A Study on the Production of Intense Cold Atomic Beams for Polarized Hydrogen and Deuterium Targets

Den Naturwissenschaftlichen Fakultäten

der Friedrich–Alexander–Universität Erlangen–Nürnberg

zur

Erlangung des Doktorgrades

vorgelegt von

Norbert Koch

aus

Nürnberg

Als Dissertation genehmigt von den Naturwissenschaftlichen Fakultäten der Universität Erlangen-Nürnberg

Tag der mündlichen Prüfung:	29. März 1999
Vorsitzender der Prüfungskommission:	Professor Dr. W. Buggisch
Erstberichterstatter:	Professor Dr. E. Steffens
Zweitberichterstatter:	Professor Dr. W. Kretschmer

Zusammenfassung

Streuexperimente mit kernspinpolarisierten internen Wasserstoff- und Deuteriumgastargets an Speicherringen sind zu einem wichtigen Werkzeug zur Messung spinabhängiger Observablen in der Kern-und Teilchenphysik geworden. Dabei hat sich bisher der Einsatz von Targets, die auf nach dem Stern-Gerlach-Prinzip arbeitenden Atomstrahlquellen basieren, als die beste und zuverlässigste Methode erwiesen. Bei diesen Quellen wird molekularer Wasserstoff in Atome dissoziiert, und mittels einer kalten Düse und eines Strahlformungssystem ein Atomstrahl hoher Phasenraumdichte erzeugt. Strahlfokussierung und Polarisationserzeugung erfolgen in einer Kombination von Multipolmagneten und adiabatischen Hochfrequenzübergängen.

Um präzise Messungen zur Aufklärung der Spinstruktur des Nukleons machen zu können, wird beim HERMES-Experiment am Deutschen Elektronen Synchrotron in Hamburg die Streuung hochenergetischer, longitudinal polarisierter Elektronen oder Positronen an kernspinpolarisierten Helium-, Wasserstoff- und Deuteriumtargets untersucht. Dabei ist eine Atomstrahlquelle im Einsatz, deren Strahl an polarisierten Wasserstoff- bzw. Deuteriumatomen zur Erhöhung der Targetflächendichte in eine sogenannte Speicherzelle injiziert wird, durch die der Elektronenstrahl verläuft. Durch eine Steigerung der mit der Quelle erreichbaren Intensität an Targetatomen könnte die statistische Genauigkeit des Experiments erheblich verbessert werden.

Im Rahmen dieser Arbeit ist die HERMES-Atomstrahlquelle im Experiment installiert und im Hinblick auf eine langzeitstabile und hohe Intensität optimiert worden. Parallel zum laufenden Experiment wurde ein Programm zu einer weiteren Intensitätssteigerung der Quelle initiiert. Dieses umfaßte den Bau eines neuartigen Dissoziators für die Produktion eines hochintensiven kalten Wasserstoff- und Deuteriumatomstrahls, sowie eines Atomstrahlteststands zur präzisen Diagnostik der Strahlparameter und zur Untersuchung der die Intensität der Atomstrahlquelle limitierenden Effekte.

Eine Modellierung der Prozesse in der Hochfrequenz-Wasserstoffentladung zeigte die Notwendigkeit einer hohen Leistungsdichte, um die angestrebten Dissoziationseffizienzen auch im Bereich großer Gasdurchsätze zu erreichen. Dazu wurde eine Plasmaquelle aufgebaut, die auf der Ankopplung einer Oberflächenwelle basiert, und durch Studien in einem Testaufbau optimiert. Beim Bau des Dissoziators wurden diese Ergebnisse berücksichtigt, sowie auf Kompatibilität mit der polarisierten Atomstrahlquelle und den technischen Anforderungen des HERMES-Experiments geachtet. Messungen am Atomstrahlteststand zeigten, daß mit dem neuen Dissoziator hohe Dissoziationsgrade über einen weiten Gasdurchsatzbereich sowie sehr gute Langzeitstabilität und Reproduzierbarkeit erreicht werden können. Untersuchungen der Rekombinationseigenschaften zahlreicher Düsenoberflächen in einem weiten Temperaturbereich wurden durchgeführt. Im Zuge einer Vergleichsmessung mit dem momentan in der HERMES–Atomstrahlquelle eingesetzten Radiofrequenzdissoziator ergab sich speziell für hohe Gasdurchsätze und bezüglich der Produktion eines Deuteriumatomstrahls eine deutliche höhere Dissoziationseffizienz

des neuen Dissoziators.

Zusätzlich zu den Dissoziationsgradmessungen wurden Strahlformung, -transport und -abschwächung untersucht. Alle Parameter zur Beschreibung der Abschwächung durch Restgas wurden ermittelt. Dies ermöglichte zusammen mit den Untersuchungen am Radiofrequenzdissoziator die Erklärung der an der HERMES-Atomstrahlquelle gemessenen unterschiedlichen Intensitäten von polarisierten Wasserstoff- und Deuteriumatomstrahlen. Jedoch zeigte sich auch, daß der Strahltransport im Rahmen der bisherigen Modelle nicht ausreichend beschrieben werden kann und möglicherweise weitere Abschwächungsmechanismen berücksichtigt werden müssen.

Schließlich wurden in dieser Arbeit zahlreiche Vorbereitungen am Atomstrahlteststand sowie am Testaufbau für die Plasmaquelle für weiterführende Studien zur Erhöhung der Phasenraumdichte des Atomstrahls und damit der Intensität der polarisierten Atomstrahlquelle getroffen.

Table of Contents

1 Introduction

The production of nuclear polarized hydrogen and deuterium targets or ion beams in order to study spin–dependent observables is of high interest in nuclear and particle physics.

Recently, experiments using a storage ring for polarized protons and an internal polarized gas target to study the nucleon–nucleon interaction have been performed at IUCF. Spin–correlation parameters have been determined and pion production near threshold has been investigated to improve the present understanding of the short–range forces in the nucleon–nucleon potential [1, 2, 3]. Similar studies are in preparation at COSY by the EDDA collaboration [4, 5]. Moreover, a series of new experiments is suggested employing the ANKE spectrometer [6].

In particle physics, deep–inelastic scattering of polarized lepton beams off nuclear polarized hydrogen and deuterium targets is used to investigate the internal proton and neutron spin structure. The nucleon spin consists of the spin contributions from the quarks and gluons as well as of their corresponding angular momenta. The total quark spin contribution can be determined by measuring the spin structure function g_1 of the proton or neutron. Recent high precision experiments for the determination of g_1 employing external polarized lepton beams and polarized solid state or high pressure targets have been performed at CERN by the SMC collaboration [7, 8, 9, 10] and in the course of the SLAC experiments E142 [11], E143 [12], E154 [13] and E155 [14].

The HERMES experiment at DESY has been designed to measure the total, the flavour dependent and the see quark spin contribution as well as the contribution arising from angular orbital momentum of the quarks [15, 16]. Moreover, attempts are being made to study the contribution from the gluon polarisation [17, 18]. For these purposes, the 27 GeV electron or positron beam of the HERA synchrotron is scattered off internal polarized gas targets. A decisive milestone for the approval of HERMES was the demonstration of high longitudinal electron or positron polarisation of 60 ... 65 % provided by the storage ring [19]. The use of an internal gas target allows for low systematic uncertainties, since all target nuclei are polarisable and the target polarisation can be switched instantaneously. In order to measure the proton and deuteron spin structure, a Stern–Gerlach type Atomic Beam Source (ABS) is used to inject a nuclear polarized hydrogen or deuterium beam into a T–shaped storage cell through which the HERA beam is circulating. The atomic fraction and nuclear polarisation within the cell is determined by extracting a sample beam from the center of the cell into a target gas analyser [20] and a Breit–Rabi polarimeter [21].

Apart from the beam parameters, the statistical precision of polarized scattering experiments depends on the target figure of merit, which is given by the product of the target areal density and the square of the target polarisation. In case of the HERMES experiment, the target polarisation obtained with the ABS is about 90 % [22], and the intensity is limited at present to about $6.4(5.2) \times 10^{16}$ H(D)/s [23, 24]. Although a storage cell is used, which increases the target density by about two orders of magnitude compared to the free atomic jet, the achievable target density is a factor of more than 10 below the lifetime limit of the HERA beam [16].

Exhibiting higher intensities, the so–called Laser–Driven Source (LDS) has been proposed as an alternative to the ABS. Atomic flow rates of up to 10^{18} H(D)/s at a polarisation of 60 . . . 70 % have been reported [25]. However, caused by non–reproducable surface effects, the LDS has not resulted in a reliable target source yet [26]. In the course of a test experiment at IUCF, only low polarization values as well as low atomic fractions have been achieved [27]. From this experience, the ABS is the clearly superior target source for the HERMES experiment, since it provides both a higher figure of merit and long–term stable and reproducible operation.

As a consequence, a program has been initiated to increase the output intensity of the ABS. This involved a detailed study on the production of cold atomic hydrogen or deuterium beams being the first step of polarized atomic beam production. In the framework of this thesis, a new type of dissociator has been developed yielding a high atomic flow rate as well as a long–term stable and reproducible behaviour. Additionally, an atomic beam test stand has been set up to investigate all parameters relevant for dissociator operation in an ABS and to study beam formation and attenuation.

In order to motivate this work, the operational principle of polarized atomic beam sources and the performance of the HERMES–ABS are reviewed in section 2. In section 3, a simple model is developed to describe the processes in the hydrogen discharge. This model is the basis of an improved understanding with respect to the production of high atomic flow rates in the plasma source of the dissociator. The design criteria and operational principle of the plasma source as well as the optimization towards a high atomic fraction in the discharge are reviewed in section 4. In section 5 and 6, the new dissociator and the atomic beam test stand are described. As shown in section 7, a series of degree of dissociation measurements has been performed to study the dissociator performance. The investigations of beam formation and attenuation are presented in section 8. Finally, in section 9, the main results obtained in the framework of this thesis are reviewed and an outlook towards the next steps in the atomic beam development is given.

2 The Polarized Atomic Beam Source

In this section, atomic beam sources (ABSs) for the production of polarized atomic beams are reviewed and their application in an experiment is described. For simplicity, only the production of nuclear polarized atomic hydrogen beams is considered.

In section 2.1, the operational principle of AB sources is described. The ABS used for the HERMES experiment is presented in section 2.2, and the performance in the experiment is reviewed. Finally, in section 2.3, a description for the output flow rate of polarized atoms into the target cell is given, and possible ways to further increase the output intensity of the HERMES–ABS are discussed.

2.1 Principle of operation

The basic set–up of a polarized atomic beam source is shown schematically in fig. 2.1. In

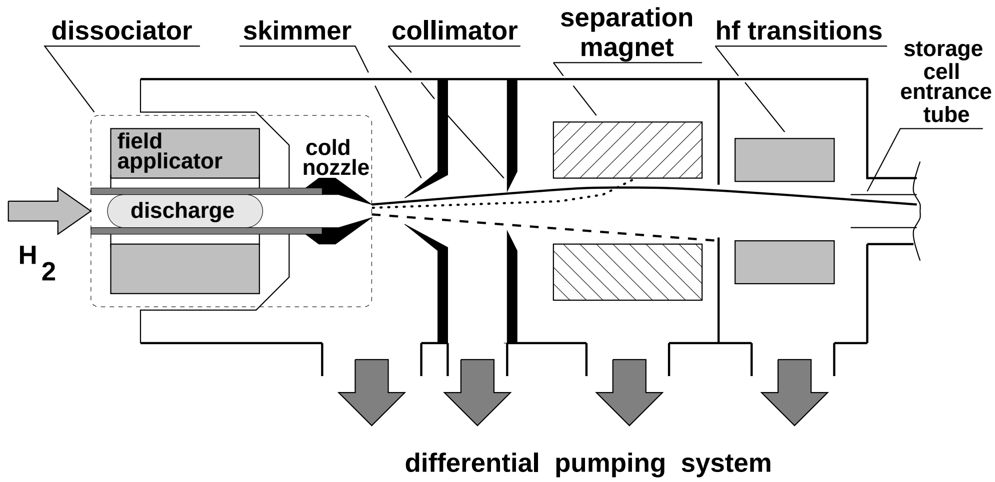

Fig. 2.1: Schematic representation of a polarized atomic beam source. for the production of a nuclear polarized hydrogen beam in a strong magnetic holding field. The continuous, dotted and dashed lines denote typical trajectories of atoms with electron spin $m_S = +1/2$ and $-1/2$ and that of molecules. The functional principle of the different components is explained in the text.

the dissociator, hydrogen molecules are partially dissociated into atoms in a gas discharge. The gas throughput usually ranges between 0.5 and 3 mbar l/s resulting in gas pressures between 0.3 and 3 mbar. The discharge is sustained in the plasma source which consists of the field applicator and the discharge vessel. Typically, the field applicator is based on a resonant circuit radiating radio or microwave frequencies into a cylindrical tube shaped discharge vessel. The molecules are dissociated via electron impact with the free electrons in the discharge, which gain energy from the applied electromagnetic field (see e.g., ref. [28]). The properties of the hydrogen discharge are discussed in detail in section 3. At its downstream end, the discharge tube is terminated by a cooled nozzle.

The nozzle, a skimmer and a collimator, together with a powerful differential pumping system, serve to form a beam with high phase space density. Assuming the nozzle to be a point–like source, the intensity distribution function can be described as [29, 30]

$$f_I(\vartheta) = \frac{n+1}{2\,\pi}\,\cos^n\vartheta, \tag{2.1}$$

where ϑ is the polar angle with respect to the beam axis, and n is the so–called peaking exponent.
It is obvious, that an increase in the peaking exponent results in a higher forward intensity of the beam. Peaking exponents of $n > 1$ can be achieved, if the beam leaving the nozzle expands adiabatically. As a condition for adiabatic expansion, the flow through the nozzle has to be laminar, and the ratio of the pressure at the nozzle entrance to the pressure in the nozzle chamber has to be large enough [31]. The flow regime through the nozzle can be characterized by the Knudsen number, which is defined as the ratio of the mean free path $\bar{\lambda}$ of the gas particles to the nozzle diameter d [32, 33]:

$$K = \frac{\bar{\lambda}}{d}, \quad \bar{\lambda} = \frac{k\,T}{4\,\pi\,\sqrt{2}\,p\,r^2}, \tag{2.2}$$

where k is the Boltzmann constant, T is the gas temperature, p the pressure and r the gas kinetic radius.
Assuming thermalization of the gas particles on the nozzle surface, for a typical nozzle temperature around 100 K, a nozzle diameter of 2 mm and a pressure at the nozzle entrance of 1 mbar, one obtains $K \approx 0.02$. Laminar flow is characterized by $K < 0.01$. Thus the flow through the nozzle is in the so–called transition regime, close to be laminar. Because of a high pumping speed, the pressure in the nozzle chamber typically is about 10^{-4} mbar and hence about four orders of magnitude lower than the pressure at the nozzle entrance. Consequently, for low pressures and large nozzle diameters one expects low values of n close to one and an increase in n for increasing pressures and decreasing diameters. The distribution function of the longitudinal velocity v_z of the beam particles leaving the nozzle follows a modified Maxwell distribution [31]:

$$f(v_z) \propto \left(\frac{m}{2\,k\,T_{\mathrm{beam}}}\right)^{\frac{3}{2}} \exp\left[-\frac{m}{2\,k\,T_{\mathrm{beam}}}\,\left(v_z - v_z^{\mathrm{drift}}\right)^2\right], \tag{2.3}$$

where m is the molecular or atomic mass, T_{beam} is the beam temperature and v_z^{drift} the drift velocity of the beam with respect to the mean velocity expected from the non–modified Maxwell distribution.

After being shaped and collimated, the beam passes a sixpole magnet, where the atoms are spatially selected according to their electron spin following the Stern–Gerlach principle (see e.g. refs. [34, 35]). Stern–Gerlach separation for hydrogen atoms is based on the interaction of a magnetic gradient field with the magnetic moment of the atom. Hydrogen atoms in the ground state have an electron spin $S = 1/2$ with a z–component $m_S = \pm 1/2$ and a proton spin $I = 1/2$ with $m_I = \pm 1/2$. Electron and proton spin couple to the total spin $F = S + I = 0$ or $F = 1$ with $m_F = 0$ or $m_F = -1, 0, +1$, respectively. The so–called hyperfine splitting energy E_{hfs}, which denotes the energy difference between the states with $F = 0$ and $F = 1$ corresponds to a frequency of 1420 MHz. If an external magnetic field B is applied, the interaction with the magnetic momentum of the atom leads to an energy splitting of the $F = 1$ state according to the Zeemann effect. If the critical field B_{c}, defined as

$$B_{\mathrm{c}} = \frac{E_{\mathrm{hfs}}}{(g_S - g_I)\,\mu_B} = 50.7\,\mathrm{mT}\,, \tag{2.4}$$

where $g_S = 2.002$, $g_I = 0.00304$ and $\mu_B = 9.274078 \times 10^{-24}$ J/T are the g–factor of the electron and the proton and the Bohr magneton, respectively, is exceeded, proton and electron spin decouple. The energy splitting E due to an external magnetic field is given by the Breit–Rabi formula [36]:

$$E = -\frac{E_{\mathrm{hfs}}}{4\,I + 2} + g_I\,\mu_B\,m_F\,B + (-1)^{F+1}\,\frac{E_{\mathrm{hfs}}}{2}\,\sqrt{1 + \frac{4\,m_F}{2\,I + 1}\,\frac{B}{B_{\mathrm{c}}} + \left(\frac{B}{B_{\mathrm{c}}}\right)^2}\,. \tag{2.5}$$

In fig. 2.2, the relative energy splitting E/E_{hfs} is shown as a function of the ratio B/B_{c}. For high magnetic fields, the interaction with the magnetic moment of the atoms is dominated by the interaction with the magnetic moment of the electron as a result of the decoupling of S and I and the about 1837 times higher magnetic moment of the electron.

The energy splitting in a strong external magnetic field is used to spatially separate the beam particles according to their electron spin. Because of a field gradient in radial direction, multipole magnets are applied. The force on the hydrogen atoms in a strong magnetic multipole field is given as

$$\vec{F} = -\nabla E = -\frac{\partial E}{\partial r}\,\vec{e}_r = -\frac{\partial E}{\partial B}\,\frac{\partial B}{\partial r}\,\vec{e}_r \approx \begin{cases} -\mu_B\,\frac{\partial B}{\partial r}\,\vec{e}_r\,, & m_S = +1/2 \\ +\mu_B\,\frac{\partial B}{\partial r}\,\vec{e}_r\,, & m_S = -1/2\,, \end{cases} \tag{2.6}$$

where r is the radial component and $\vec{e}_r$ the unity vector in radial direction.
As a result, atoms with $m_S = +1/2$, are accelerated in radial direction towards the magnet axis and those with $m_S = -1/2$ away from the magnet axis. In AB sources, usually sixpole magnets are used with a radial field dependency

$$B(r) = B_0\,\left(\frac{r}{r_0}\right)^2\,, \tag{2.7}$$

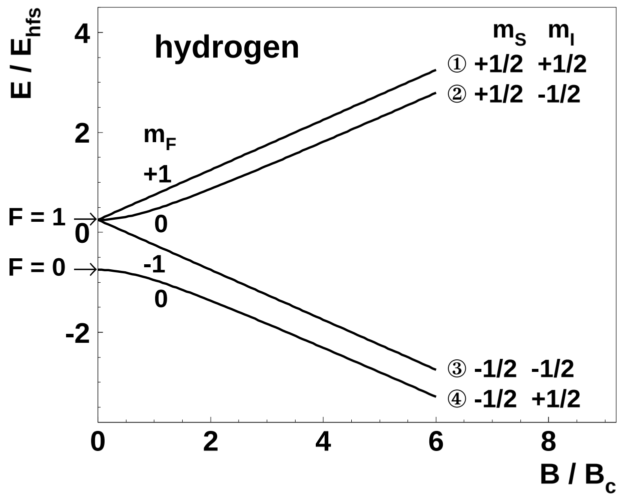

Fig. 2.2: Breit–Rabi diagram for hydrogen. The ratio E/E_{hfs} of the hyperfine splitting energy with and without external magnetic field for all four states ①, ②, ③ and ④ is shown as a function of the ratio B/B_{c} of the external magnetic field to the critical magnet field.

where B_0 and r_0 are the pole tip field and radius, respectively. Hence the radial field gradient is proportional to the radial position, so that relatively large solid angles can be accepted. Taking into account eqs. (2.6) and (2.7), the trajectory of a $m_S = +1/2$ atom can be calculated for a magnet with cylindrical bore as

$$r(z) = \frac{r_e}{\Lambda}\,\sin(\Lambda\, z) + r_e\,\cos(\Lambda\, z)\,, \tag{2.8}$$

where z is the axial position, r_e is the radial position at which the atom enters the sixpole magnet and $1/\Lambda$ is the focal length given as

$$\frac{1}{\Lambda} = r_0\, v_z\,\sqrt{\frac{m_{\mathrm{a}}}{2\,\mu_B\, B_0}}\,. \tag{2.9}$$

Here, m_{a} denotes the atomic hydrogen mass and v_z is the z–component of the atomic velocity. For atoms with $m_S = -1/2$, the trigonometric functions are replaced by the corresponding hyperbolic functions. In the ideal case, the geometry and the pole tip field of the magnet are designed such, that a maximum of the hydrogen atoms with $m_S = +1/2$ are transmitted into the entrance tube of the storage cell, and that those with $m_S = -1/2$ are completely deflected. The corresponding trajectories are indicated by the solid and dotted line in fig. 2.1. The trajectory of a molecule, which is not affected by the magnetic field, is shown by the straight dashed line.

The nuclear vector polarisation is defined as

$$P_{\mathrm{p}} = \frac{N(m_I = +1/2) - N(m_I = -1/2)}{N(m_I = +1/2) + N(m_I = -1/2)}\,, \tag{2.10}$$

where $N(m_I = +1/2)$ and $N(m_I = -1/2)$ are the numbers of atoms with proton spin orientated parallel and anti–parallel to the external magnetic field, respectively.

Since at the end of the multipole magnet, in the ideal case the beam consists exclusively of atoms in state ① and ② with equal occupation numbers, the proton polarisation is expected to be zero. However, the adiabatic transition to a weak magnetic field occuring in the sixpole stray field results in a re–coupling of proton and electron spin and a nuclear polarisation of $P_{\rm p} = 0.5$. The proton polarisation of each of the four hyperfine states as a function of the external magnetic field is shown in fig. 2.3 following the calculation given in ref. [37]. It can be seen, that for a suitable combination of hyperfine states, full nuclear

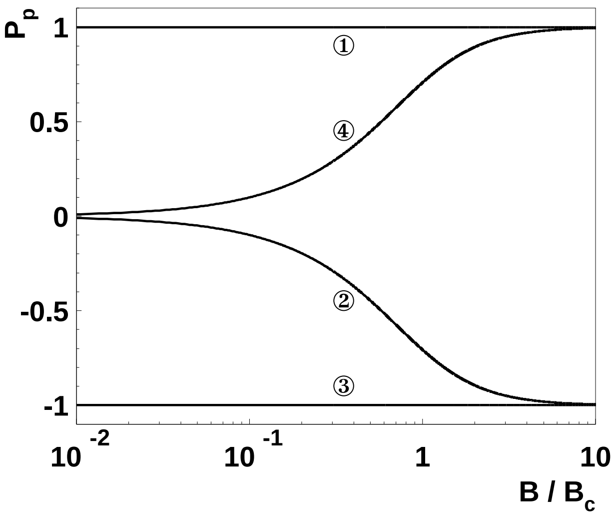

Fig. 2.3: Nuclear Polarization $P_{\rm p}$ as for the four hyperfine states ① , ② , ③ and ④ as a function of the ratio $(B/B_{\rm c})$ of the external magnetic field to the critical magnet field.

polarisation is obtained in a strong external magnetic field. In order to make use of this behaviour, so–called adiabatic high frequency transitions are employed. Those serve to induce interchanges between the hyperfine states by superimposing a high frequency with a static and a gradient magnetic field [38]. Applying a strong magnetic guide field after the transition units, full nuclear polarisation of the beam injected into the storage cell can then be achieved for the combination of states ① and ④ or states ② and ③ , respectively. This requires an interchange from state ① to ③ in a so–called weak field transition or from state ② to ④ in a so–called strong field transition.

2.2 The HERMES–ABS

The HERMES target source is based on the ABS for the FILTEX experiment [39]. Prior studies on a test source [40] yielded the main design criteria of the FILTEX–ABS [41], which has been the first high–intensity source owing to its advanced vacuum system, its improved dissociator and its magnet system. For the HERMES experiment, the FILTEX source has been modified in order to inject two hyperfine states into the storage cell [42].

In the following, a technical description of the HERMES–ABS is given and the running performance within the HERMES experiment is reviewed.

2.2.1 Technical description

Figure 2.4 shows a side view drawing of the HERMES–ABS (taken from ref. [46]). The main geometrical parameters are listed in table A.1. The dissociator is placed on large

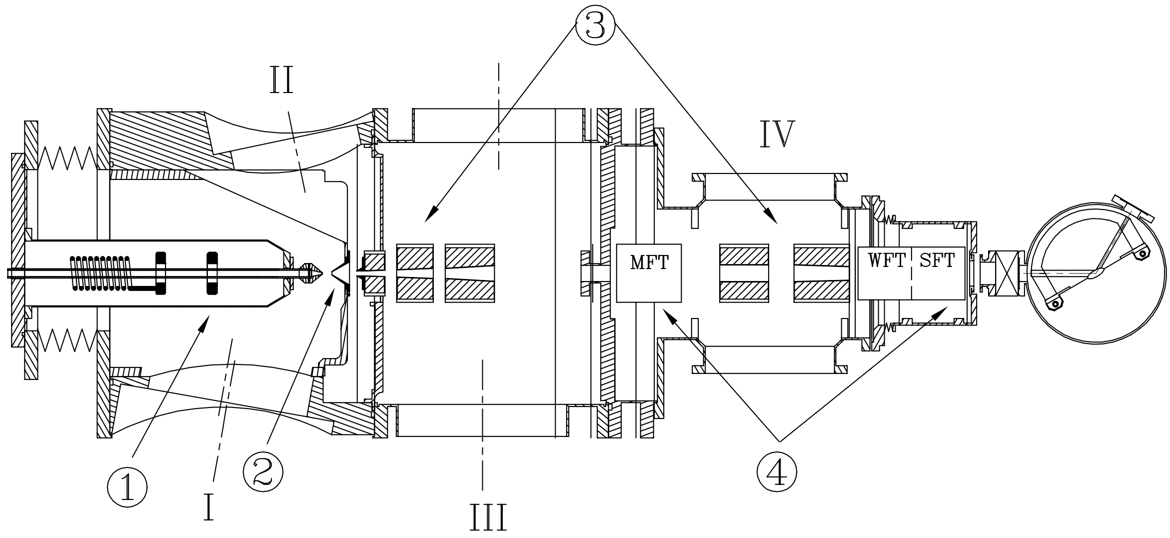

Fig. 2.4: Side view of the HERMES–ABS. ① indicates the dissociator, ② the skimmer, ③ the two sets of sixpole magnets and ④ the three high frequency transition units. The roman numbers show the different pumping stages: I is the dissociator chamber, II the skimmer chamber, and III and IV are the two sixpole chambers. The atomic beam is injected into the storage cell which is shown at the right.

manipulator in order to ajust the nozzle position. The plasma source of the applied radio frequency dissociator (RFD) consists of a LC–circuit as field applicator, tuned to a resonance frequency of 13.56 MHz, and a water cooled discharge tube. The degrees of dissociation provided by the RFD have been measured to be in the range between 30 % and 60 % at the standard gas throughput of 1 . . . 1.5 mbar l/s [49, 50, 42]. Earlier studies, however done with a different nozzle geometry, report a decrease in the degree of dissociation from 70 % at 1 mbar l/s to less than 30 % at 5 mbar l/s [41]. The conical nozzle at the end of the tube is made of aluminum with a small diameter of 2 mm and a channel length of about 15 mm. It is cooled with a closed–cycle helium refrigerator coldhead via a massive cooling bridge [43]. At the working point, the gas throughput typically is about

1.25 mbar l/s, the pressure in the discharge tube 1 mbar, the nozzle temperature 100 K and the applied radio frequency power 300 W.

The beam forming system consists of a conical skimmer at the end of the dissociator chamber, a flat collimator at the entrance of the first sixpole magnet and a powerful differential pumping system with a nominal pumping speed of 5600 l/s in the dissociator chamber and 2000 l/s in the skimmer chamber.

The magnet system consists of five rare–earth permanent sixpole magnets [44] with pole tip fields of up to 1.5 T, mounted in the first and second sixpole chamber with pumping speeds of about 7500 l/s and 4000 l/s, respectively. In contrast to the simplified scheme given in fig. 2.1, two sets of magnets are employed, of which the first separates off atoms with $m_S = -1/2$, and the second focusses those atoms with $m_S = +1/2$ left into the entrance tube of the storage cell. The splitting of the two magnet sets into three and two magnets each provides an increased pumping conductance for the residual gas accumulating in the magnet bores. The magnet geometry and, taking into account the Halbach–equation [45], their magnetic field strengths have been adapted to the velocity profile of the atomic nozzle beam in order to obtain a maximum transmission for $m_S = +1/2$ atoms into the storage cell feed tube. This has been done using numerical tracking calculations combined with a genetic algorithm and yielded the given geometry with divergent and convergent conical bores for the first and second sixpole set, respectively [50].

Three high frequency transition units are used, of which a medium field transition (MFT) is placed between the two sets of magnets and a weak and strong field transition (WFT and SFT) are mounted in the appendix chamber after the second magnet set. The MFT serves to inject a single hyperfine state and hence to produce both full electron and nuclear polarisation. Using the WFT and the SFT full nuclear polarisation (at zero electron polarisation) for two injected hyperfine states is provided. The combination of the three transitions also allows to produce a nuclear tensor polarized deuterium beam. The efficiencies of all transitions have been determined to range between 98 % and 100 % [42].

2.2.2 Operation within the experiment

The entire target has been assembled in the second half of 1995 and installed in the experiment at the beginning of 1996. In this time, the ABS has been mainly used to provide polarized beam for calibration measurements with the target polarimeter. In parallel, the sixpole magnets have been optically aligned and the dissociator has been optimized to obtain long–term stable operation. Due to the long running periods of the HERA collider, long–term stability of the output intensity is vital to avoid losses during data taking of the experiment. It has been found, that the oxygen admixture of about 1 . . . 4 vol% added to the hydrogen in order to obtain a maximum output intensity [43, 47] resulted in a decrease in intensity already after several hours of continuous operation.

This behaviour is due to excessive water formation in the discharge, which is adsorbed on the cold nozzle, as shall be shown in detail in sections 7.3 and 7.4. Following the experience with a similar plasma source applied in the Erlangen laser–driven source, where high atomic fractions could be achieved without oxygen admixture [48], the discharge tube has been cleaned with a mixture of hydrofluoridic and chlorine acid as described in appendix D. As a result, the oxygen admixture needed to obtain a maximum in output intensity could be reduced to the low permille range.

The intensity of polarized hydrogen atoms measured shortly before the ABS has been installed in the experiment was $6.4 \times 10^{16}\,\mathrm{s}^{-1}$. This was in agreement with the value for higher oxygen admixtures [43, 23]. In order to obtain a reproducible and stable oxygen admixture for ABS operation in the HERMES experiment, a buffer volume with a calibrated needle valve has been installed. Typically, the oxygen admixture has been set to 0.15 flux% for the first few hours after starting up the discharge, until the maximum in output intensity was reached. Then it has been reduced to 0.04 flux%, whilst the intensity stayed constantly high [24]. As a result, the ABS could deliver stable intensity for 7 . . . 8 days inbetween two nozzle warm–ups needed to remove the ice layer. In fig. 2.5 the characteristic evolution of the normalized total count rate $\Phi_{\mathrm{ABS}}^{(\mathrm{TGA})}$[1] of the target gas analyzer (TGA), which is proportional to the intensity of the ABS, is shown as a function of running time for a period of four weeks. Switching on the dissociator after the nozzle

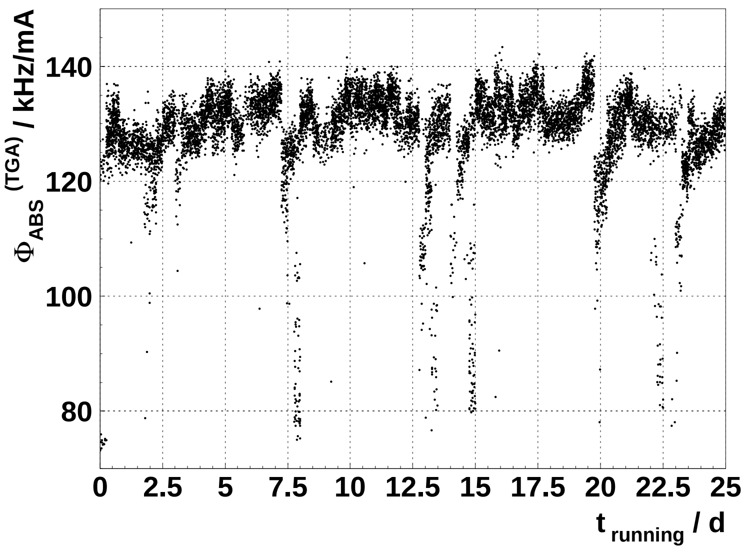

Fig. 2.5: Dependence of the normalized TGA rate $\Phi_{\mathrm{ABS}}^{(\mathrm{TGA})}$, which is proportional to the ABS output intensity, on the running time. The data presented are taken from a four weeks period during the experimental run in 1996. The steep rises in $\Phi_{\mathrm{ABS}}^{(\mathrm{TGA})}$ are caused by nozzle regeneration cycles.

has been regenerated, $\Phi_{\mathrm{ABS}}^{(\mathrm{TGA})}$ typically rises from about 80 kHz/mA up to a mean value around 130 kHz/mA within the first few hours of operation and then stays constant within

[1] $\Phi_{\mathrm{ABS}}^{(\mathrm{TGA})}$ gives the channeltron count rate of the TGA mass spectrometer normalized to the ion current.

$\pm 15\,\%$. From the steep rises in the intensity one can conclude, that the nozzle has been usually warmed up every few days.

In summary, the ABS has been found to be a reproducable and long–term stable operating target source during the 1996 and 1997 running period of the HERMES experiment.

2.3 The output intensity

2.3.1 Description

Operating in a strong target holding field, the maximum flow rate of polarized atoms $\vec{a}$ injected into the entrance tube of the storage cell can be written as

$$\Phi_{\vec{a}}^{\mathrm{cell}} = Q'_{\mathrm{a}} \int_{\Omega_{\mathrm{mag}}} f_I(\vartheta)\,\mathrm{d}\Omega\ \mathcal{T}_{\mathrm{mag}}\ S\,, \tag{2.11}$$

where Q'_{a} is the atomic flow rate out of the nozzle, Ω_{mag} is the solid angle of the first sixpole magnet, $\mathcal{T}_{\mathrm{mag}}$ is the transmission probability of atoms emitted into Ω_{mag} into the entrance tube of the storage cell and S is an attenuation factor accounting for beam losses due to scattering.
The atomic flow rate out of the nozzle is given as

$$Q'_{\mathrm{a}} = 2\,Q'_{\mathrm{m}}\,\alpha\,, \tag{2.12}$$

where Q'_{m} is the molecular gas throughput[2] and α is the degree of dissociation in the nozzle beam.
In general, α depends on the gas throughput and pressure as well as on the properties of the discharge tube and nozzle surface, as shall be shown both theoretically and experimentally in sections 3.5, 7.4 and 7.5. In order to obtain the atomic flow rate into the first sixpole magnet, the intensity distribution function from eq. (2.1) is integrated over the solid angle accepted by the first magnet:

$$\int_{\Omega_{\mathrm{mag}}} f_I(\vartheta)\,\mathrm{d}\Omega\ = 1 - \cos^{n+1}\vartheta_{\mathrm{mag}}\,, \tag{2.13}$$

where ϑ_{mag} is the corresponding maximum polar angle.
The peaking exponent n cannot be accessed directly, but derived from the longitudinal velocity distribution $f(v_z)$ of the beam given in eq. (2.3). Assuming the lonitudinal and

[2] Q'_{m}, which denotes the throughput in units of molecules/s, is calculated from Q_{m} given in mbar l/s for a given gas temperature T considering the ideal gas law as follows:

$$1\,\mathrm{mbar\,l/s} = 2.69\times10^{19}\,\frac{1}{\mathrm{s}}\,\frac{273\,\mathrm{K}}{T}\,.$$

transversal beam temperature to be equal, the Machnumber M is obtained from $f(v_z)$ as [52]

$$M = v_z^{\text{drift}} \sqrt{\frac{m}{(c_p/c_v)\; k\, T_{\text{beam}}}} \tag{2.14}$$

from which n can be derived [51]:

$$G = \frac{n+1}{2} = \frac{(c_p/c_v)}{2} M^2 \,, \tag{2.15}$$

where G is the gain factor in forward intensity compared to an effusive source, and the ratio of the isopressure to the isovolume specific heat $(c_p/c_v) = 5/3$ is the adiabatic coefficient for atomic hydrogen.
Earlier measurements have shown, that M is well above 1 as a result of an adiabatic expansion of the beam behind the nozzle [53, 50]. In general, M has been found to increase with increasing gas throughput, decreasing nozzle diameter and decreasing nozzle temperature. From the most recent time–of–flight measurements done with the present nozzle configuration of the HERMES–ABS [50], n can be determined to be around 15.

The transmission of the sixpole system is the average over the transmissions t_i of the different hyperfine states:

$$\mathcal{T}_{\text{mag}} = \frac{1}{4}\sum_{i=1}^{4} t_i \,, \quad \text{with } t_i = \frac{(N_i)_{\Omega_{\text{cell}}}}{(N_i)_{\Omega_{\text{mag}}}} \,, \tag{2.16}$$

where $(N_i)_{\Omega_{\text{mag}}}$ and $(N_i)_{\Omega_{\text{cell}}}$ are the number of atoms in state $ⓘ$ accepted by the first magnet and of those transmitted into the entrance tube of the storage cell, respectively. Taking into account that the beam follows the velocity distribution from eq. (2.3), it is obvious from eq. (2.9), that the width $\Delta v_z \propto \sqrt{T_{\text{beam}}}$ of $f(v_z)$ should be preferably small in order to obtain a maximum transmission. In order to keep the magnet reasonably short, the mean velocity $\bar{v}_z$ of the beam has to be relatively low. Therefore, the nozzle is cooled which also leads to a reduction in T_{beam}, since it has been shown that the beam temperature is proportional to the nozzle temperature [50].

The attenuation factor $S = 0 \ldots 1$ is given as the ratio between the intensity $\Phi_{\vec{\text{a}}}^{\text{cell}}$ expected from eq. (2.11) assuming $S = 1$ and the intensity actually obtained. S has been introduced in order to explain the non–linear behaviour of the undissociated beam intensity with increasing gas throughput [41]. Attenuation of the beam arises from scattering of the beam particles with residual gas particles (rest gas attenuation, RGA) and from scattering with other particles in the beam (intra–beam scattering, IBS):

$$S = S_{\text{RGA}}\; S_{\text{IBS}} \,. \tag{2.17}$$

Assuming single scattering losses and the simplified scenario of a beam passing a vacuum chamber with a length l and a homogenious residual gas presure p_{rg}, S_{RGA} can be written as [31]

$$S_{\mathrm{RGA}} = \exp\left(-l\,\sigma_{\mathrm{rg}}^{\mathrm{eff}}\,\frac{p_{\mathrm{rg}}}{k\,T_{\mathrm{rg}}}\right), \tag{2.18}$$

where $\sigma_{\mathrm{rg}}^{\mathrm{eff}}$ is the effective cross section for single scattering losses and T_{rg} is the residual gas temperature.
In case of the ABS, the pressures and lengths of the several pumping stages have to be considered and one has to integrate the residual gas pressure over the whole distance L between the nozzle exit and the entrance tube into the storage cell, hence

$$l\,p_{\mathrm{rg}} \longrightarrow \int_0^L p_{\mathrm{rg}}(z)\,\mathrm{d}z\,.$$

The RGA losses for the HERMES–ABS due to a finite nominal pumping speed have been determined to be $S_{\mathrm{RGA}} = 0.81$ at the working point [42].

A model for the reduction in flow density ϕ caused by single intra–beam scattering losses is given in ref. [54]. The description is restricted to a parallel beam, as it is expected after the first sixpole magnet system, and a scattering cross section based on a hard–sphere potential is assumed. The decrease in flow density with increasing distance from the nozzle exit z is described by a differential equation as

$$\frac{\mathrm{d}\phi(z)}{\mathrm{d}z} = -\frac{\Delta v_z\,\sigma_{\mathrm{ib}}^{\mathrm{eff}}}{\bar{v}_z^2}\,\phi^2(z)\,, \tag{2.19}$$

the solution of which is given by

$$\phi(z) = \phi_0\left(1 + z\,\frac{\Delta v_z\,\sigma_{\mathrm{ib}}^{\mathrm{eff}}}{\bar{v}_z^2}\,\phi_0\right)^{-1}, \tag{2.20}$$

where Δv_z and $\bar{v}_z$ are the width and the mean value of the velocity distribution $f(v_z)$, $\sigma_{\mathrm{ib}}^{\mathrm{eff}}$ is the effective intra–beam scattering loss cross section and $\phi_0 = \phi(z = 0)$ is the initial flow density out of the nozzle.
Hence, for the total IBS induced attenuation factor over the whole distance L from the nozzle exit to the entrance tube of the storage cell one obtains

$$S_{\mathrm{IBS}} = \frac{\phi(z = L)}{\phi_0}\,. \tag{2.21}$$

However, it has been estimated that IBS induced losses are neligible for the current flow densities obtained with high–intensity AB sources.

2.3.2 Optimization of the output intensity

From the previous considerations, it can be concluded that a maximum in output intensity requires:

1.) A nozzle beam with a high atomic fraction α for a wide range of gas throughputs Q_{m}.

2.) A high phase space density of the nozzle beam in order to maximize the exponent n in the intensity distribution function and to minimize the width Δv_z of the velocity distribution $f(v_z)\,\mathrm{d}v_z$.

3.) An proper matching of the sixpole magnet system to the properties of the beam in order to maximize $\mathcal{T}_{\mathrm{mag}}$.

4.) A maximum in S and hence a minimum in the integrated pressure $\int_0^L p_{\mathrm{rg}}(z)\,\mathrm{d}z$ in order to minimized RGA losses as well as a minimum in Δv_z to minimize IBS losses.

The geometries of the nozzle, the skimmer–collimator and the magnet system of the HERMES–ABS have been steadily optimized in order to minimize RGA for the given nominal pumping speed and to maximize the transmission [41, 49, 42]. However, as mentioned above, the dissociator shows a quite poor performance. Therefore, considering the latest studies and intensity models on the HERMES–ABS [42], the most straightforward way to increase the output intensity is to increase the degree of dissociation in the nozzle beam. Regarding the various efforts and investigations towards an optimization of the RFD used at present [55, 41, 43], the relatively low atomic fraction in the nozzle beam and its decrease for an increased gas throughput can be traced back to a low dissociation efficiency in the plasma source itself rather than to excessive atomic recombination losses in the nozzle.

As a first step towards the design of an improved plasma source, the properties of the high frequency sustained hydrogen discharge have been investigated, which is presented in the following section.

3 The High Frequency sustained Hydrogen Discharge

In the following, a discharge model will be developed to describe the properties in a high frequency sustained hydrogen discharge for the typical gas conditions of a dissociator.

The degree of dissociation in the discharge is determined by the production and loss mechanisms of atoms. These depend on macroscopic parameters such as the power transferred to the plasma, the gas conditions and the properties of the discharge vessel. Typically, the discharge is sustained by application of an electromagnetic high frequency (hf) field, which is coupled into a cylindrical dielectric discharge tube with the hf field applicator located outside. As mentioned in the previous section, the gas throughput ranges between 0.5 and 5 mbar l/s resulting in a pressure in the discharge tube range between 0.3 and 3 mbar. If the applied electrical field strength is sufficiently high, the gas in the discharge tube breaks down and a steady–state glow discharge is formed. Such a "cold" plasma is characterized by a low degree of ionisation [56]

$$\zeta = \frac{n_\mathrm{e}}{n_\mathrm{n}} = \frac{n_\mathrm{i}}{n_\mathrm{n}} = 10^{-5} \ldots 10^{-3}\,,$$

where n_e, n_i and n_n denote the free electron, the ion and the neutral density in the gas. The low degree of ionisation, together with the fact that the electron mobility is higher than the ion mobility, leads to a substantially higher temperature of the electrons compared to the neutral and ion gas [57]. Typically, the temperatures of neutrals and ions range between 500 K and 2000 K corresponding to energies of $0.08 \ldots 0.35$ eV, whilst the electrons have mean energies of $\bar{u} = 2 \ldots 10$ eV. As a result, the discharge properties are dominated by the electron kinetics: the free electrons gain energy from the electromagnetic field and dissipate it via inelastic and elastic collisions with the neutral gas components.

For the calculations given below on the electron kinetics, the balance of charged particles and the atomic losses, a simplified scenario has been assumed:

(i) The discharge occurs in a long cylindrical dielectric tube with a typical inner radius of $r_\mathrm{dt} = 0.5$ cm.

(ii) The discharge volume is assumed to have a constant value of $V_\mathrm{pl} = 30\,\mathrm{cm}^3$. The volume is terminated with low conductances at both sides. This requirement makes the gas density independent of the gas temperature.

(iii) The electron density is assumed to have the following spatial profile

$$n_\mathrm{e}(r,\,z) = \begin{cases} \mathrm{const.} = n_\mathrm{e},\ 0 \le z \le L,\ r < r_\mathrm{dt} \\ 0,\ r = r_\mathrm{dt}\,, \end{cases} \tag{3.1}$$

where r and z denote the radial and axial direction, and L is the plasma length.

(iv) The molecular gas density shall be $2.47 \times 10^{22}\,\mathrm{m}^{-3}$ according to a typical pressure of 1 mbar at 293 K independent of the gas throughput. This corresponds to the situation of a variable conductance at the downstream end of the discharge.

3.1 Basic definitions and relations

In order to describe the electron–impact driven processes in the discharge, some basic quantities are introduced in the following.
The specific reaction rate k_X per electron and unit density for a process x is given by

$$k_\mathrm{X} = \langle v(u)\,\sigma_\mathrm{X}(u)\rangle = \sqrt{\frac{2}{m_\mathrm{e}}}\,\langle\sqrt{u}\,\sigma_\mathrm{X}(u)\rangle, \tag{3.2}$$

where u is the electron energy, $v(u)$ the electron velocity, $\sigma_\mathrm{X}(u)$ the cross section for process x and m_e the electron mass.
The brackets denote an averaging over the electron energy distribution function (EEDF) $f(u)$, where $\sqrt{u}\,f(u)\,\mathrm{d}u$ gives the probability to find an electron with an energy between u and $u + \mathrm{d}u$.
The EEDF is normalized as follows:

$$\int_0^{+\infty} \sqrt{u}\,f(u)\,\mathrm{d}u = 1. \tag{3.3}$$

Hence k_X becomes:

$$k_\mathrm{X} = \sqrt{\frac{2}{m_\mathrm{e}}}\int_0^{+\infty} u\,\sigma_\mathrm{X}(u)\,f(u)\,\mathrm{d}u\,. \tag{3.4}$$

Since the free electrons are *a priori* not in thermal equilibrium, an exact determination of the EEDF can only be obtained solving self–consistently the Boltzmann transport equation for the electrons in the discharge (see e.g., ref [58]). Calculations given in ref. [59] predict that the EEDF becomes Maxwellian for a sufficiently high collision rate between the free electrons, i.e. in case of a high electron density, and similar to a Maxwellian distribution in case of a high applied field frequency in the microwave range. Also experimental results show, that the assumption of a Maxwellian EEDF reproduces the measurements rather well, even in cases where the self–consistent solution of the Boltzmann equation predicts a different shape of the EEDF [60]. Therefore, a Maxwellian EEDF is assumed in the following, and $f(u)$ becomes (for derivation see Appendix B):

$$f(u) = \frac{2}{\bar{u}^2}\,\sqrt{u}\,\exp\left(-\frac{2}{\bar{u}}\,u\right). \tag{3.5}$$

Taking into account the typical mean electron energy range of $2\ldots10\,\mathrm{eV}$ as mentioned above, the reaction rate k_X from eq. (3.2) can be written as

$$k_\mathrm{X} \approx \frac{2}{\bar{u}^2}\sqrt{\frac{2}{m_\mathrm{e}}}\int_0^{50\,\mathrm{eV}} \sigma_\mathrm{X}(u)\,u^{\frac{3}{2}}\,\exp\left(-\frac{2}{\bar{u}}\,u\right)\mathrm{d}u. \tag{3.6}$$

Since k_x denotes the reaction rate per electron, the potential total reaction rate K_x for a process x is given by multiplying k_x with the free electron density:

$$K_\mathrm{x} = k_\mathrm{x}\, n_\mathrm{e}\,. \tag{3.7}$$

It is important to note, that k_x does not take into account the density n_n of atoms or molecules which are involved in a given electron impact process x, i.e. the density of the neutral collisional partners. Therefore, the collision frequency per electron ν_x is introduced as

$$\nu_\mathrm{x} = n_\mathrm{n}\, k_\mathrm{x} \tag{3.8}$$

Consequently, one obtains the total reaction rate density $\mathcal{R}_\mathrm{x}$ for a process x multiplying the collision frequency with the free electron density

$$\mathcal{R}_\mathrm{x} = \nu_\mathrm{x}\, n_\mathrm{e} = K_\mathrm{x}\, n_\mathrm{n}\,, \tag{3.9}$$

and the total reaction rate for an electron driven process x in the plasma is given by

$$R_\mathrm{x} = \mathcal{R}_\mathrm{x}\, V_\mathrm{pl}, \tag{3.10}$$

where V_pl is the plasma volume.
Another key parameter is the power loss per electron Θ. As the electrons loose their power gained from the hf–field via inelastic and elastic collisions with the neutral gas components, Θ is given as the sum over all processes x of the product of collison frequency and energy loss:

$$\Theta = \sum_\mathrm{x} \nu_\mathrm{x}\, U_\mathrm{x}, \tag{3.11}$$

where U_x denotes the energy lost by the electron during process x.
The power density ρ_pl in the discharge under given conditions is therefore given by

$$\rho_\mathrm{pl} = n_\mathrm{e}\,\Theta \tag{3.12}$$

and the total power needed to sustain the discharge by

$$P_\mathrm{pl} = \rho_\mathrm{pl}\, V_\mathrm{pl}\,. \tag{3.13}$$

3.2 Electron–neutral collisions

3.2.1 Inelastic collisions

The dominating inelastic electron impact processes (x = in) in a hydrogen discharge are listed in table 8.6 (according to refs. [61, 62] and references listed therein). Vibrational levels of the molecules (R 1) are excited already at low electron energies. Dissociation (R 2) occurs mainly via excitation of the first molecular triplet $^3\Sigma_u^+$ state, and the dominant

Vibrational exitation	R 1: $e^- + H_2 \rightarrow H_2^{vib} + e^-$
Dissociation	R 2: $e^- + H_2 \rightarrow H + H + e^-$
Ionisation	R 3: $e^- + H_2 \rightarrow H_2^+ + e^- + e^-$ R 4: $e^- + H \rightarrow H^+ + e^- + e^-$
Exitation of H atoms	R 5: $e^- + H \rightarrow H\ (2p) + e^-$ R 6: $e^- + H \rightarrow H\ (2s) + e^-$

Tab. 3.1: Dominant inelastic electron impact processes in a hydrogen glow discharge.

molecular ionisation reaction is the direct production of H_2^+ (R 3). Due to dissociation also the inelastic atomic processes have to be considered, which are ionisation (R 4) and excitation mainly to the 2 p–level (R 5) and only in second order to the 2 s–level (R 6). Atomic ion production from dissociative ionisation of molecules and atomic excitation to higher levels can be neglected.
In fig. 3.1, the cross sections for the above listed inelastic electron impact processes are plotted as a function of electron energy. Each graph has been parameterized to fit the experimental data given in refs. [62, 28, 64]. The corresponding parametrization functions are listed in table C.1. All cross sections show a strong increase at their onset energy and

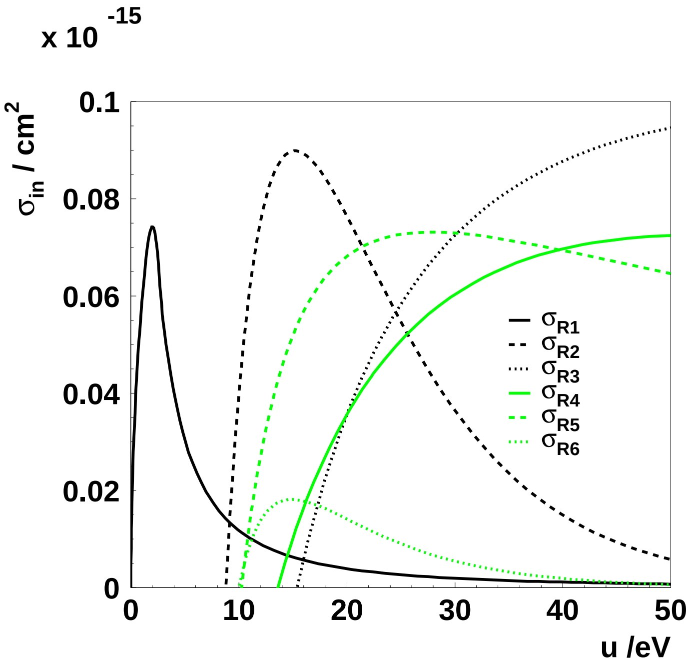

Fig. 3.1: Inelastic cross sections σ_{in} for the processes R 1 – R 6 listed in table 1 as a function of the electron energy u. The curves are a parametrization of experimental data.

decrease nearly exponentially after reaching their maximum. The ionisation and atomic exciation cross sections are quite similar except for excitation of the atomic 2 s–level, which has a substantially lower cross section. For low energies $u = 0.1 \ldots 8\,\text{eV}$, vibrational levels are predominantly excited with a maximum in the total vibrational cross section at around

3 eV. The dissociation cross section rises strongly beyond its onset energy of 8.8 eV with increasing electron energy up to its maximum at 16.5 eV and then decreases rapidly.

The inelastic reaction rate k_{in} is obtained from eq. (3.6) as

$$k_{\text{in}} \approx \frac{2}{\bar{u}^2}\sqrt{\frac{2}{m_{\text{e}}}}\int_{U_{\text{onset}}}^{50\,\text{eV}} \sigma_{\text{in}}(u)\, u^{\frac{3}{2}} \exp\left(-\frac{2}{\bar{u}}\,u\right) \mathrm{d}u = k_{\text{in}}\,(\bar{u}) \tag{3.14}$$

and can be calculated numerically taking into account the parametrization of the inleastic cross sections from above. The dependence of the calculated rates k_{in} on the mean electron energy is shown in fig. 3.2. Below a mean electron energy of about 6.5 eV, the rate for

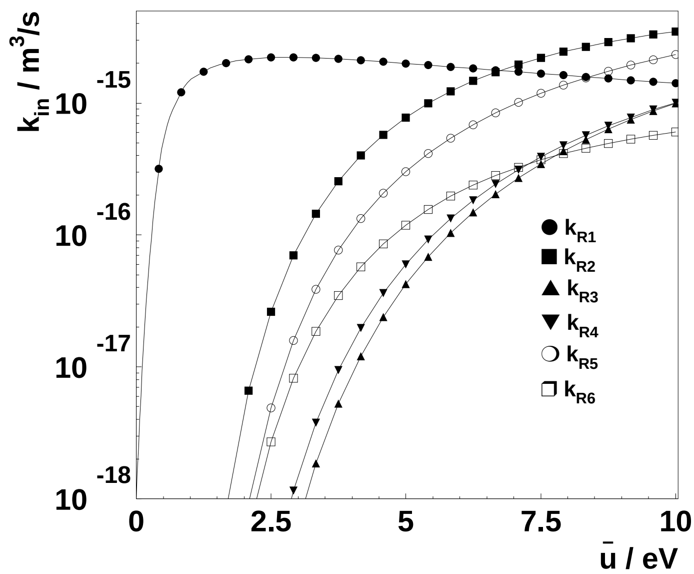

Fig. 3.2: Calculated rates k_{in} for the inelastic processes R 1 – R 6 listed in table 1 as a function of mean electron energy $\bar{u}$ under the assumption of a Maxwellian electron energy distribution function.

vibrational excitation k_{R1} dominates due to the low onset energy. k_{R1} rises steeply to $2 \times 10^{-15}\,\text{m}^3/\text{s}$ at $\bar{u} = 2\,\text{eV}$ and then stays nearly constant. All other rates start to increase strongly with the mean electron energy at higher $\bar{u}$ values, amongst which the dissociation rate k_{R2} clearly dominates reaching a value of $3 \times 10^{-15}\,\text{m}^3/\text{s}$ at $\bar{u} = 10\,\text{eV}$. As a consequence of the similar evolution of their cross sections, the rates for molecular and atomic ionisation, k_{R3} and k_{R4}, behave quite similar, too. Due to the high onset energy of both processes, the rates overcome $1 \times 10^{-18}\,\text{m}^3/\text{s}$ only at $\bar{u} \approx 3\,\text{eV}$ and reach a value of about $8 \times 10^{-16}\,\text{m}^3/\text{s}$ at 10 eV. The rates for the two atomic excitation processes are nearly equal at mean electron energies below 2.5 eV as a result of the same onset energy. However, due to the higher cross section, k_{R5} for excitation of the 2 p–level rises stronger and reaches a value of $2 \times 10^{-15}\,\text{m}^3/\text{s}$ at $\bar{u} = 10\,\text{eV}$, whereas k_{R5} for excitation of the 2 s–level is a factor of 4 lower.

Because of dissociation, the neutral gas density is composed of the molecular and the atomic density: $n_{\text{n}} = n_{\text{m}} + n_{\text{a}}$. This has to be considered for the calculation of the total inelastic collision frequency $\nu_{\rm in,tot}$ from eq. (3.8), and one obtains:

$$\nu_{\rm in,tot} = n_{\rm m} \sum_{l=1}^{3} k_{{\rm R}\,l} + n_{\rm a} \sum_{l=4}^{6} k_{{\rm R}\,l}. \tag{3.15}$$

The two partial densities are linked with the total neutral density $n_{\rm n}$ via the degree of dissociation $\alpha_{\rm pl}$ in the plasma as follows:

$$\alpha_{\rm pl} = \frac{n_{\rm a}}{n_{\rm a} + 2\,n_{\rm m}}. \tag{3.16}$$

Since one molecule is dissociated into two atoms, one can write

$$n_{\rm a} = 2\left(n_{\rm m}^{\rm off} - n_{\rm m}\right), \quad \text{and thus} \quad \alpha_{\rm pl} = 1 - \frac{n_{\rm m}}{n_{\rm m}^{\rm off}}, \tag{3.17}$$

where $n_{\rm m}^{\rm off}$ is the molecular density when the discharge is off.
Therefore, $n_{\rm a}$ and $\alpha_{\rm pl}$ can be determined for a given value of $n_{\rm m}$ from eqs. (3.16) and (3.17), taking into account that the initial neutral density $n_{\rm n}^0$ before the discharge is switched on is equal to the molecular density $n_{\rm m}^{\rm off}$. In fig. 3.3, $\nu_{\rm in,tot}$ is shown as a function of mean electron energy for various atomic fractions $\alpha_{\rm pl}$ in the plasma. It is found,

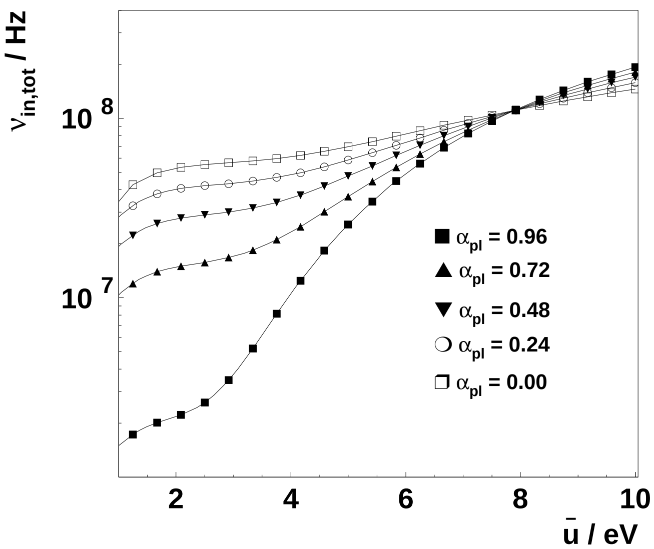

Fig. 3.3: Calculated total inelastic collision frequency $\nu_{\rm in,tot}$ as a function of mean electron energy $\bar{u}$, under the assumption of a Maxwellian EEDF for various degrees of dissociation $\alpha_{\rm pl}$ in the plasma. The initial neutral gas density used was 2.47×10^{22} m^{-3} corresponding to a pressure of 1 mbar at 293 K.

that $\nu_{\rm in,tot}$ increases for decreasing $\alpha_{\rm pl}$ at a given mean electron energy $\bar{u}$ which is very pronounced for low values of $\bar{u}$. This results from the evolution of the dissociation and the total vibrational cross sections, which reach their maximum already at low electron energies. At higher mean electron energies, the influence of a change in $\alpha_{\rm pl}$ is reduced continuously due to an increased influence of ionisation reactions, the cross sections of which have a similar shape for both atoms and molecules. For $\bar{u} \geq 8\,\mathrm{eV}$, the total inelastic collision frequency becomes even higher for higher values of α_{pl} than for lower ones.

Calculating the power loss per electron Θ_{in} due to inleastic collisions, one has to take into account, that the energy lost by an electron during an inelastic process R $l\,(l = 1...6)$, is equal to its onset energy $U_{\mathrm{onset,R}\,l}$ given in Appendix C. Hence, one obtains from eqs. (3.11) and (3.15):

$$\Theta_{\mathrm{in}} = n_{\mathrm{m}} \sum_{l=1}^{3} k_{\mathrm{R}\,l}\, U_{\mathrm{onset,R}\,l} + n_{\mathrm{a}} \sum_{l=4}^{6} k_{\mathrm{R}\,l}\, U_{\mathrm{onset,R}\,l}. \tag{3.18}$$

The depence of Θ_{in} on the mean electron energy for various degrees of dissociation in the plasma is shown in fig. 3.4. In analogy to the evolution of the total inelastic collision

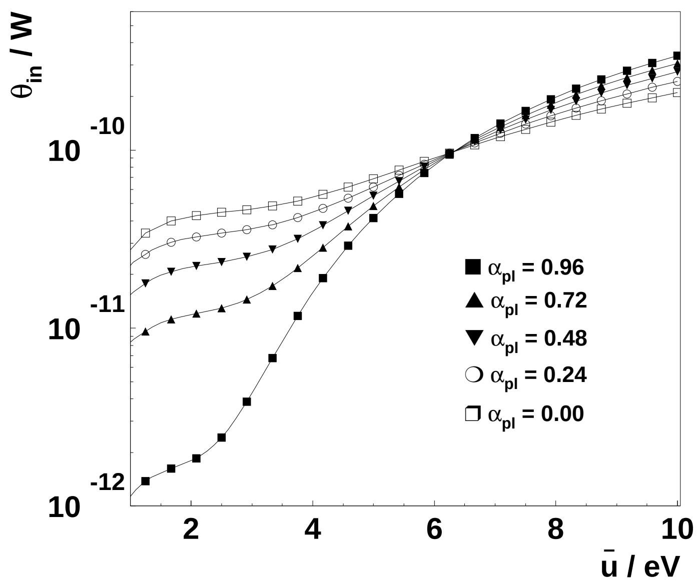

Fig. 3.4: Calculated power loss per electron Θ_{in} due to inelastic collisions for an initial neutral gas density of $2.47 \times 10^{22}\,\mathrm{m}^{-3}$ as a function of mean electron energy $\bar{u}$ under the assumption of a Maxwellian EEDF for various degrees of dissociation α_{pl} in the plasma.

frequency in fig. 3.3, the inelastic power loss per electron increases strongly with decreasing α_{pl} at a given mean electron energy for low values of $\bar{u}$ and increases with increasing α_{pl} for $\bar{u} \geq 6.5\,\mathrm{eV}$.

3.2.2 Elastic collisions

In case of elastic electron–neutral collisions in hydrogen, the cross section is inversely proportional to the electron velocity [65]. Hence, taking into account the normalization of the EEDF from eq. (3.3), the elastic reaction rates become a constant:

$$k_{\text{el-a,m}} = \sqrt{\frac{2}{m_{\text{e}}}} \int_0^{+\infty} \frac{C_{\text{el-a,m}}}{\sqrt{u}}\, u\, f(u)\, \mathrm{d}u = \sqrt{\frac{2}{m_{\text{e}}}}\, C_{\text{el-a,m}}\,, \tag{3.19}$$

where $C_{\text{el-a,m}}$ are the constants for the atomic (a) and the molecular (m) elastic cross section, respectively.
The data found in the literature for the elastic collision frequency in hydrogen do not specify the atomic fraction, and the values given correspond to $k_{\text{el}} = 1.7 \times 10^{-13}\,\text{m}^3/\text{s}$ [65, 66] and $1.4 \times 10^{-13}\,\text{m}^3/\text{s}$ [57], respectively. Parametrizing the data for the elastic cross sections given in [62] yields $C_{\text{el-a}} = 2.2 \times 10^{-15}\,\text{cm}^2/\sqrt{\text{eV}}$ and $C_{\text{el-m}} = 3.0 \times 10^{-15}\,\text{cm}^2/\sqrt{\text{eV}}$ and one obtains for the reaction rates $1.3 \times 10^{-13}\,\text{m}^3/\text{s}$ and $1.8 \times 10^{-13}\,\text{m}^3/\text{s}$, which is in good agreement with the above values.
Consequently, the elastic collision frequency

$$\nu_{\text{el,tot}} = n_{\text{m}}\, k_{\text{el-m}} + n_{\text{a}}\, k_{\text{el-a}} \tag{3.20}$$

is only slightly affected by a variation of the atomic fraction and is in the range of $(3.2 \ldots 4.5) \times 10^9\,\text{Hz}$ at the standard initial gas density of $2.47 \times 10^{22}\,\text{m}^{-3}$. As a result, depending on α_{pl}, $\nu_{\text{el,tot}}$ is a factor of about $50 \ldots 1000$ higher than the inelastic collision frequencies shown in fig. 3.3.

For the calculation of the power loss per electron Θ_{el} due to elastic collisions, one has to take into account the mean elastic energy losses $U'_{\text{a,m}}$ for atomic and molecular collisions, which are given by:

$$U'_{\text{a,m}} = 4\, \frac{m_{\text{e}}}{m_{\text{a,m}}}\, \bar{u}\,, \tag{3.21}$$

where m_{a} and m_{m} denote the atomic and molecular hydrogen mass, respectively.
Hence, one obtains for the elastic power loss per electron:

$$\Theta_{\text{el}} = n_{\text{m}}\, k_{\text{el-m}}\, U'_{\text{m}} + n_{\text{a}}\, k_{\text{el-a}}\, U'_{\text{a}}. \tag{3.22}$$

The elastic power losses for various degrees of dissociation are shown in fig. 3.5. In contrast to the evolution of the inelastic power loss, Θ_{el} rises with increasing α_{pl} at a given mean electron energy because of the mass dependence in the energy loss. However, although the elastic collsion frequency is much higher than the inelastic one, the elastic power losses are clearly lower than the inelastic losses.

3.2.3 Summary

The dominant electron impact reaction rates, collision frequencies and power losses in the hydrogen discharge for both inelastic and elastic reactions have been calculated for typical gas conditions of a dissociator. The Maxwellian electron energy distribution function used seems to be a valid assumption based on theoretical studies on the electron kinetics in low

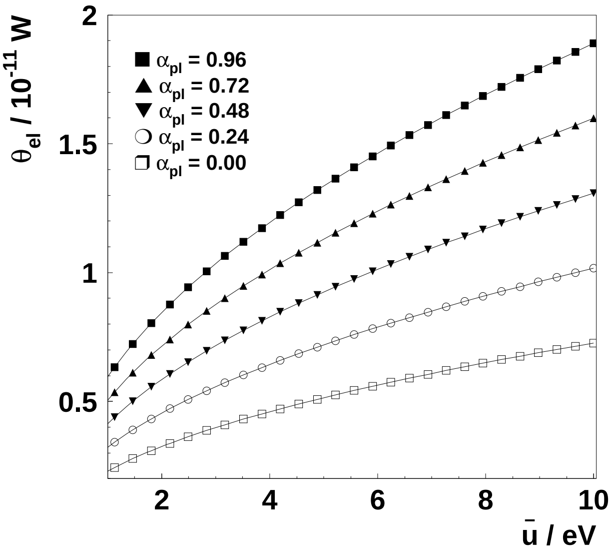

Fig. 3.5: Calculated power loss per electron Θ_{el} due to elastic collisions for an initial neutral gas density of $2.47 \times 10^{22}\,\text{m}^{-3}$ as a function of the mean electron energy $\bar{u}$ for various degrees of dissociation α_{pl} in the plasma.

temperature plasmas. The collision frequency of the various excitation processes depends strongly on the degree of dissociation. In order to obtain a maximum reaction rate for dissociation k_{R2}, one has to aim for a high mean electron energy $\bar{u}$. However, for a maximum total potential dissociation rate K_{R2}, also a high electron density is required as can be seen from eq. (3.7). Hence, for a complete description of the problem one has to consider two loss mechanisms affecting K_{R2}: the reduction of the free electron density n_{e} and the recombination of hydrogen atoms to molecules. Both mechanisms are discussed in the following sections 3.3 and 3.5.
Another important conclusion arises from the evolution of the total power loss per electron in the discharge, which is composed of the inleastic and elastic power loss:

$$\Theta_{\text{tot}} = \Theta_{\text{in}} + \Theta_{\text{el}}. \tag{3.23}$$

The dependence of Θ_{tot} on the mean electron energy is shown in fig. 3.6. Comparing fig. 3.6 with figs. 3.4 and 3.5, one can see that Θ_{tot} is dominated by the inelastic losses only for higher mean electron energies and lower degrees of dissociation. In contrast to discharges in heavier gases, the relatively large elastic contribution to the power loss leads to a considerable heating of the neutral gas components and consequently to a high neutral gas temperature, which is an important aspect of atomic loss processes discussed in section 3.5. Moreover, a considerably higher electron power loss is expected for a low degree of dissociation for lower values of the mean electron energy ($\bar{u} \leq 4\,\text{eV}$) and an opposite behaviour for $\bar{u} > 8\,\text{eV}$.

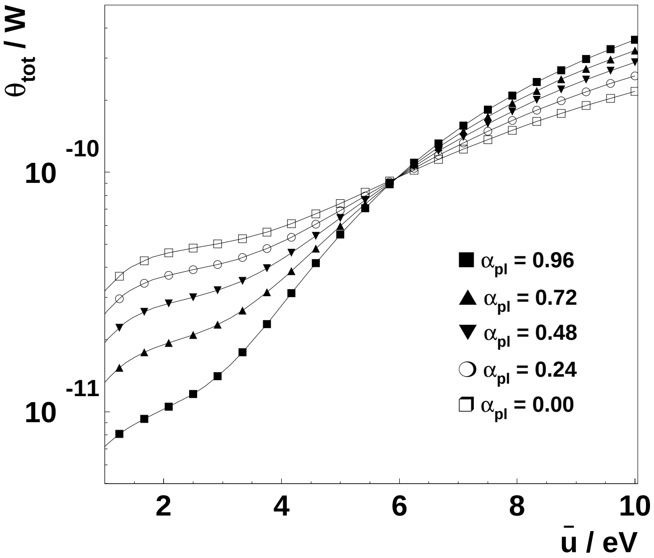

Fig. 3.6: Calculated total power loss per electron Θ_{tot} for an initial neutral gas density of 2.47×10^{22} m^{-3} as a function of mean electron energy $\bar{u}$ under the assumption of a Maxwellian EEDF for various degrees of dissociation α_{pl} in the plasma.

3.3 Balance of charged particles

The influence of the macroscopic parameters such as gas pressure and temperature as well as applied hf power on the mean electron energy and electron density can be quantitatively understood considering the balance of charged particles in the discharge. The required over–all neutrality of the steady–state plasma results in an equality of the production and loss rate of electrons and ions. Since the charged particles are produced via ionisation, one can write

$$\nu_{\mathrm{ion}} = \nu_{\mathrm{loss}}, \tag{3.24}$$

where $\nu_{\mathrm{ion}} = \nu_{\mathrm{R3}} + \nu_{\mathrm{R4}}$ is the ionisation frequency and ν_{loss} the frequency for charged particle losses due to recombination of a free electron with a H^+ or a H_2^+ ion.
The four possible recombination mechanisms are described in the following.

3.3.1 Diffusion losses

Since densities of the charged particles vanish at the discharge tube walls, a gradient in the electron and ion density builts up, which results in diffusion of electrons and ions to the discharge tube walls, followed by recombination on the surface:

$$\mathrm{H}_{(2)}^+ + \mathrm{e}^- + \mathrm{M}_{\mathrm{wall}} \rightarrow \mathrm{H}_{(2)} + \mathrm{M}_{\mathrm{wall}},$$

where $\mathrm{H}_{(2)}^+$ is either an H^+ or an H_2^+ ion and $\mathrm{M}_{\mathrm{wall}}$, required as third collisional partner, is either a molecule from the discharge tube wall or a gas particle adsorbed on it.

The frequency for diffusion losses of charged particles in a discharge sustained in a long, cylindrical tube can be written as [65]

$$\nu_{\text{diff}} = \frac{D}{\Lambda^2}, \quad \text{with } \Lambda = \frac{r_{\text{dt}}}{2.405}, \tag{3.25}$$

where D is the diffusion coefficient, Λ the diffusion length, and r_{dt} the radius of the discharge tube.
As a consequence of their lower mass and higher energies, the free electrons diffuse much faster than the ions. Therefore, a negative space charge field builds up at the discharge tube wall retarding free electron and enhancing ion diffusion. This mechanism is called ambipolar diffusion, and the diffusion coefficient is given by [33]:

$$D_{\text{am}} = b'_{\text{ion}} \frac{\bar{u}\,[\text{eV}]}{2\,n_{\text{n}}}, \tag{3.26}$$

where $b'_{\text{ion}} = 1.59 \times 10^{22}\,\text{m}^{-1}\,\text{s}^{-1}\,\text{eV}^{-1}$ is the density normalized mobility constant for H_2^+ ions in H_2.
As shown in ref. [72], an enhancement of ambipolar diffusion towards free electron diffusion in case of hf sustained discharges has not to be taken into account for the gas and discharge conditions considered here.

3.3.2 Two–body recombination

Two–body recombination in the volume may occur radiatively, i.e. under emission of a photon:

$$H^+_{(2)} + e^- \rightarrow H_{(2)} + \gamma$$

In addition, molecular ions can recombine dissociatively, i.e., the molecule formed through the neutralisation process dissociates in two atoms:

$$H_2^+ + e^- \rightarrow 2\,H$$

The radiative recombination frequency is proportional to the density of charged particles and is given by

$$\nu_{\text{rad-rec}} = k_{\text{rad-rec}}(n_{\text{e}},\, \bar{u})\, n_{\text{e}} \tag{3.27}$$

where the reaction rate $k_{\text{rad-rec}}$ for radiative recombination in general is a function of the mean electron energy and the electron density.
The $k_{\text{rad-rec}}$ values given in ref. [65] for radiative recombination of H^+ ions are nearly constant for $n_{\text{e}} = 10^{14} \ldots 10^{19}\,\text{m}^{-3}$, and range between $10^{-19} \ldots 10^{-18}\,\text{m}^3\,\text{s}^{-1}$ for mean electron energies of more than 2 eV. Similar values can be expected for radiative recombination of molecular ions.
The frequency for dissociative recombination of molecular ions is given as

$$\nu_{\text{diss-rec}} = k_{\text{diss-rec}}\, n_{\text{e}} \tag{3.28}$$

with $k_{\text{diss-rec}} \approx 10^{-16} \ldots 10^{-14}\,\text{m}^3\,\text{s}^{-1}$ [67].
It can be concluded, that charged particle losses via dissociative recombination are clearly dominating the radiative recombination losses provided the molecular ion density is not negligibly small compared to the atomic ion density, i.e., for degrees of dissociation smaller than unity.

3.3.3 Three–body recombination

Three–body recombination in the volume, where the third collisional partner $\text{M}_{\text{3-b-rec}}$ is either a neutral or a charged particle:

$$\text{H}^+_{(2)} + \text{e}^- + \text{M}_{\text{3-b-r}} \rightarrow \text{H}_{(2)} + \text{M}_{\text{3-b-rec}}$$

The frequency for charged particle losses via three–body recombination in the volume is given as

$$\nu_{\text{3-b-rec}} = k_{\text{3-b-rec}}\, n_{\text{e}}, \tag{3.29}$$

with a value of the rate constant $k_{\text{3-b-rec}}$ in hydrogen of $1.6 \times 10^{-13}\,\text{m}^3\,\text{s}^{-1}$ [57].

3.3.4 Gas flow effects

Gas flow induced charged particle losses arise, because one electron–ion pair leaving the discharge region downstream is replaced by a neutral flowing into the discharge at its upstream end. Due to the substantially higher frequencies for diffusion losses and also for three–body recombination, gas flow induced losses are negligible, as has also been shown in ref. [68] for a helium discharge under gas conditions similar to the scenario considered here.

3.3.5 Summary

The total charged particle loss frequency can be written as

$$\nu_{\text{loss}} = \nu_{\text{diff}} + \nu_{\text{2-b-v}} + \nu_{\text{3-b-v}} + \nu_{\text{flux}}\,, \tag{3.30}$$

where ν_{diff}, $\nu_{\text{2-b-v}}$, $\nu_{\text{3-b-v}}$ and ν_{flux} are the frequencies for diffusion losses, two–body recombination, three–body volume recombination and throughput induced losses, respectively. Assuming a typical mean electron energy of $\bar{u} = 5\,\text{eV}$, an electron density of $n_{\text{e}} = 10^{17}\,\text{m}^{-3}$ and the standard gas conditions from above, it is found, that diffusion losses with $\nu_{\text{diff-am}} = 3.7 \ldots 7.4 \times 10^5\,\text{Hz}$ (depending on α_{pl}), dominate the charged particle losses followed by volume recombination with $\nu_{\text{3-b-rec}} = 1.6 \times 10^4\,\text{Hz}$.
Therefore eq. (3.24) becomes

$$\nu_{\text{ion}} = \nu_{\text{loss}} \approx \nu_{\text{diff-am}}\,. \tag{3.31}$$

Dividing this equation by $(\bar{u}\, n_{\rm n})$, taking into account eq. (3.8), yields a fundamental result:

$$\frac{k_{\rm ion}}{\bar{u}\,[\rm eV]} = \frac{b'_{\rm ion}\,(2.405)^2}{2\, n_{\rm n}^2\, r_{\rm dt}^2}\,, \tag{3.32}$$

where $k_{\rm ion} = k_{\rm R3} \approx k_{\rm R4}$ is the reaction rate for ionization shown in fig. 3.2.
Thus, if diffusion dominates the charged particle losses, the mean electron energy is solely determined by the discharge tube diameter and the neutral gas density.
The determination of $\bar{u}$ is illustrated in fig. 3.7, where $k_{\rm ion}/\bar{u}$ is plotted as a function of the mean electron energy $\bar{u}$. $\bar{u}$ has been determined from eq. (3.32) for the two limiting

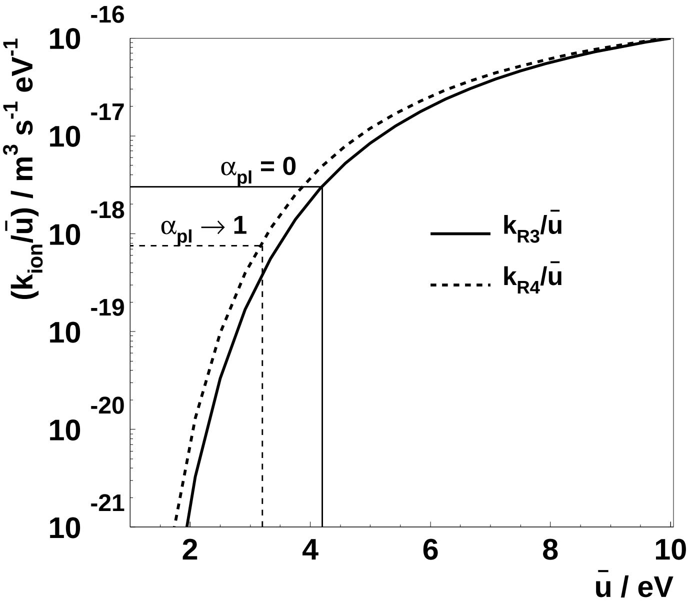

Fig. 3.7: Calculated reaction rates for atomic (dashed curve) and molecular (solid curve) ionization divided by the mean electron energy, $k_{\rm R4,3}/\bar{u}$ as function of the mean electron energy $\bar{u}$. The vertical lines denote the values obtained in case the charged particle loss is dominated by diffusion (dashed line: $\alpha_{\rm pl} \rightarrow 1$; solid line: $\alpha_{\rm pl} = 0$).

cases $\alpha_{\rm pl} = 0$ and $\alpha_{\rm pl} \rightarrow 1$, which is indicated by the vertical lines.

Considering an initial neutral density of $2.47 \times 10^{22}\,{\rm m}^{-3}$ and a discharge tube radius of $r_{\rm dt} = 0.5\,{\rm cm}$, one finally obtains $\bar{u} = 4.2\,{\rm eV}$ for $\alpha_{\rm pl} = 0$ and $\bar{u} = 3.2\,{\rm eV}$ in case of $\alpha_{\rm pl} \rightarrow 1$.

3.4 Maximization of the dissociation rate

As shown above in eq. (3.32), the mean electron energy $\bar{u}$ will be fixed if the charged particle losses are dominated by diffusion. In this case, also the reaction rate $k_{\rm R2}$ is fixed, as can be seen in fig. 3.2. However, $\bar{u}$ also determines the total power loss per electron $\Theta_{\rm tot}$ for a given atomic fraction (see fig. 3.6). According to eq. (3.12), an increase in the power density ρ_{pl} will then in first order lead to an increase in the free electron density n_{e} . This prediction is confirmed by studies given in ref. [61] for a low pressure, ambipolar diffusion controlled hydrogen discharge. As consequence of a higher electron density, the total potential dissociation rate K_{R2} increases, since it is proportional to n_{e} (see eq. (3.7)). If ρ_{pl} and hence n_{e} is increased further, three body recombination will enhance the charged particle losses, resulting in an increased ionization frequency according to eq. (3.24). Consequently, the mean electron energy rises and, as shown in fig. 3.2, k_{R2} increases as well. Taking into account this secondary order effect, the dependence of n_{e} , $\bar{u}$, k_{R2} and K_{R2} on the power density ρ_{pl} have been calculated iteratively for the two limiting cases $\alpha_{\mathrm{pl}} = 0$ and $\alpha_{\mathrm{pl}} \rightarrow 1$, the results of the calculation being shown in fig. 3.8.

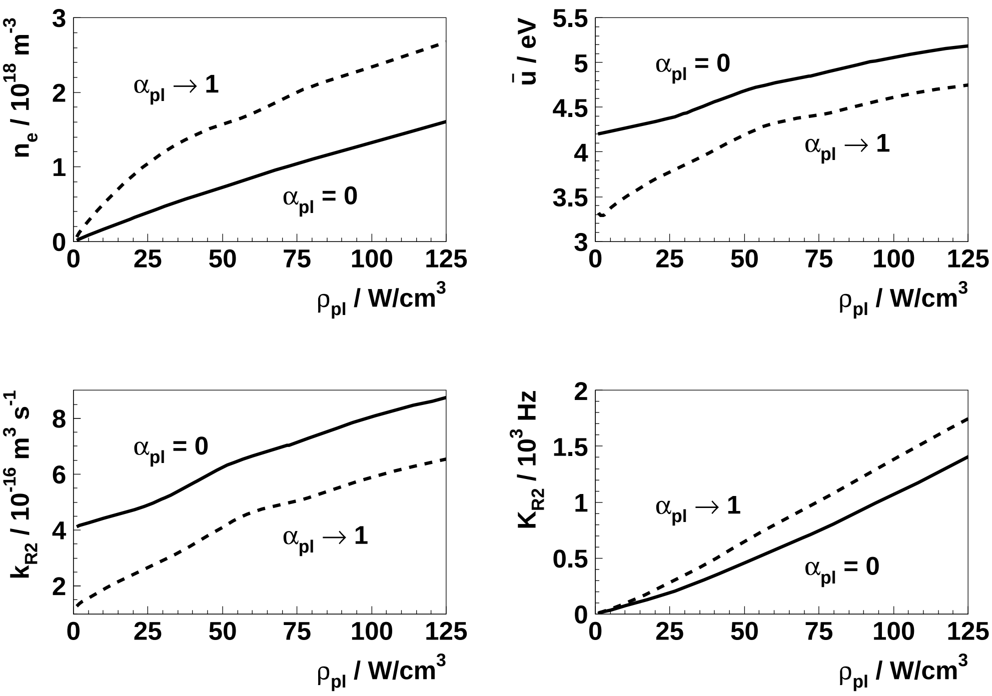

Fig. 3.8: Calculated electron densities n_{e} , mean electron energies $\bar{u}$, process and total potential rate for dissociation, k_{R2} and K_{R2}, respectively, as a function of power density ρ_{pl} in the discharge. The full and dashed curves curves show the calculation for an atomic fraction equal to zero and one, respectively.

It can be seen, that the atomic fraction has a clear influence on the electron density and the mean electron energy: highly dissociated plasmas have a lower mean electron energy but a higher electron density. This is a result of the increase in neutral density with α_{pl} (see eqs. (3.16) and (3.17)), which leads to a lower ambipolar diffusion coefficient (see eq. (3.26)) and consequently a lower value of $\bar{u}$ as can be seen from eq. (3.32). Taking into account the change of the total power loss per electron Θ_{tot} with atomic fraction and mean electron energy as shown in fig. 3.6, one obtains from eq. (3.12) an increase in n_{e} for a high degree of dissociation at a given power density in the discharge. The difference in $\bar{u}$ results in a lower dissociation rate k_{R2} for a high atomic fraction. However, regarding the total potential dissociation rate K_{R2} defined in eq. (3.7), the lower value of k_{R2} in case of $\alpha_{\mathrm{pl}} \to 1$ is overcompensated by a higher electron density so that K_{R2} is a factor of about 1.2 times higher for a highly dissociated discharge.

In summary, if a maximum potential total dissociation rate is anticipated, the plasma source has to be designed in such a way, that the coupling of the hf field provides a maximum power density in the discharge.
However, as a maximum atomic fraction in the plasma is required, the influence of a high power density on the loss processes of atoms in the plasma source have to be considered. The atomic loss processes are discussed in the following section.

3.5 Atomic losses

In analogy to the charged particle losses, hydrogen atoms are lost by surface or volume recombination of two atoms to a molecule and by throughput–induced effects.
For the recombination of two hydrogen atoms to a molecule, a third collision partner is needed to conserve energy and momentum. The atomic recombination process can be written as:

$$2\,\mathrm{H} + \mathrm{M} \to \mathrm{H}_2 + \mathrm{M} + E_{\mathrm{b}}\,,$$

where $E_{\mathrm{b}} \approx 4.5\,\mathrm{eV}$ is the binding energy of the molecule [63]. As shall be shown in the following, the atoms can either recombine at the wall of the discharge tube or in the volume.

3.5.1 Surface recombination

In case of surface recombination, hydrogen atoms collide with another atom adsorbed at the discharge tube wall. In this case, M is a hydrogen atom or molecule or a molecule from the discharge tube material, and E_{b} will mainly be deposited on the wall. Since the mean free path λ_{a} of hydrogen atoms in the discharge for the typical pressure range is small compared to the discharge tube dimensions ($\lambda_{\mathrm{a}} \approx 10^{-2}\,\mathrm{cm}$ according to eq. (2.2) and $2\,r_{\mathrm{dt}} \approx 1\,\mathrm{cm}$), the transport to the wall can be described via diffusion, in analogy to the charged particle losses. Hence one can write for the wall recombination frequency (see eq. (3.25)):

$$\nu_{\text{ar-w}} = \frac{(2.405)^2\,D_{\mathrm{a}}}{r_{\mathrm{dt}}^2}\,\gamma, \tag{3.33}$$

where D_{a} is the diffusion coefficient for hydrogen atoms and γ the surface recombination coefficient of the discharge tube, which gives the probability of recombination per wall

collision.
The atomic diffusion coefficient can be written as [33]

$$D_{\mathrm{a}} = \frac{1}{3}\,\bar{v}_{\mathrm{a}}\,\lambda_{\mathrm{a}} = \frac{1}{3}\sqrt{\frac{2\,k\,T_{\mathrm{n}}}{m_{\mathrm{a}}}}\,\lambda_{\mathrm{a}}\,, \tag{3.34}$$

where $\bar{v}_{\mathrm{a}}$ is the mean thermal velocity of hydrogen atoms.
Neglecting the minor change in λ_{a} due to a different degree of dissociation, one finally obtains for the wall recombination frequency of hydrogen atoms at the discharge tube wall

$$\nu_{\text{ar-w}} \approx \frac{(2.405)^2}{12\,\pi}\sqrt{\frac{k\,T_{\mathrm{n}}}{m_{\mathrm{a}}}}\,\frac{\gamma}{r_{\mathrm{m}}^2\,n_{\mathrm{n}}\,r_{\mathrm{dt}}^2}\,, \tag{3.35}$$

where $r_{\mathrm{m}} = 1.35 \times 10^{-10}\,\mathrm{m}$ is the kinetic radius of hydrogen molecules [33].
The wall recombination coefficient γ depends on wall temperature and material. In the following, the discussion is restricted to wall recombination properties of borosilicate or quartz glass. The recombination coefficients γ_{glass} presented in the literature vary strongly. For example, at a surface temperature of $T_{\mathrm{s}} = 300\,\mathrm{K}$, $\gamma_{\mathrm{glass}} = 3 \times 10^{-3}$ is given in ref. [73], 2.15×10^{-5} in ref. [74] and 7×10^{-4} in ref. [75]. However, all authors report an increase in γ_{glass} of about two orders of magnitude when the surface temperature is increased from 300 K to 1000 K. The most recent data on γ_{glass} from ref. [76], which give the lowest values of all references cited above, are shown in fig. 3.9 as a function of surface temperature. γ_{glass} can be parametrized by an exponential function:

$$\gamma_{\mathrm{glass}} = 8.41 \times 10^{-6}\,\exp\left(4.82 \times 10^{-3}\,\frac{T_{\mathrm{s}}}{\mathrm{K}}\right) \tag{3.36}$$

It has to be mentioned, that all γ_{glass} values presented are measured in the afterglow of the discharge. However, as pointed out in ref. [69], the surface recombination coefficient in the discharge region might be substantially higher.

3.5.2 Volume recombination

In case of volume recombination, hydrogen atoms collide in the gas phase where M is either another hydrogen atom or a molecule. E_{b} is transferred to the three collision partners. The volume recombination rate is proportional to the square of the atomic density in the discharge and is given by

$$\nu_{\text{ar-v}} = k_{\text{ar-v}}\,n_{\mathrm{a}}^2\,, \tag{3.37}$$

where $k_{\text{ar-v}}$ is the volume recombination rate constant.
Volume recombination in the afterglow of a hydrogen discharge with a low degree of dissociation has been investigated in ref. [77]. The value for the recombination rate constant in case of $\mathrm{M} = \mathrm{H_2}$ has been determined to $k_{\text{ar-v}} = (8.1 \pm 0.4) \times 10^{-45}\,\mathrm{m^6\,s^{-1}}$ at a

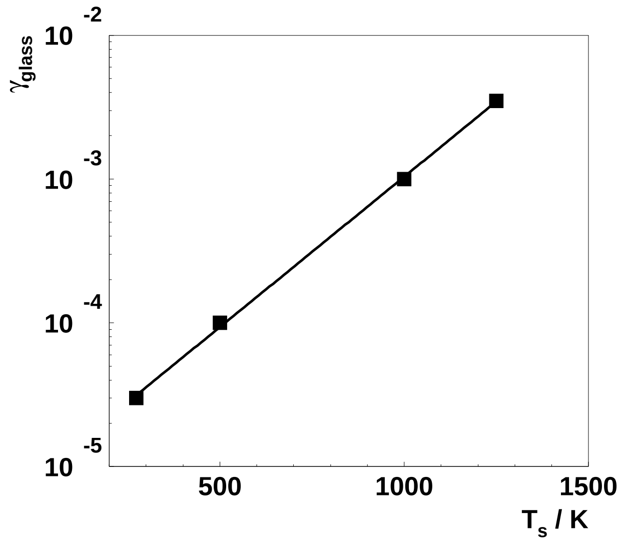

Fig. 3.9: Surface recombination coefficient γ_{glass} on quartz glass as a function of surface temperature T_{s}. The full squares are data given in ref. [76], the line is an exponential fit to the data points.

gas temperature of 298 K. Unfortunately, the investigations of $\nu_{\text{ar-v}}$ have been restricted to a gas temperature range of $T_{\text{n}} = 77 \ldots 298\,\text{K}$. As shown in fig. 3.10, an estimate of $k_{\text{ar-v}}$ for the gas temperature range within the discharge between 300 K and 2000 K is obtained extrapolating the low temperature data with the suggested $T_{\text{n}}^{-0.68}$–dependence as follows:

$$k_{\text{ar-v}} = 4 \times 10^{-43}\,\frac{\text{m}^6}{\text{s}}\left(\frac{T_{\text{n}}}{\text{K}}\right)^{-0.68}. \tag{3.38}$$

The validity of the extrapolation to high gas temperatures is also confirmed by theoretical

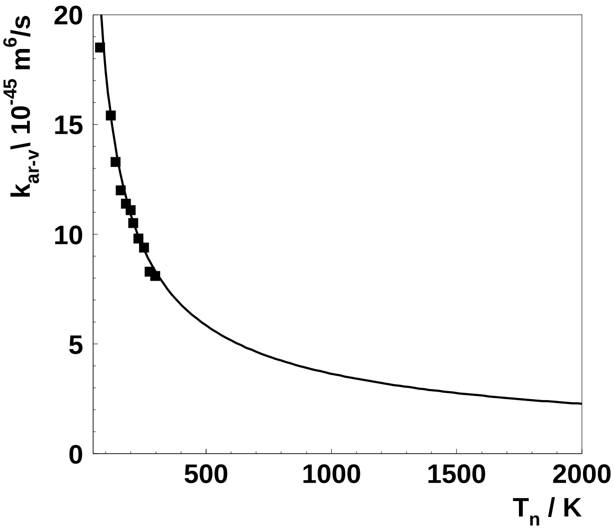

Fig. 3.10: Volume recombination coefficient $k_{\mathsf{ar\text{-}v}}$ as a function of gas temperature T_{n}. The squares are data given in ref. [77], the line represents an extrapolation of the data to higher gas temperatures with the $T_{\mathsf{n}}^{-0.68}$–dependence suggested therein.

predictions given in ref. [78].

3.5.3 Gas flow induced losses

The fact that atoms leave the discharge region and are replaced by molecules entering the discharge leads to an effective contribution to the atomic losses. The loss rate of hydrogen atoms can be written as

$$\left(\frac{\mathrm{d}N_{\mathrm{a}}(t)}{\mathrm{d}t}\right)_{\mathrm{flux}} = -\frac{N_{\mathrm{a}}(t)}{t_{\mathrm{dwell}}}\,, \tag{3.39}$$

where the dwell time of a hydrogen atoms in the discharge is given as the quotient out of discharge length L and gas velocity v_{gas}:

$$t_{\mathrm{dwell}} = \frac{L}{v_{\mathrm{gas}}}\,, \quad v_{\mathrm{gas}} = \frac{Q'_{\mathrm{m}}}{n_{\mathrm{n}}^{0}\, r_{\mathrm{dt}}^{2}\, \pi}\,. \tag{3.40}$$

Consequently, one obtains for the solution of eq. (3.39):

$$N_{\mathrm{a}}(t) = N_{\mathrm{a}}(t=0)\, \exp\left(-\frac{Q'_{\mathrm{m}}}{n_{\mathrm{n}}^{0}\, V_{\mathrm{pl}}}\, t\right)\,. \tag{3.41}$$

Since the throughput induced atomic loss frequency is equal to the time constant in the exponential function above, one finally has:

$$\nu_{\mathrm{flux}} = \frac{Q'_{\mathrm{m}}}{n_{\mathrm{n}}^{0}\, V_{\mathrm{pl}}}\,. \tag{3.42}$$

3.5.4 Summary

The total atomic loss frequency can be written as

$$\nu_{\mathrm{ar}} = \nu_{\text{ar-w}} + \nu_{\text{ar-v}} + \nu_{\mathrm{flux}}\,. \tag{3.43}$$

In order to obtain a rough estimation for the various loss frequencies in the plasma, a gas and discharge tube wall temperature of 1000 K and 700 K have been assumed in addition to the sceanrio given at the beginning of this section. In table 3.2, the dominant loss frequencies appearing in eq. (3.43) are listed. It has to be mentioned, that the given values are based on the simple model assumption of a discharge tube pressure being independent of the gas throughput. Given are two values each for two degrees of dissociation, $\alpha_{\mathrm{pl}} = 0.5$ and 0.8, respectively. The results from table 3.2 show, that wall recombination and throughput effects contribute with the same order of magnitude to the atom losses for low gas throughputs. For high values of Q_{m}, ν_{flux} clearly dominates. However in case of the dissociator, the gas density increases with increasing gas throughput. Consequently, volume recombination will have a stronger influence, whereas the throughput induced losses will be on a lower level compared to the values shown in table 3.2.

gas throughput Q_m / mbar l/s	surface recombination $\nu_\text{ar-w}$ / Hz	volume recombination $\nu_\text{ar-v}$ / Hz	throughput induced losses ν_flux / Hz
0.5	27, 17	2.2, 5.6	34
1.0	27, 17	2.2, 5.6	67
5.0	27, 17	2.2, 5.6	335

Tab. 3.2: Atomic loss frequencies under typical gas and discharge conditions.

3.6 Estimate of the degree of dissociation

In the following, the the degree of dissociation will be estimated as a function of power density in the discharge based on the atomic production and loss mechanisms discussed above.

The time dependence of the atomic density in the discharge is described by

$$\frac{\mathrm{d}n_\mathrm{a}}{\mathrm{d}t} = K_\mathrm{R2}\, n_\mathrm{m} - \nu_\mathrm{ar}\, n_\mathrm{a}. \tag{3.44}$$

Asuming steady–state, one obtains $(\mathrm{d}n_\mathrm{a}/\mathrm{d}t) = 0$. Taking into account eq. (3.16), the degree of dissociation in the discharge can be expressed as

$$\alpha_\mathrm{pl} = \frac{K_\mathrm{R2}}{K_\mathrm{R2} + 2\,\nu_\mathrm{ar}}\,. \tag{3.45}$$

Hence, the degree of dissociation is determined by the total potential dissociation rate and the atomic loss frequency.

It has already been demonstrated, that K_R2 is enhanced by increasing the power density ρ_pl in the discharge (see fig. 3.8). In order to estimate the dependence of the total atomic loss frequency ν_ar, both the neutral gas and the discharge tube wall temperature, T_n and T_s, are assumed to rise linearly with the power density from 300 K up to 1500 K and 2000 K, respectively, at a power density of 125 W/cm^3. This assumption implies a sufficient cooling of the outer discharge tube surface, providing a moderate rise of the outer surface temperature with increasing ρ_pl.

It is important to note, that K_R2 and the various atomic loss frequencies depend on the atomic, molecular or total neutral gas density and thus show an implicit dependence on α_pl istself. Therefore, α_pl has been calculated iteratively. As mentioned before, the wall recombination coefficient on glass might be higher and might show a stronger increase with surface temperature as the measurements done in the afterglow of the discharge. On the other hand, surface recombination can be strongly compensated by an admixture of oxygen resulting in an effective reduction of γ and an appropriate treatment of the glass surface, as shall be shown later. One may also think of an enhanced discharge tube cooling yielding a lower increase of T_s with ρ_{pl} compared to assumption above. Facing this freedom in the description of the wall recombination losses, as an example three possible evolutions of γ as a function of T_s are considered. In order to describe the case of low wall recombination, γ' is set constant to 10^{-5}. $\gamma = \gamma_{glass}$ from eq. (3.36) denotes the behaviour described above, and for the case of a stronger rise in the wall recombination coefficient with temperature described by γ'', the exponent of γ is multiplied by a factor of 2. The result of the calculation is shown in fig. 3.11 for four different gas throughput values $Q_m = 0$, 1.0, 2.8 and 5.0 mbar l/s. It is found, that for high gas throuhputs high

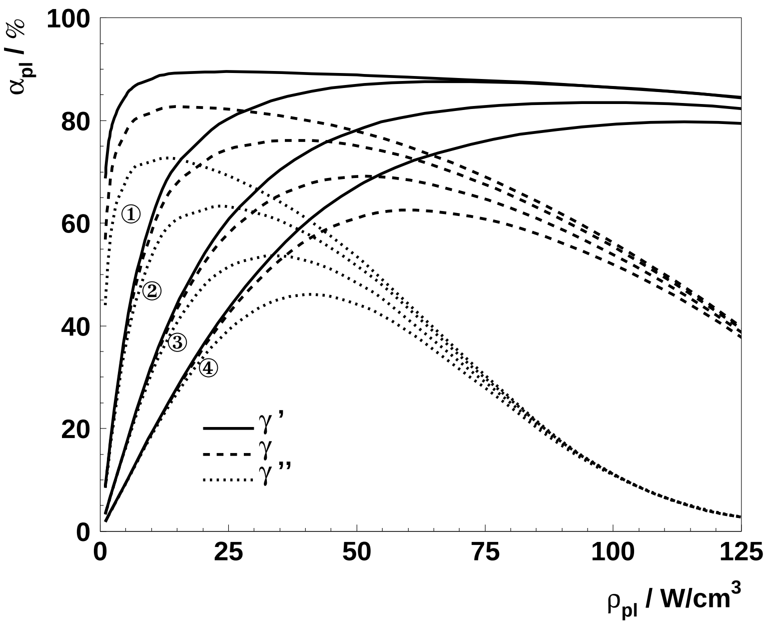

Fig. 3.11: Degree of dissociation α_{pl} as a function of power density ρ_{pl}. For each throughput value, denoted by the numbers in circles, α_{pl} is shown for γ, γ' and γ'', indicated by the dashed, solid and dotted line. ① , ② , ③ and ④ denote a molecular throughput of $Q_m = 0$, 1, 2.8 and 5 mbar l/s, respectively.

degrees of dissociation can only be obtained at high power densities and with a low surface recombination coefficient. Otherwise the anticipated rise in the dissociation rate with increasing power density is overcompensated by an increase in the surface recombination rate. As a result, α_{pl} is expected to drop for higher values of ρ_{pl}. This effect is very pronounced if the increase of γ with surface temperature is assumed stronger than in eq. (3.36).

3.7 Summary

The influence of macroscopic parameters on the properties of a hydrogen discharge have been calculated using a model based on microscopic processes, which involves electron kinetics, the balance of charged particles and atomic loss mechanisms.

For the typical gas conditions in a dissociator plasma source, the dependence of reaction rates, elastic and inelastic collision frequencies and power losses per electron on the mean electron energy and atomic fraction have been calculated. It is worth to mention, that the calculated reaction rate for dissociation shows a quantitative agreement with model calculations based on a self–consistent solution of the Boltzmann equation given in ref. [79].

The mean electron energy has been determined taking into account the mechanisms of charged particle losses. Consequently, the power loss per electron could be determined, together with the electron density and reaction rates for dissociation. It has been found, that the total potential dissociation rate increases slightly overproportional to the power density.

The atomic losses are expected to be dominated by surface recombination and gas flow induced losses. The contribution from volume recombination is only minor for the gas conditions under consideration. The dependence of the degree of dissociation as a function of power density in the discharge has been predicted quantitatively assuming different scenarios for the recombination coefficient of the discharge tube wall.

Anticipating a high atomic fraction in the discharge over a wide throughput range, the plasma source has to be designed in a way that

1.) the power density can be varied over a broad range of up to $\rho_{\mathrm{pl}} \approx 100\,\mathrm{W/cm^3}$.

2.) the discharge tube provides a low wall recombination coefficient.

The requirement of a high power density in the discharge implies an efficient power transfer from the field applicator to the plasma. This problem is investigated in detail in the next section.

4 The Plasma Source

4.1 The mechanism of surface wave coupling

A widely used technique for sustaining hf discharges is the resonant coupling of the electromagnetic field to the plasma by applying cavities or oscillating circuits. However, resonant coupling implies several shortcomings:

1. The discharge acts as conducting medium. This results, especially at the anticipated high electron densities, in a reflection of the electromagnetic waves at the plasma surface [80]. As a consequence, the impedance matching may become instable and the power density cannot be increased further.

2. The plasma impedance depends strongly on the electron density. However, n_e in general changes when the gas conditions and the applied hf power are varied. This may envolve significant problems with respect to impedance matching [81, 83, 82].

3. Resonantly sustained plasmas often show a non–reproducable behaviour and mode variations. In case of radio frequency discharges, a change in gas pressure and applied hf power can result in the change from a homogenious plasma to a so–called plasmoid mode [56]. For microwave frequencies, spontaneous changes towards a surface wave mode are reported [84].

These drawbacks can be overcome, if the plasma is sustained by a surface wave which propagates along the interface between plasma column and dielectric discharge tube. Surface wave discharges (SWD) are reported to be stable, reproducable and quiescent over a broad range of operating conditions [85]. Surface wave propagation as a means of transporting electromagnetic energy along a dielectric or a conducting wire covered with a dielectric of suitable permittivity is known from microwave physics (see e.g. [86]). It has been shown in ref. [87], that surface waves can also be propagated along the positive column of a DC discharge, provided that

$$\omega_{\mathrm{hf}} \leq \frac{\omega_{\mathrm{p}}}{\sqrt{1+\epsilon_{\mathrm{dt}}}}\,, \tag{4.1}$$

where $\omega_{\mathrm{hf}} = 2\,\pi\, f_{\mathrm{hf}}$ is the angular frequency of the applied hf field, ω_{p} the electron–plasma frequency and ϵ_{dt} the relative permittivity of the discharge tube.

A compact field applicator, the so–called surfatron, which uses surface wave propagation in order to sustain a discharge, had been first disclosed by Moisan and co–workers [88, 89]. Until now, a series of surface wave launchers have been developed for frequencies ranging from 1 MHz to 10 GHz, the properties of which are described and analyzed theoretically in various articles (see e.g., refs. [85, 90, 91, 92]).

In case of surfatron based field applicators, the surface wave is launched by means of an azimuthal coupling slit terminating a coaxial line through which the discharge tube is inserted. Surface wave launching from a surfatron is illustrated in fig. 4.1. The

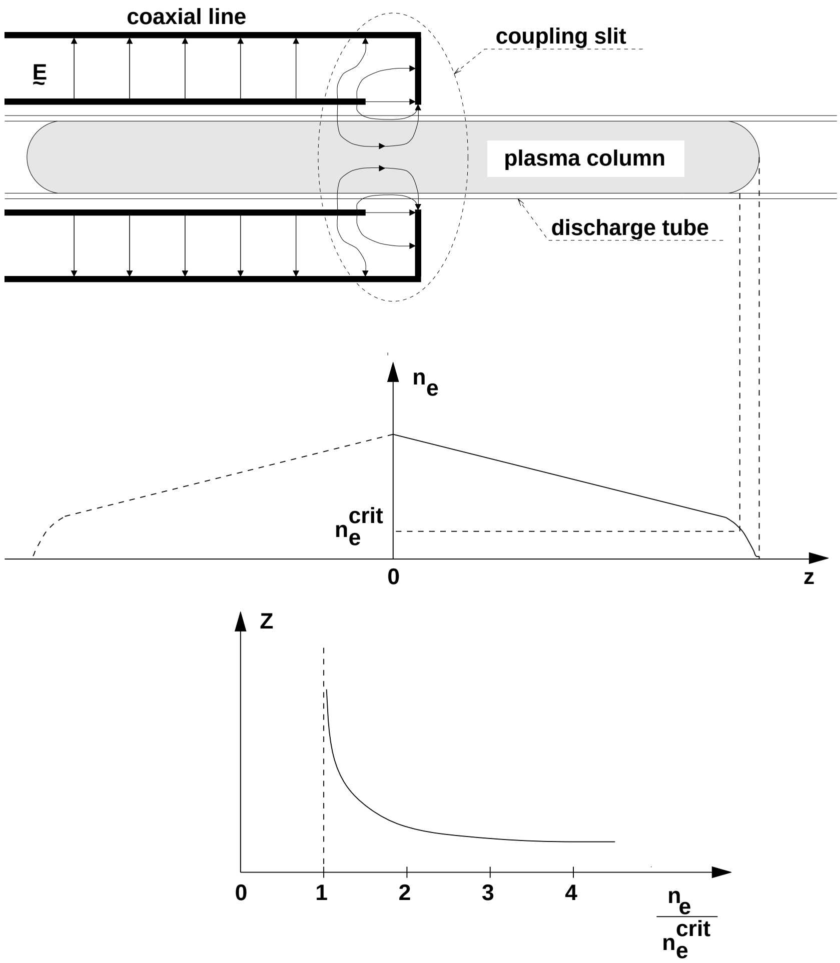

Fig. 4.1: Surface wave coupling to the discharge by means of a surfatron. The upper picture shows the electrical field distribution in the coaxial line and the region of the coupling slit. In the middle graph, the electron density n_e as a function of axial position z is shown. $n_\mathrm{e}^\mathrm{crit}$ is the critical electron density which defines the limit for surface wave propagation. The lower figure shows the impedance Z seen by the surface wave as a function of $n_\mathrm{e}/n_\mathrm{e}^\mathrm{crit}$.

usually transversal electromagnetic (TEM) mode in the coaxial line is transferred into a transversal magnetic (TM) surface wave mode at the coupling slit. Two surface waves are propagated in opposite direction along the discharge tube, so that the plasma created is symmetric with respect to $z = 0$. Usually, the geometry of both coaxial line and discharge tube are chosen such, that only the azimuthal symmetric mode is supported (the conditions for monomode operation will be discussed later in section (4.2.2)).

The surface wave is damped along the direction of propagation as it successively transfers power in order to maintain the discharge. As a result, the power density ρ_{pl} in the discharge decreases linearly with increasing axial distance $|z|$ from the coupling slit. Because of small variations in the total power loss per electron Θ_{tot}, this leads to a nearly linear decrease of the electron density n_{e} with z, which is a main characteristic of surfatron sustained SWDs [93]. Since the electron plasma frequency is given by (see e.g. ref. [28])

$$\omega_{\mathrm{p}} = \sqrt{\frac{n_{\mathrm{e}}\, e^2}{\epsilon_0\, m_{\mathrm{e}}}}\,, \tag{4.2}$$

where e is the elementary charge and ϵ_0 is the permittivity of free space, one obtains from eq. (4.1):

$$n_{\mathrm{e}} \geq \frac{4\,\pi^2\,\epsilon_0\,m_{\mathrm{e}}}{e^2}\,(1+\epsilon_{\mathrm{dt}})\,f_{\mathrm{hf}}^2 = n_{\mathrm{e}}^{\mathrm{crit}}. \tag{4.3}$$

This means, that surface wave propagation and hence the discharge column is terminated, if the electron density decreases below a critical value $n_{\mathrm{e}}^{\mathrm{crit}}$, which is solely determined by the applied field frequency and the dielectric properties of the discharge tube.

The anticipated quiescence and reproducability of the discharge behaviour require a stable impedance matching. In case of surface wave plasmas, the characteristic impedance Z seen by the surface wave is nearly constant for a wide range of the ratio $n_{\mathrm{e}}/n_{\mathrm{e}}^{\mathrm{crit}}$, as shown in fig. 4.1. Only if the electron density becomes close to $n_{\mathrm{e}}^{\mathrm{crit}}$, Z increases. This behaviour is a consequence of the low level of fluctuations in the electron density and it results in uncritical impedance matching properties over a wide range of operating conditions.

4.2 Plasma source design and operation

As established in section 3, the field applicator has to provide a high power density in the discharge to achieve a high dissociation rate. In case of a SWD, one therefore has to aim for a high frequency, since according to eqs. (3.12) and (4.3), the minimum electron density is proportional to f_{hf}^2 and the power density is proportional to n_{e} . Moreover, from the dependence of the degree of dissociation on the power density shown in fig. 3.11, one can conclude that high power levels are needed to obtain high atomic fractions. Taking into account these considerations, the designed field applicator is based on a standard microwave frequency of 2.45 GHz where power supplies (and the corresponding accessories) of the required power levels are available.

In the following, the set up of the microwave components is described in section 4.2.1, and the design and operational principle of the field applicator in section 4.2.2. In section 4.2.3, general results on the running performance are presented.

4.2.1 Microwave circuit

The arrangement of the microwave components for the plasma source is shown schematically in fig. 4.2. Microwaves are produced using an external magnetron (MUEGGE, MW–

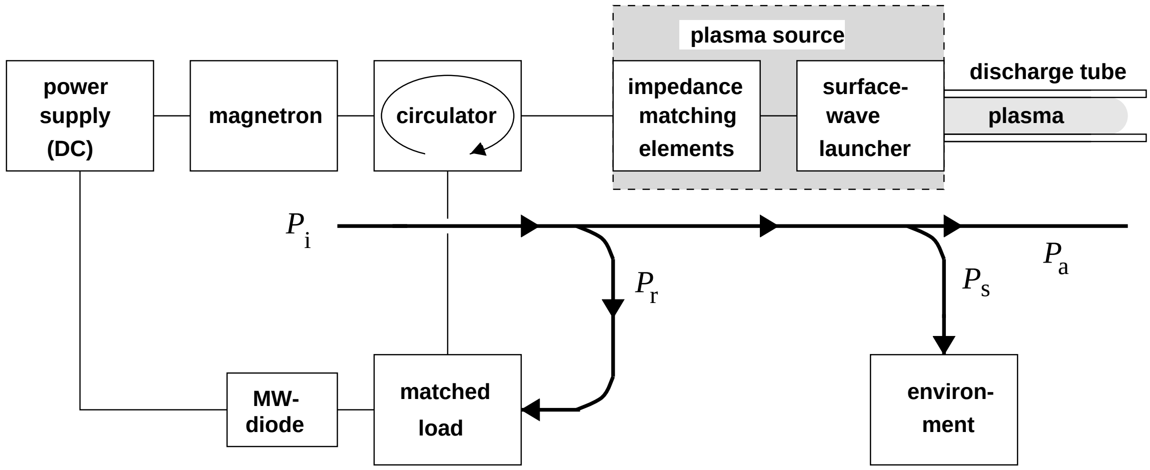

Fig. 4.2: Schematic overview of the general set up of the microwave components for the surface wave plasma source designed. P_{i} denotes the incident power provided by the magnetron, P_{r} the power reflected by the plasma source, P_{s} the stray radiation emitted by the field applicator and P_{a} the power absorbed by the discharge.

46029–1200W), which is powered by a DC power supply (MUEGGE, MW–GIRYJ1540-1K2-08). The maximum incident microwave power is $P_{\mathrm{i}}^{\mathrm{max}} = 1200\,\mathrm{W}$. A circulator (PHILIPPS, type 2722 163 02101) serves to protect the magnetron from the power P_{r} reflected by the plasma source caused by an impedance mismatch. P_{r}, the value of which is indicated at the power supply, is directed into a matched, water cooled load. The plasma source consists of the surface wave launcher, the impedance matching elements and the discharge tube. The impedance matching elements serve to tune the total impedance of surface wave launcher and discharge in order to match the magnetron impedance. The surface wave launcher transfers the microwave power into a surface wave mode sustaining the discharge, where the power P_{s} lost by stray radiation should be preferably low. The discharge tube together with the plasma column acts as guiding structure for the surface wave, provided its relative permittivity is sufficiently low in order to fulfill the propagation condition given in eq. (4.1).

The power transfer efficiency from the field applicator to the discharge is given by the ratio of the power absorbed by the plasma divided by the incident power:

$$\eta = \frac{P_\mathrm{a}}{P_\mathrm{i}} = \frac{P_\mathrm{i} - P_\mathrm{r} - P_\mathrm{s} - P_\mathrm{c}}{P_\mathrm{i}}, \tag{4.4}$$

where P_c are the ohmic losses in the different components and connections due to the skin effect.

4.2.2 The modified waveguide surfatron

The field applicator has been designed such, that the microwaves coming from the magnetron are fed into the coaxial line forming the surfatron via a standard rectangular wave guide in order to provide a maximum power transfer efficiency also at high power levels. This principle is similar to that of a so–called waveguide surfatron field applicator [94]. Because of some important modifications compared to the original design [95], the field applicator designed is referred to as modified waveguide surfatron (MWS). The MWS is schematically shown in fig. 4.3. All components of the MWS are made of brass, copper and

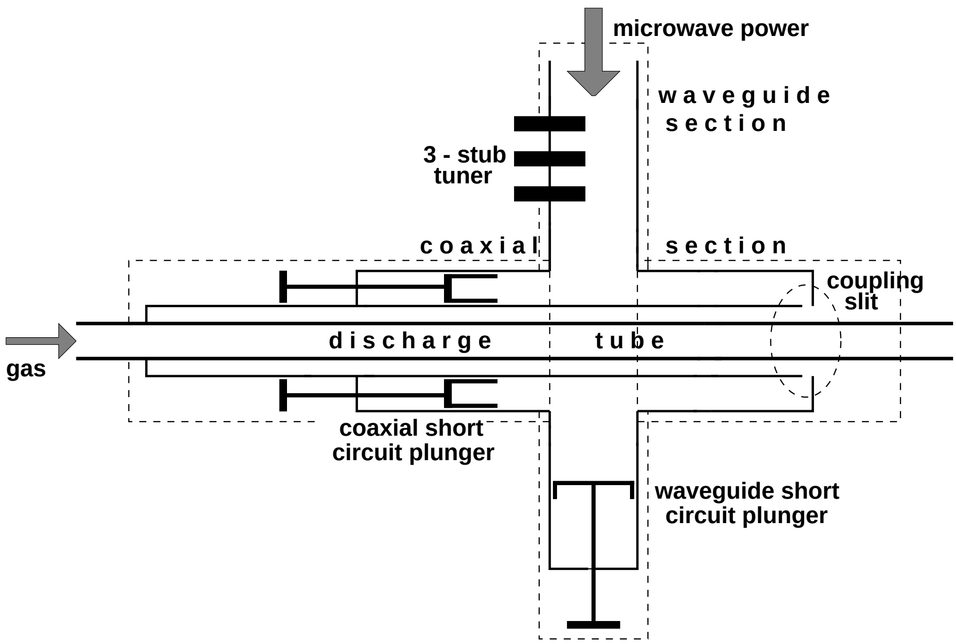

Fig. 4.3: Schematic representation of the modified waveguide surfatron field applicator. The various components are explained in the text.

CuBe with a high electrical conductivity each. The waveguide section is based on a standard R 26 waveguide with an inner width and height of 43 mm and 86 mm, respectively. It is terminated by a rectangular short circuit plunger (MUEGGE, MW–6971–0071). Mode shaping can be optmized by a three–stub–tuner (MUEGGE, MW–7614–0060). For $f_{\rm hf} = 2.45\,\rm GHz$, only the $\rm TE_{01}$ mode is supported. The incident microwave power from the magnetron is fed into the waveguide section by means of a low–loss coaxial cable with a damping ratio of 0.5 dB and two coaxial–to–waveguide transitions (MUEGGE, MW–6971–0040). In the center of the waveguide section, the coaxial section is inserted perpendicular to the broad width of the waveguide. Here, the $\rm TE_{01}$ mode is transferred into a coaxial mode. The coaxial section is terminated by a short circuit plunger placed in its rear part. The lenght of the rear coaxial line measured from the rectangular waveguide is 135 mm, so that the plunger position can be varied by more than one wavelenght. The front end of the coaxial section is terminated by the coupling slit, where a mode transfer occurs from the coaxial into the surface wave mode. The variability of the coupling slit width serves as additional impedance matching element.

In order to achieve a homogenious radial distribution of the electron density in the discharge as well as a reproducible impedance matching, one has to aim for exclusive propagation of the azimuthal symmetric surface wave mode [97]. With respect to the MWS, this involves the following requirements [98]:

(i) The wave mode in the coaxial line has to have azimuthal symmetry.
This is obtained launching exclusively the coaxial TEM mode, which requires [96]

$$a + b \leq \frac{c}{\pi\, f_{\rm hf}} \approx 39\,\rm mm \quad for \ \ f_{\rm hf} = 2.45\,\rm GHz\,, \tag{4.5}$$

where a and b are the inner radius of the outer coaxial conductor and the outer radius of the inner coaxial conductor, respectively, and c is the speed of light.

(ii) The inner discharge tube diameter has to satisfy the condition

$$r_{\rm dt} \leq \frac{2\,\rm GHz\,cm}{f_{\rm hf}} \approx 8\,\rm mm \quad for \ \ f_{\rm hf} = 2.45\,\rm GHz\,. \tag{4.6}$$

In order to accomodate discharge tubes with an inner radius of up to the value allowed in eq. (4.6) and at the same time to fulfill eq. (4.5), the dimensions of the coaxial section have been chosen to $a = 25$ mm, whilst b has been varied between 10.5 mm and 14 mm, depending on the outer diameter of the discharge tube used. This results in a gap width between the outer diameter of the discharge tube and the inner diameter of the inner conductor, which provides sufficient cooling of the discharge tube (the discharge tube cooling is discussed below). No restrictions arise with respect to the length of the coaxial section. Since it acts like a coaxial line with a large surface area of high electrical conductivity, ohmic losses and hence damping of the TEM mode are negligible.

Power losses due to stray radiation, which occur when the TEM mode is transferred to the surface wave mode, can be minimized keeping the end plate of the coupling slit sufficiently thin [88]. Thin plates, however, may become deformed resulting in locally excessive electrical field strenghts. Higher power levels can even lead to a destruction of the end plate [82]. Regarding the electrical field configuration in the region of the coupling slit as shown in fig. 4.1, only the inner surface of the end plate and its tip are of importance. As illustrated in fig. 4.4, the end plate of the MWS therefore consists of

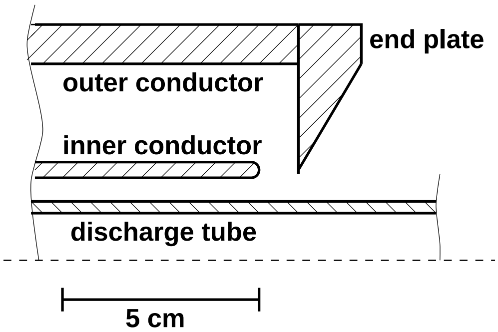

Fig. 4.4: Scale drawing of the coupling region of the MWS. The design of the end plate and the tip of the inner conductor assure high power handling capability and a azimuthal homogeneity of the the electrical field distribution.

an 8 mm thick copper plate tapered down to a knife edge towards the coupling region. This assures mechanical stability and sufficient heat conductivity. Additionally, the tip of the inner conductor has been rounded to provide a more homogenious electrical field distribution.

Special care has been taken in the design of the coaxial short circuit plunger, which is the most important impedance matching element of the MWS. Since it has to withstand high blind currents, the contact to the coaxial line has to have desirably low ohmic losses, and the plunger must be easily adjustable for impedance matching. Therefore, the coaxial short has been designed as a $\lambda/4$ short circuit [96], machined out of a single piece of CuBe. As shown in fig. 4.5, the voltage maximum occurs at the tip of the plunger, whereas the maximum current arises at the bottom, where the surface area and hence the conductivity is largest.

Finally, the requirements towards the discharge tube as a main part of the plasma source shall be discussed. Since the discharge tube serves as guiding structure for the surface wave, beside the mechanical and chemical also the dielectric properties have to be considered.
Required are:

(i) Mechanical stability up to high gas temperatures and towards large radial temperature gradients.
As shall be shown in section 5.3, the outer surface of the downstream tube end is cooled to temperatures as low as 40 K, whilst the gas temperatures inside the tube are expected to be as high as 2000 K.

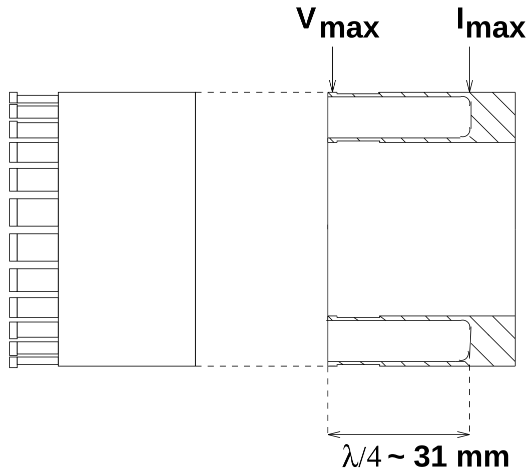

Fig. 4.5: Side view of the $\lambda/4$ coaxial short circuit. In the cross section given in the right figure, the voltage and current maxima V_{max} and I_{max} are indicated.

(ii) High chemical resistance.
Although, in contrast to resonantly coupled rf discharges, no high sheath potentials at the tube surface and thus no sputtering due to bombardment with energetic ions are expected in case of SWDs, there will be a substantial rate of so–called chemical sputtering. Chemical sputtering results from wall recombination, where energies up to the recombination energy of 4.5 eV are deposited on the surface. These energies are sufficient to break up chemical bonds of the tube material. Consequently, the rate of chemical sputtering is directly proportional to the surface recombination coefficient.

(iii) Low dielectric losses.
A low value of the relative permittivity at 2.45 GHz is required in order to maximize the power transfer efficiency to the discharge as well as to enable surface wave propagation (see eq. (4.1)).

Besides borosilicate and quartz glass, possible materials are Al_2O_3 based ceramics. A detailed information on the properties of the tubes used is given in Appendix D.

Concerning glass as discharge tube material, it has been already mentioned, that the recombination coefficient increases strongly with increasing surface temperature (see section 3.5.1). Therefore, the inner diameter of the inner coaxial conductor has been chosen such, that there is a sufficient gap to the outer tube surface in order to provide an adequate flow of the coolant. Additionally, the coolant has to have a low permittivity in order to allow surface wave propagation. This condition restricts the choice of cooling media to cold or liquified gas such as cold He or LN_2 and to some types of silicon or mineral oils (see e. g. [99]). For the plasma source presented, forced–air cooling has been used. As shall be shown later in section 5, fig. 5.1, the air is guided between the discharge tube and the inner coaxial conductor or another coaxial glass tube downstream the coupling slit. Forced air cooling is the least complicated method and rules out the risk of contaminating of the vacuum system in case of a crack in the discharge tube.

4.2.3 Plasma source operation

For the operation of the MWS plasma source, at first the impedance matching was optimized, using a set–up similar to fig. 4.6. It is important to mention, that for all gases used (air, helium, hydrogen), the discharge could be ignited by matching the impedance only with the three–stub–tuner, having the coaxial and waveguide short citcuit plungers set such, that the reflected power P_r was at minimum. However, the more convenient way was to use a 9 kV high voltage pulse (HUETTINGER, Laserzündhilfe LZH–1) applied to a pin at the outer discharge tube surface. Doing so, the impedance matching elements could be left unchanged with respect to the steady–state discharge. It has been found, that a perfect impedance matching with $P_r = 0$ can be achieved by exclusively varying the position of the coaxial short, provided the width of the coupling slit was set to a value between 3 and 10 mm. In order to keep P_r at the minimum, no change in the position of the coaxial short is nescessary for incident microwave power levels ranging between about twice the extinction power and 1200 W. This confirms the evolution of the impedance seen by the surface wave as described in fig. 4.1. Also a change in the gas parameters (pressure, gas mixture) leads only to minor changes in the reflected power. The plasma source can be operated in a pressure range between 10^{-3} mbar and 1500 mbar. Increasing the pressure from 1 mbar up to 1000 mbar results at first in an axial shrinkage of the plasma column, and for pressures beyond ≈ 100 mbar in an additional radial contraction, ending up in a filamentary discharge as described in ref. [100]. In summary, the reflected power can be tuned to zero for the entire pressure and power range, provided that the incident microwave power is higher than about twice the extinction power. The pressure requiring the lowest incident microwave power for discharge ignition ranges between 1 and 7 mbar. For hydrogen, an optimum value of about 4 mbar has been found in agreement with the studies presented in ref. [101].

The ohmic losses in the different components of the MWS have been found to be negligible. No heating has been observed, apart from the effect of heat radiated from the discharge inside the inner coaxial conductor. After disassembling the MWS, no traces of local heating at the gap flange or the coaxial short could be found. Also the commercial coaxial–to–waveguide transitions revealed no ohmic losses. Therefore one can assume, that the ohmic losses are restricted to the piece of coaxial cable separating the circulator from the MWS, which gets slightly warm when operating at microwave powers exceeding 400 W.

The power P_s lost due to stray radiation has been determined using a calibrated stray field detector (HOLADAY INDUSTRIES, HI 1501). Herefore, the stray radiation per unit surface area $(\mathrm{d}P_s/\mathrm{d}A)$ has been measured at radial distances r of 5 cm and 10 cm from the center of the coupling region for various azimuthal and polar positions. A nearly isotropic distribution has been found. The total stray radiation power loss P_s is obtained by integrating the measured values, resulting in:

$$P_\mathrm{s} \approx 4\,\pi\,r^2\,\frac{\mathrm{d}P_\mathrm{s}}{\mathrm{d}A}\,.$$

P_s has been found to be about 3 % of the incident microwave power, whatever the value of P_i.

In summary, the designed MWS based plasma source reveals uncritical impedance matching properties and low losses due to stray radiation and skin effect. Considering eq. (4.4), one can conclude a high power transfer efficiency of

$$\eta = 1 - \frac{1}{P_\mathrm{i}}\,(P_\mathrm{r} + P_\mathrm{c} + P_\mathrm{s}) \approx 1 - (0 + 0.05 + 0.03) = 0.92\,,$$

i.e. about 92 % of the incident microwave power are absorbed by the discharge.

4.3 Test bench studies

In the following it is shown, that a qualitative optimization of the MWS sustained hydrogen discharge with respect to a maximum degree of dissociation can be achieved by the use of a simple test bench and visual inspection of the discharge. In section 4.3.1, the dependence of the plasma length on the atomic fraction is predicted, based on the theoretical considerations from section 3 and the properties of surfatron sustained SWDs described previously. The experimental set–up and the results are shown in section 4.3.2.

4.3.1 Theoretical considerations

Surfatron sustained SWDs are characterized by a linear decrease of the power density in the discharge along the direction of propagation. Therefore one can write:

$$\rho_\mathrm{pl}(z) = \rho_\mathrm{pl}^0 - \frac{\mathrm{d}\rho_\mathrm{pl}(z)}{\mathrm{d}z}\,z\; = \rho_\mathrm{pl}^0 - \frac{\rho_\mathrm{pl}^0 - \rho_\mathrm{pl}^\mathrm{crit}}{L}\,z\,. \tag{4.7}$$

where $\rho_\mathrm{pl}^0 = \rho_\mathrm{pl}(0)$ and $\rho_\mathrm{pl}^\mathrm{crit} = \rho_\mathrm{pl}(L)$ are the power densities at the coupling slit and at the end of the plasma coulumn, respectively, and L is the length of the plasma column measured from the coupling slit. It is important to note, that the actual plasma length is $2\,L$, since two surface waves are launched in opposite direction at $z = 0$.

Assuming power balance in the discharge, i.e., all microwave power absorbed is transferred to the electrons dissipating it via elastic and inelastic collisions to the neutrals, one obtains for the power absorbed by the discharge:

$$P_\mathrm{a} = V_\mathrm{pl}\,\left(\frac{1}{L}\int_0^L \rho_\mathrm{pl}(z)\,\mathrm{d}z\right) = \frac{1}{2}\,\pi\,r_\mathrm{dt}^2\,L\,\left(\rho_\mathrm{pl}^0 + \rho_\mathrm{pl}^\mathrm{crit}\right) \tag{4.8}$$

In case of a SWD, eq. (3.12) becomes:

$$\rho_{\mathrm{pl}}(z) = n_{\mathrm{e}}(z)\,\Theta_{\mathrm{tot}}(z)\,. \tag{4.9}$$

From the results of the discharge model shown in fig. 3.8 one can conclude, that the electron density n_{e} varies much stronger with the power density than the total power loss per electron Θ_{tot}, provided the degree of dissociation does not change much with axial position. Rearranging eq. (4.8) then yields:

$$\Theta_{\mathrm{tot}}\,\frac{\mathrm{d}n_{\mathrm{e}}(z)}{\mathrm{d}z} = \frac{2}{L}\left(\frac{P_{\mathrm{a}}}{\pi\, r_{\mathrm{dt}}^2\, L} - \rho_{\mathrm{pl}}^{\mathrm{crit}}\right) = \frac{2}{L}\left(\bar{\rho}_{\mathrm{pl}} - \rho_{\mathrm{pl}}^{\mathrm{crit}}\right)\,, \tag{4.10}$$

where $\bar{\rho}_{\mathrm{pl}}$ is the axially averaged power density in the discharge.
Studies on plasma parameters of a 2.45 GHz sustained hydrogen SWD presented in ref. [69] showed, that the slope $\mathrm{d}n_{\mathrm{e}}(z)/\mathrm{d}z$ normalized to the initial neutral density does not change with the degree of dissociation in the discharge. Consequently, taking into account eqs. (4.7), (4.9) and (4.10), one can conclude, that the linear decrease in power density and hence the damping rate will be proportional to the power lost per electron. Therefore, the length of the plasma column will be inversely proportional to the total power loss Θ_{tot} per electron for a constant power P_{a} absorbed by the discharge.

It has been shown in section 3, that for the mean electron energies obtained under typical gas conditions of a dissociator, $\Theta_{\mathrm{tot}} = \Theta_{\mathrm{tot}}(\alpha_{\mathrm{pl}})$ increases strongly for a decreasing atomic fraction as can be seen in fig. 3.6. Consequently, for a given value of P_{a}, the plasma column will be longer in case of a high atomic fraction than for a low one. From eq. (4.10) one expects that this behaviour is more pronounced in case of a larger difference between mean and critical power density, and hence for a larger difference between incident microwave power and extinction power.

In order to verify these predictions, the discharge has been investigated with a simple test bench set–up described in the following.

4.3.2 Experimental set up and results

The test bench has been set–up to investigate the following questions:

(i) Optimization of the plasma source parameters in order to achieve a high degree of dissociation based on the previous theoretical considerations.

(ii) Quantitative determination of the atomic losses in the afterglow of the discharge.

A schematic representation of the test bench is shown in fig. 4.6. The MWS is mounted on a linear motion bearing so that it can be slided over the discharge tube. The discharge tube used is 1100 mm long with an inner and outer diameter of 11 mm and of 14 mm,

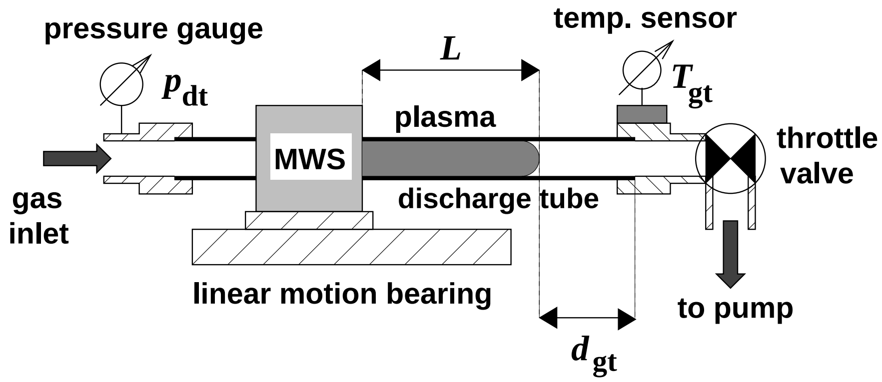

Fig. 4.6: Schematic representation of the set–up for the test bench studies.

---

respectively. It is air cooled using a rotary pump (see section 5.2). Gas is fed into the plasma source via the gas inlet system described later in section 6.2. The pressure in the discharge tube $p_{\rm dt}$ is measured using a capacitive gauge (LEYBOLD, CM 10). At the downstream end of the plasma source, the discharge tube is connected to the vacuum system via a glass–to–metal transition and a throttle valve. For the test bench set–up a rotary pump (PFEIFFER, DUO 030) with an oil trap has been used. The throttle valve allows an adjustment of the discharge tube pressure in a range of about $p_{\rm dt} = 0.5 \ldots 10\,\mathrm{mbar}$ independent of the throughput for $Q_{\rm m} \leq 2.5\,\mathrm{mbar\,l/s}$. The glass–to–metal transition made of stainless steel serves also as recombination body for the hydrogen atoms produced in the discharge. The temperature increase $\Delta T_{\rm gt}$ at the glass–to–metal transition arising from recombination heating is measured with a Pt–100 sensor. The visible plasma length L is measured from the coupling slit to the end of the discharge. As mentioned previously, the actual plasma length is assumed to be equal to $2\,L$.
In case all atoms recombine on the stainless steel surface, the heating power due to recombination is

$$P_{\rm rec} = Q_{\rm m}\, 2\, \alpha_{\rm gt}\, E_{\rm rec}\,, \tag{4.11}$$

where $\alpha_{\rm gt}$ is the degree of dissociation in the gas in front of the glass–to–metal transition and $E_{\rm rec}$ is the recombination energy equal to $4.48\,\mathrm{eV}$, the binding energy of a hydrogen molecule [63]. In first order, the temperature rise measured should be proportional to $P_{\rm rec}$.

In order to verify the predicted dependence between plasma length and atomic fraction, L and $\Delta T_{\rm gt}$ have been measured varying gas pressure and throughput, incident microwave power and cooling air flow. Moreover, various discharge tube materials and surface treatments have been tested. The measurements done with zero gas flow in a pressure range of several millibars showed that the ceramic tubes cannot be used as they revealed severe drawbacks in their mechanical and dielectric properties. Although Al_2O_3 based tubes have been found to exhibit a high chemical resistance [102], they are not suitable for the present application, since they tend to develop cracks at higher power levels. In case of the SiC tube, no surface wave could be propagated due to excessive dielectric losses.

Using glass tubes, it could be observed, that long pink–red coloured plasma columns could be obtained for both quartz and borosilicate tubes, L being slightly longer in case of borosilicate glass. The pink–red colour arises from excitation of the atomic Balmer–lines (especially the H_α–line), indicating an appreciable atomic fraction in the discharge. Switching off the air cooling, the discharge contracted axially and became white. A similar observation is described in ref. [69]. The white colour arises from the excitation of molecular vibrational and rotational bands, which yield a quasi–continuous emission spectrum, and is therefore an indication for a high molecular fraction in the discharge. This observation supports the prediction, that a high degree of dissociation coincides with a maximum plasma length.

Running the discharge with a gas flow of 1 mbar l/s and with the maximum cooling air flow available yielded a similar effect. For the first few seconds after igniting the discharge, the plasma column was long and pink–red and then gradually contracted turning into a white colour. This observation can be explained as follows: at the beginning, the discharge tube wall is still cold and one obtains a high initial atomic fraction. Then, the tube surface will be gradually heated by the hot gas, ionic bombardment and surface recombination. Consequently, the recombination coefficient of the glass tube rises and hence the atomic loss rate, and the degree of dissociation $\alpha_{\rm pl}$ decreases. A lower value of $\alpha_{\rm pl}$ however, results in a higher power loss per electron and hence a higher power density $\rho_{\rm pl}$ in the discharge. Although a higher power density yields a higher dissociation rate $K_{\rm R2}$ as shown in fig. 3.8, it will also increase the tube surface temperature and hence the surface recombination rate. As a consequence, $\alpha_{\rm pl}$ decreases further, which finally results in a situation where the atomic loss rate is substantially higher than the dissociation rate. In case of this scenario, only a negligible temperature rise $\Delta T_{\rm gt}$ of less than 3 K has been measured indicating that nearly no atoms reach the glass–to–metal transition.

The observation of a decreasing degree of dissociation for an increasing power density is simulated by the model calculations shown in fig. 3.11: regarding the dashed lines which denote a strong increase of γ with increased power density, $\alpha_{\rm pl}$ first rises when $\rho_{\rm pl}$ is increased and, after passing a maximum, drops for a further increase in $\rho_{\rm pl}$. The difference compared to the situation with zero gas flow is a lower initial degree of dissociation due to gas flow induced atomic losses, which leads to a higher initial power density.

However, long and pink–red plasma columns coinciding with high values of $\Delta T_{\rm gt}$ can be obtained by admixing a small amount of oxygen to the hydrogen gas. Measurements have shown, that the recombination coefficient of glass poisoned by water vapour is up to two orders of magnitude smaller compared to the bare glass surface [103], which could be

theoretically explained by a change in activation energy with respect to the adsorption of hydrogen atoms on the surface. Another theory suggests a mechanism of catalytic dissociation of H_2 by OH–radicals formed in the discharge [104]. For the optimization of an ABS dissociator plasma it has been shown in ref. [41], that high atomic fractions can also be achieved admixing oxygen containing molecules, so that that admixing O_2 is the most convenient and reproducible method in order to benefit from the "water effect".
However, the water produced in the dissociator plasma source as a result of the oxygen admixture (see sections 7.3 and 7.4) is found to contradict the anticipated long–term stability of the ABS. As mentioned previously, the ice layer frozen onto the cold nozzle leads to a decrease in the output intensity, a behaviour also observed at the Madison–ABS [105]. Consequently, for the MWS based discharge attempts have been made to minimize the O_2 admixture needed to obtain a maximum degree of dissociation. This goal has been achieved in two steps, which both helped to minimize the wall recombination coefficient:

(i) Efficient tube cooling.
The cooling air flow has been maximized using a rotary pump with a nominal pumping speed of $140\,\mathrm{m^3/h}$ (see also section 5.2). In order to obtain the maximum air flow, the inner diameter of the coaxial inner conductor has been chosen such as to provide a gap of 3.5 mm to the outer diameter of the glass tube. It has been verified, that no change occured in the power transfer efficiency with respect to the initial MWS set–up with an inner conductor providing a gap of only 1 mm. However, at a given oxygen admixture the plasma length has been significantly longer with the large gap width owing to a decreased tube wall temperature.

(ii) Suitable surface preparation.
Various chemicals and procedures have been tested, which are described in Appendix D. The best and most reproducible results have been obtained rinsing the tubes with an acid mixture of highly concentrated chlorine and hydrofluoridic acid followed by a bake–out under vacuum.

The results obtained under these conditions are shown in fig. 4.7 for a hydrogen gas throughput of $Q_{\mathrm{m}} = 1.0\,\mathrm{mbar\,l/s}$. In order to suppress the effect of atomic losses in the plasma afterglow, the position of the MWS for a given set of parameters has been set such, that the distance between the end of the plasma column and the glass–to–metall transition was kept constant at 5 cm. As shown in the left graph, the plasma length L for a given incident microwave power P_{i} increases with increasing oxygen admiture $Q^{\mathrm{rel}}_{\mathrm{O_2}}$ and saturates for $Q^{\mathrm{rel}}_{\mathrm{O2}} \geq 0.15\,\mathrm{flux\%}$. The right graph shows, that the maximum in L coincides with a maximum in the recombination induced temperature rise ΔT_{gt}. One also can conclude, that for $P_{\mathrm{i}} = 240\,\mathrm{W}$, which is close to the extinction power of 180 W, the change in L is not very sensitive to a change in the degree of dissociation. This observation can be explained by eq. (4.10), which predicts a small change in L during a variation of α_{pl} in case the incident microwave power does not exceed much the extinction power.

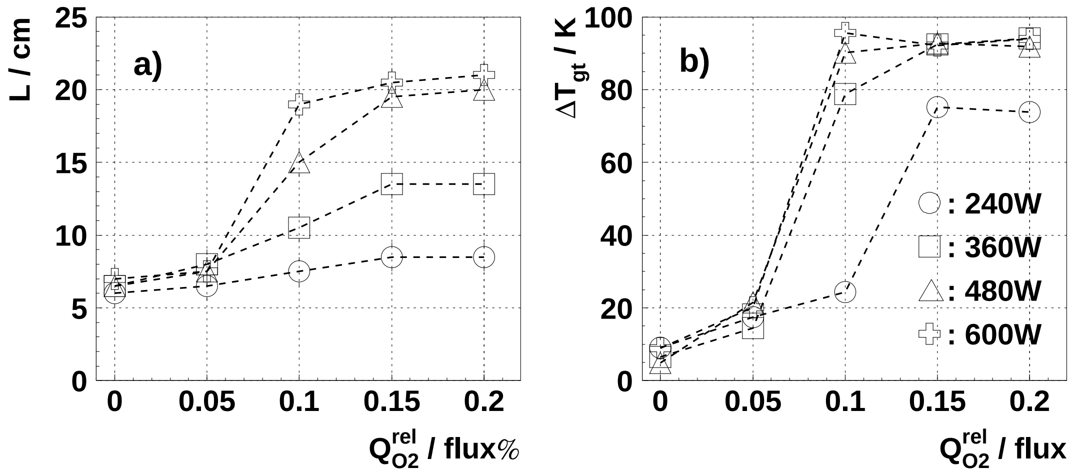

Fig. 4.7: a) Plasma length L measured from the coupling slit as a function of relative oxygen admixture $Q_{O_2}^{rel}$. b) Temperature rise ΔT_{gt} at the glass–to–metal transition as a function of $Q_{O_2}^{rel}$. The data have been taken for four different microwave power levels ranging from 240 W to 600 W.

Moreover one can conclude, that the mean power density for this low P_l value is not sufficient to reach a maximum atomic fraction as the gas flow induced atom losses cannot be compensated, which is in qualitative agreement with the result shown in fig. 3.11.

A rather different behaviour has been observed if the discharge has been operated with deuterium instead of hydrogen. Only about half the oxygen admixture was needed to establish the same recombination heating ΔT_{gt}. Moreover, the plasma column at a given value of ΔT_{gt} was always up to 20 % longer. This observation can be explained looking at the kinetics in the discharge described in section 3. It has been shown, that the amount of power lost by elastic electron–neutral collisions is significant. This leads to a heating of the neutral gas and hence the discharge tube, resulting in an increased surface recombination rate according to eqs. (3.35) and (3.36). It is obvious from eq. (3.21), that the elastic power losses are by a factor of 2 lower for deuterium compared to hydrogen since the deuterium neutrals have twice the mass of the hydrogen neutrals. Therefore, the neutral gas in the deuterium discharge is less hot and additionally the total power loss Θ_{tot} per electron is reduced. This results in a lower power density and a reduced heating of the discharge tube surface. From the results given in figs. 3.5 and 3.6 taking into account a mean electron energy of about 4 eV, one expects Θ_{tot} in a highly dissociated deuterium discharge to be about 25 % lower compared to the case of hydrogen. This is in good agreement with the experimental observation of a 1.2 times longer plasma column at the same value of ΔT_{gt}.

With respect to the dissociator design, a knowledge of the recombination losses in the afterglow is decisive. This information has been obtained measuring ΔT_{gt} as a function of the distance d_{gt} between the end of the plasma column and the glass–to–metal transition. The measurements have been performed for a throughput of $Q_{\mathrm{m}} = 1.0\,\mathrm{mbar\,l/s}$, where P_{i} and $Q^{\mathrm{rel}}_{\mathrm{O}_2}$ have been set to 480 W and 0.15 flux% in order to yield the maximum atomic fraction in the discharge according to the previous results. At the given throughput, the initial pressure p_{dt} in the discharge tube before plasma ignition has been varied between 0.6, 1.2 and 2.4 mbar. The results are shown in fig. 4.8. The error bars denote

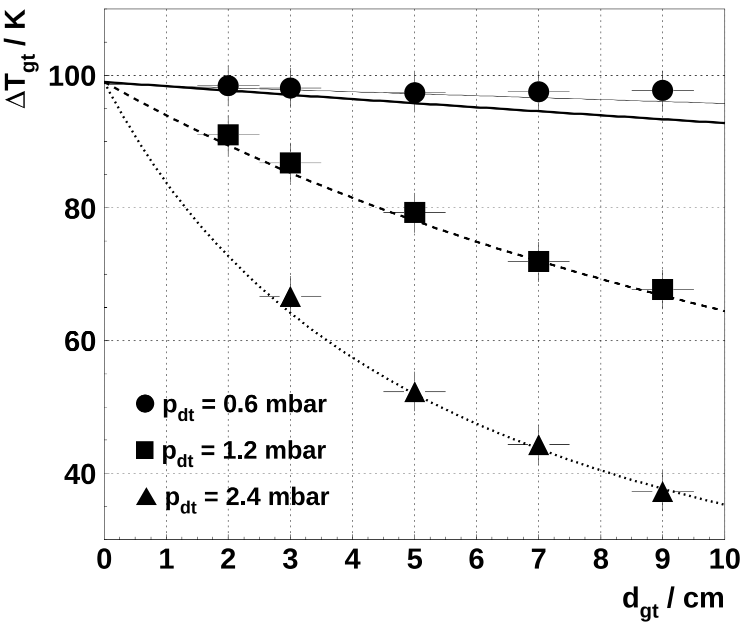

Fig. 4.8: Temperature rise ΔT_{gt} at the glass–to–metal transition as a function of the distance d_{gt} between plasma end and glass–to–metal transition for three different discharge tube pressures p_{dt}. The thin solid line denotes a fit to the data taken at $p_{\mathrm{dt}} = 0.6\,\mathrm{mbar}$, and the thick solid, dashed and dotted lines curves represent model calculations.

the systematic uncertainties in the determination of L ($\pm 0.5\,\mathrm{cm}$) and of ΔT_{gt} ($\pm 3\,\mathrm{K}$). Fitting the curve taken at $p_{\mathrm{dt}} = 0.6\,\mathrm{mbar}$, one can conclude that the atomic density is not high enough to induce atomic losses due to volume recombination, and that there are only minor surface recombination losses on the discharge tube wall.
This allows to estimate the wall recombination coefficient γ of the discharge tube under study. Taking into account the maximum systematic errors of the measurement, one can conclude that along an axial distance of 7 cm at most 6 % of the atoms are lost. Consequently, one obtains for the number of wall recombinations per atom

$$N_{\text{ar-w}} = \nu_{\text{ar-w}}\, t_{\mathrm{dwell}} \le 0.06\,, \text{ where } t_{\mathrm{dwell}} = \frac{7\,\mathrm{cm}}{v_{\mathrm{gas}}} \tag{4.12}$$

is the dwell time of a hydrogen atom in the afterglow and v_{gas} is the throughput induced axial gas velocity from eq. (3.40). From eq. (3.35), γ can be estimated, assuming a gas temperature in the afterglow of $T_\mathrm{n} = 300\,\mathrm{K}$ as

$$\gamma \le 0.06\,\frac{(2.405)^2}{12}\sqrt{\frac{m_\mathrm{a}}{k\,T_\mathrm{n}}}\,\frac{r_\mathrm{m}^2\,Q'_\mathrm{m}}{0.07\,\mathrm{m}} = 5.2\times 10^{-4}\,, \tag{4.13}$$

which is in good agreement with the value shown in fig. 3.9 for 300 K taken from ref. [76]. Since the data from this reference represent the lowest values found in the literature, one can conclude that the treatment of the glass tube actually yields very low wall recombination losses.

Taking into account the low amount of surface recombination losses, the decrease of ΔT_gt with increasing d_gt for the higher initial discharge tube pressures can be explained solely by volume recombination losses. Equation (3.37) yields a differential equation for atomic density dependence on the distance d_gt from the plasma end:

$$\nu_\mathrm{ar\text{-}v} \equiv -\frac{1}{n_\mathrm{a}^0}\,\frac{\mathrm{d}n_\mathrm{a}(t)}{\mathrm{d}t} = -\frac{v_\mathrm{gas}}{n_\mathrm{a}^0}\,\frac{\mathrm{d}n_\mathrm{a}(d_\mathrm{gt})}{\mathrm{d}d_\mathrm{gt}} = k_\mathrm{ar\text{-}v}\,n_\mathrm{a}^2\,, \tag{4.14}$$

the solution of which is given by

$$n_\mathrm{a}(d_\mathrm{gt}) = n_\mathrm{a}^0\left(1 + d_\mathrm{gt}\,(n_\mathrm{a}^0)^2\,\frac{k_\mathrm{ar\text{-}v}}{v_\mathrm{gas}}\right)^{-1}\,, \tag{4.15}$$

where $n_\mathrm{a}^0 = n_\mathrm{a}(d_\mathrm{gt} = 0)$ is the atom density at the downstream plasma end.
Since the temperature rise at the glass–to–metal transition is assumed to be proportional to the atomic flow rate, the dependence of ΔT_gt on d_gt is obtained from eqs. (3.40), (3.17) and (4.15) as

$$\Delta T_\mathrm{gt}(d_\mathrm{gt}) = \Delta T_\mathrm{gt}^0\left(1 + k_\mathrm{ar\text{-}v}\,d_\mathrm{gt}\,(2\,\alpha_\mathrm{pl}\,n_\mathrm{n}^0)^2\,\frac{n_\mathrm{n}^0\,r_\mathrm{dt}^2\,\pi}{Q'_\mathrm{m}}\right)^{-1}\,, \tag{4.16}$$

where $\Delta T_\mathrm{gt}^0 = \Delta T_\mathrm{gt}(d_\mathrm{gt} = 0)$ is the initial temperature rise at zero distance.
Fitting the data obtained for $p_\mathrm{dt} = 0.6\,\mathrm{mbar}$ yielded $\Delta T_\mathrm{gt}^0 = 99\,\mathrm{K}$. This has been inserted into eq. (4.16), and $\Delta T_\mathrm{gt}(d_\mathrm{gt})$ has been calculated for the three different pressures investigated. For an atomic fraction of $\alpha_\mathrm{pl} = 0.75$ at the downstream end of the discharge, the calculated curves are in good areement with the measured data, as shown in fig. 4.8. This indicates, that for all pressures investigated the degree of dissociation at the downstream end of the discharge is equal and high.

If d_gt is kept at zero and the incident microwave power is increased further, up to 1.2 times higher values of ΔT_gt have been obtained. For short distances d_cg between the coupling slit and the glass–to–metal transition and high incident microwave powers, typically $d_\mathrm{cg} = 10\,\mathrm{cm}$ and $P_\mathrm{i} \ge 600\,\mathrm{W}$, even standing wave patterns could be observed. This is a result of a reflection of the travelling surface wave (tw) at the end of the dielectric glass

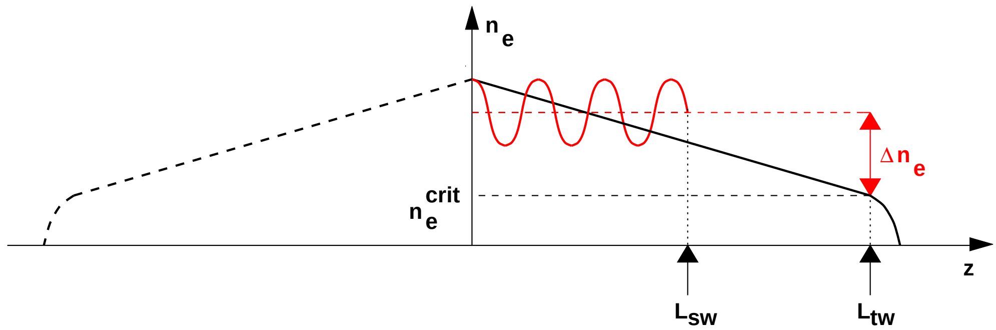

Fig. 4.9: Axial dependence of the electron density n_e in case of a travelling (tw) and a standing wave (sw) discharge shown by the black and the grey curve, respectively. L_{sw} and L_{tw} denote the end of the sw and the tw discharge and Δn_e is the difference between the electron density at the end of both discharges.

---

tube terminating surface wave propagation. A standing wave (sw) discharge is characterized by a modulation of the electron density along the direction of propagation [106], which is schematically shown in fig. 4.9. If the termination of the (travelling) surface wave is done such that the length L_{sw} of the resulting sw discharge is about half the length of the unterminated travelling discharge at the same incident power, the initial linear decrease in n_e is entirely suppressed and purely dominated by the interference between launched and reflected surface wave. Consequently, there is a significant difference Δn_e between the electron densities at the end of the sw and the tw discharge, and one obtains a substantially higher electron and hence power density in the case of a standing SWD. As a result, one expects both a higher dissociation rate and gas temperature, which explains the higher value of ΔT_{gt} observed for the sw discharge compared to the tw discharge.

4.4 Summary

A modified waveguide surfatron plasma source based on 2.45 GHz surface wave propagation has been set–up to provide high power densities in the discharge. High power transfer efficiencies from the MWS to the discharge are achieved owing to a careful design of the field applicator.

The discharge behaviour can be understood based on the discharge model from section 3 and on the general description of surface wave discharges. This has allowed to optimize the plasma source in order to obtain a high degree of dissociation at a low oxygen admixture.

Studies of the atomic losses in the plasma afterglow have revealed a low wall recombination rate on a properly prepared discharge tube surface. The description of the volume recombination losses agrees quantitatively with the measured data. As a result, a high atomic fraction of 75 % can be concluded at the end of the plasma column also for higher pressure levels. It has been found, that the power density at the discharge end can be increased substantially by creating a standing wave discharge, where the surface wave is reflected at the end of the discharge tube. The properties of the MWS sustained hydrogen and deuterium discharge investigated have yielded important information for the dissociator design, which is described in the next section.

5 The Dissociator

5.1 General design criteria

For the design of the new MWS based dissociator (MWSD), the the properties of the MWS plasma source as well as geometric restrictions and the common experimental conditions of the HERMES experiment were considered.
The most important requirements are:

1.) Geometrical compatibility with the RF–dissociator in order to allow a quick change–over to the new dissociator.

2.) Remote control operation.
During accelerator operation the radiation shielding separates the experimental area from the controlling units. Hence any device utilized inside the shielding has to be operated remotely.

3.) Long–term stable and reproducible operation.
Facing the typical running mode of the HERMES–experiment, a stable atomic fraction in the nozzle beam of the ABS dissociator is required for at least eight hours with the possibility of nozzle regeneration within two hours.

An overview drawing of the MWSD is shown in fig. 5.1. In order to be compatible with the RF–dissociator, all dissociator parts are mounted on a common flange with an outer diameter of 300 mm. The total dissociator length is about 1150 mm, and the distance from the dissociator flange to the nozzle tip is 470 mm.

In the following, the implementation of the MWS within the dissociator is described in section 5.2, and the nozzle cooling and temperature regulation system in section 5.3.

5.2 Implementation of the plasma source

In order to separate the plasma source from the dissociator chamber vacuum, the front coaxial section of the MWS is accomodated in a cylindrical vessel. From the test bench studies performed with the MWS, one can conclude that the distance d_{cn} between the coupling slit and the nozzle entrance should be variable. Therefore the MWS is mounted such, that it can be slided over the discharge tube by a linear motion bearing attached to the dissociator flange. By means of a 350 mm long coaxial section front part, d_{cn} can be varied between 15 and 30 cm. This allows the distance d_{pn} between nozzle entrance and plasma end to be optmimized with respect to the desired characteristics of the nozzle beam, independent of the microwave power needed to provide a maximum atomic fraction in the discharge. For instance, concerning beam formation, small values of d_{pn} and hence

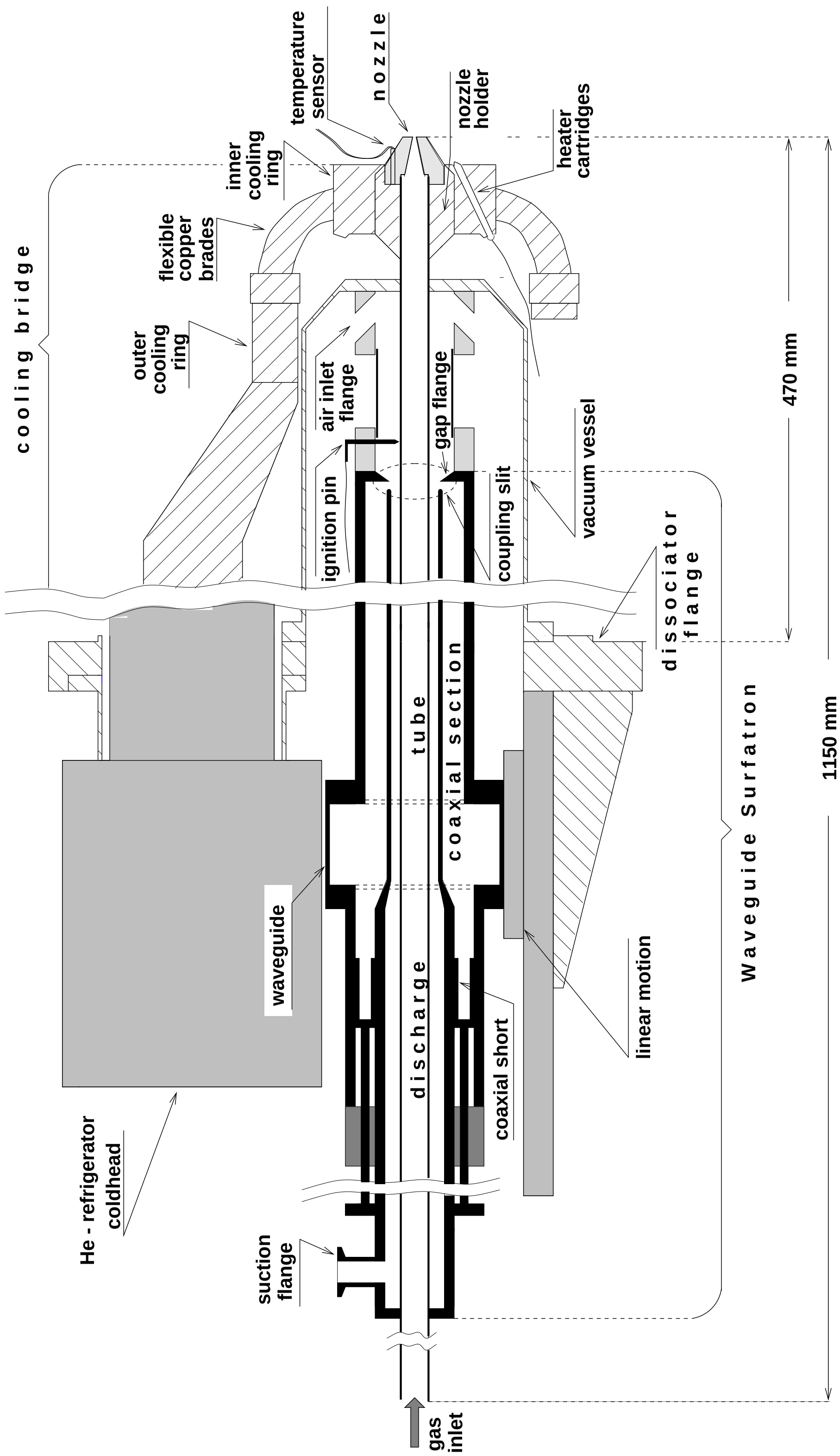

Fig. 5.1: Side view of the waveguide surfatron based dissociator. The different components are explained in the text.

high gas temperatures close to the nozzle entrance may result in an unwanted broadening of the velocity distribution [107] and consequently in a reduced transmission of the sixpole magnet system. On the other hand, it has been shown that high power densities are required in order to efficiently dissociate high gas throughputs and pressures. Therefore, one might aim for the production of a standing surface wave discharge, which requires low distances d_{cn} and high incident microwave powers.

The discharge tube is air cooled using a rotary pump (BECKER, VTA 140) with a nominal pumping speed of $140\,\mathrm{m}^3/\mathrm{h}$. Ambient air is sucked into the angular cooling channels of the air inlet flange, which guides the coolant to downstream end of the discharge. From there the cooling air flows along the discharge tube, being guided by means of a coaxial glass tube and by the coaxial inner conductor. The connection to the rotary pump is done with the suction flange at the upstream end of the inner conductor. This design provides efficient tube cooling over the whole plasma region. Thermal contact to the cold nozzle provides sufficient cooling of the nozzle sided end of the discharge tube surrounded by vacuum.

The high voltage pin for discharge ignition is placed radially in a plastic flange attached to the end plate of the coaxial section. This flange also supports the coaxial glass tube guiding the cooling air. The pin is mounted using a spring bearing to assure a permanent, but smooth contact to the discharge tube. The axial distance between pin and coupling slit is 50 mm in order to avoid the picking up of microwave stray radiation. For remote control operation of the plasma source, the external magnetron is placed close to the dissociator, whilst the magnetron power supply can be placed outside the shielded experimental area at large distance. Since for a matched steady–state discharge the setting of the impedance matching elements does not change for a large range of incident microwave power and gas throughput, remote control of the high voltage pulser is sufficient for remote operation of the discharge.

5.3 The nozzle cooling system

The geometry of the nozzles for the studies with the MWSD is shown in fig. 5.2. The nozzle has a channel length of 15 mm and a small diameter of 2 mm. This geometry yielded the highest output intensities in case of the HERMES–ABS. The nozzle is mounted onto the nozzle holder with layer of Indium inbetween. The nozzle holder is attached to the discharge tube by means of an Indium solder, which serves to cool the downstream end of the tube.

The nozzle cooling system serves to keep the nozzle at the required low temperature. It has been designed to provide a large nozzle temperature range of $T_{\mathrm{nz}} = 60 \ldots 300\,\mathrm{K}$. Moreover, the nozzle has to be "regenerated" within two hours, which is the minimum time between two luminosity runs of HERA. During a nozzle regeneration cycle, the nozzle is warmed up to room temperature to get rid of the ice layer absorbed on it and cooled down back to the operational temperature of typically 100 K.

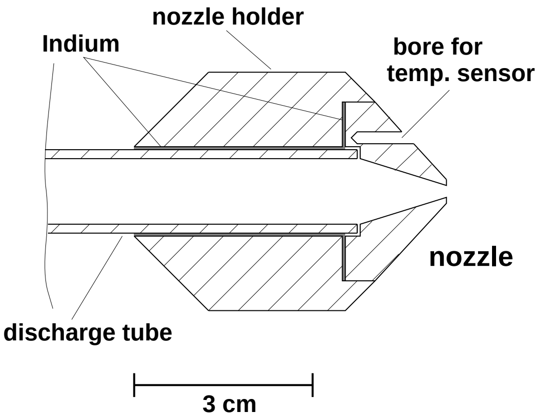

Fig. 5.2: Side view of the nozzle section. The nozzle is mounted on the nozzle holder, which is attached to the discharge tube by means of an Indium solder.

In order to estimate the maximum cooling power needed at the nozzle, a degree of dissociation at the discharge end of $\alpha_{\rm pl} = 1$, a gas throughput of $Q_{\rm m} = 5\,{\rm mbar\,l/s}$ and a surface recombination loss on the nozzle of 50 % of the atoms produced in the discharge are assumed. Hence the heating power deposed at the nozzle is

$$P_{\rm rec} = 2\,Q'_{\rm m}\,(1-\alpha_{\rm pl})\,E_{\rm rec} = 45\,{\rm W}\,.$$

In order to reach nozzle temperatures as low as 50 K, a one–stage closed cycle helium refrigerator coldhead (LEYBOLD, RGS 120) is employed, supplied by a powerful He compressor (LEYBOLD, RW 6000). This system provides a cooling power of 60 W at a cold surface temperature of $T_{\rm cs} = 50\,{\rm K}$ [108]. As shown in fig. 5.1, a massive copper cooling bridge connects the cold surface of the coldhead with the nozzle. The main design features of the cooling bridge are similar to that of the present version of the HERMES–ABS RF–dissociator [43]. However, some important changes have been made in the present design. The bridge consists of a rigid cold arm attached to the cold surface. At the nozzle sided end of the cold arm, the outer cooling ring is mounted, which is connected to the inner cooling ring surrounding the nozzle via 20 flexible, radial copper braides. Owing to this design, radial forces on the glass tube are avoided, since the flexible copper braides compensate the axial contraction of the cold arm during the cooling down phase.

The total length $l_{\rm b}$ of the cooling bridge from the cold surface to the nozzle is about 400 mm. In order to obtain a sufficient heat conductivity, the mean cross section of the bridge components can be estimated as

$$A_{\rm b} = \frac{l_{\rm b}\,(P_{\rm rec}+P_{\rm rad})}{\kappa_{\rm b}\,(T_{\rm nozzle}-T_{\rm cs})}\,, \tag{5.1}$$

where $P_{\rm rad}$ is the heating power because of radiation from the environment and $\kappa_{\rm b}$ is the specific heat conductivity of the cooling bridge.

P_{rad} is a function of the surface areas of the cooling bridge and of the inner wall of the vacuum chamber surrounding the dissociator as well as of the respective emission coefficients and has been estimated to be about 10 W [43]. Assuming a temperature of the cold surface of $T_{\mathrm{cs}} = 47\,\mathrm{K}$ at a heating power of 55 W [108], a mean specific heat conductivity of copper of $\kappa_{\mathrm{b}} = 8\,\mathrm{W/(cm\ K)}$ [109], a cross sectional area of about $A_{\mathrm{b}} = 21\,\mathrm{cm}^2$ is required for a sufficient nozzle cooling. The actual cross sections and lengths of the different cooling bridge components and their lengths are listed in table 5.1.
Inserting the actual total length of the cooling bridge of $l_{\mathrm{b}} = 361\,\mathrm{mm}$ into eq. (5.1), one

component	length	total cross sectional area
cold arm	230 mm	$19.6\,\mathrm{cm}^2$
outer cooling ring	40 mm	$101\,\mathrm{cm}^2$
20× copper brades	70 mm	$25\,\mathrm{cm}^2$
inner cooling ring	21 mm	$44\,\mathrm{cm}^2$

Tab. 5.1: Lengths in parallel and total cross sectional areas perpendicular to the heat flux of the several cooling bridge components.

can see that the cross sectional area of $19.6\,\mathrm{cm}^2$ is still sufficient in order to provide the required heat conductivity.

The total mass of the cooling bridge has been determined to be $m_{\mathrm{b}} \approx 9.5\,\mathrm{kg}$. Hence the time needed to cool down the nozzle from room temperature to the typical operational temperature of 100 K can be estimated as

$$t_{\text{cool-down}} = \frac{c_{\mathrm{Cu}}\, m_{\mathrm{b}}\, (300\,\mathrm{K} - 100\,\mathrm{K})}{\bar{P}_{\mathrm{c}}} \approx 80\,\mathrm{min},$$

where $c_{\mathrm{Cu}} = 0.38\,\mathrm{J/(g\ K)}$ is the specific heat capacity of copper [110] and $\bar{P}_{\mathrm{c}} \approx 150\,\mathrm{W}$ is the mean cooling power provided by the coldhead in the relevant temperature range [108]. Given the minimum time between two luminosity runs of 2 h, the time $t_{\text{warm-up}}$ needed to warm up the nozzle to room temperature must not exceed 40 min. Consequently, the heating power applied to the cooling bridge has to be at least 300 W. In order to provide this significant heating power, ten miniature heater cartridges (TÜRK & HILLINGER, HLP 2.8) with a diameter of 2.8 mm and a maximum heating power of 30 W each are inserted radially symmetric into the inner cooling ring. In contrast to the cooling bridge of the RF–dissociator, where a heater wire is wrapped around the cold arm, the position of the heater cartridges close to the nozzle has two major advantages:

(i) When the nozzle is warmed up, the power is first deposited in the inner cooling ring. Hence the time needed for the nozzle to reach room temperature is expected to be less than $t_{\text{warm-up}} = 40\,\text{min}$ calculated for the entire cooling bridge. Additionally, the temperature gradient between nozzle and cold head should leave the cold arm at lower temperature compared to warmed up nozzle. In conclusion, the regeneration time of the nozzle is expected to be less than the value calculated above.

(ii) Temperature regulation is facilitated, since the response time of the nozzle temperature to a change of the heating power is minimized.

In order to provide a stable output intensity, the nozzle temperature has to be stabilized at the value which yields an optimum transmission through the sixpole system. In case of the MWSD, the nozzle temperature is measured with a standard Pt 100 resistor inserted into the nozzle. The measured value is read out by a proportional–integral–differential (PID) regulator (SIEMENS, Sipart DR 19), which controls the power supply for the heater cartridges.

During operation, the characteristics of the nozzle cooling system have been found to meet the estimations from the design considerations. In table 5.2 the main characteristics are summarized for typical running conditions of the dissociator.

cooling down time $(300\,\text{K} \rightarrow 100\,\text{K})$	$85\,\text{min}$
minimum warm up time $(100\,\text{K} \rightarrow 300\,\text{K})$	$35\,\text{min}$
minimum achievable temperature	$45\,\text{K}$
range of temperature regulation	$45\ldots300\,\text{K}$
temperature fluctuations	$< 0.5\,\text{K}$

Tab. 5.2: Main operational characteristics of the nozzle cooling system.

5.4 Summary

The design of the MWSD has been based on the experiences from the test bench studies with the MWS plasma source. As a consequence, the distance between the coupling slit and the nozzle entrance can be varied over a wide range independent of the applied microwave power.

The MWSD fulfills the technical requirements arising from the running conditions of the HERMES–experiment. It is compatible with the presently used RF–dissociator and can be operated remote controlled. The nozzle cooling system provides stable nozzle temperature over a wide range and allows to regenerate the nozzle in the minimum time of two hours between two luminosity runs of the HERA collider.

In order to verify whether the MWSD provides the required high and stable degree of dissociation in the nozzle beam, an atomic beam test stand with various diagnostics has been set up, which is described in the following section.

6 The Atomic Beam Test Stand

6.1 Overview

In order to study the properties of the nozzle beam provided by the MWSD, an atomic beam test stand (ABT) has been set up. This accomodates various diagnostic tools for the investigation of:

(i) The degree of dissociation.

(ii) Beam formation and attenuation.

(iii) The longitudinal velocity distribution.

A schematic overview of the ABT is given in fig. 6.1. Basically, the ABT consists of a

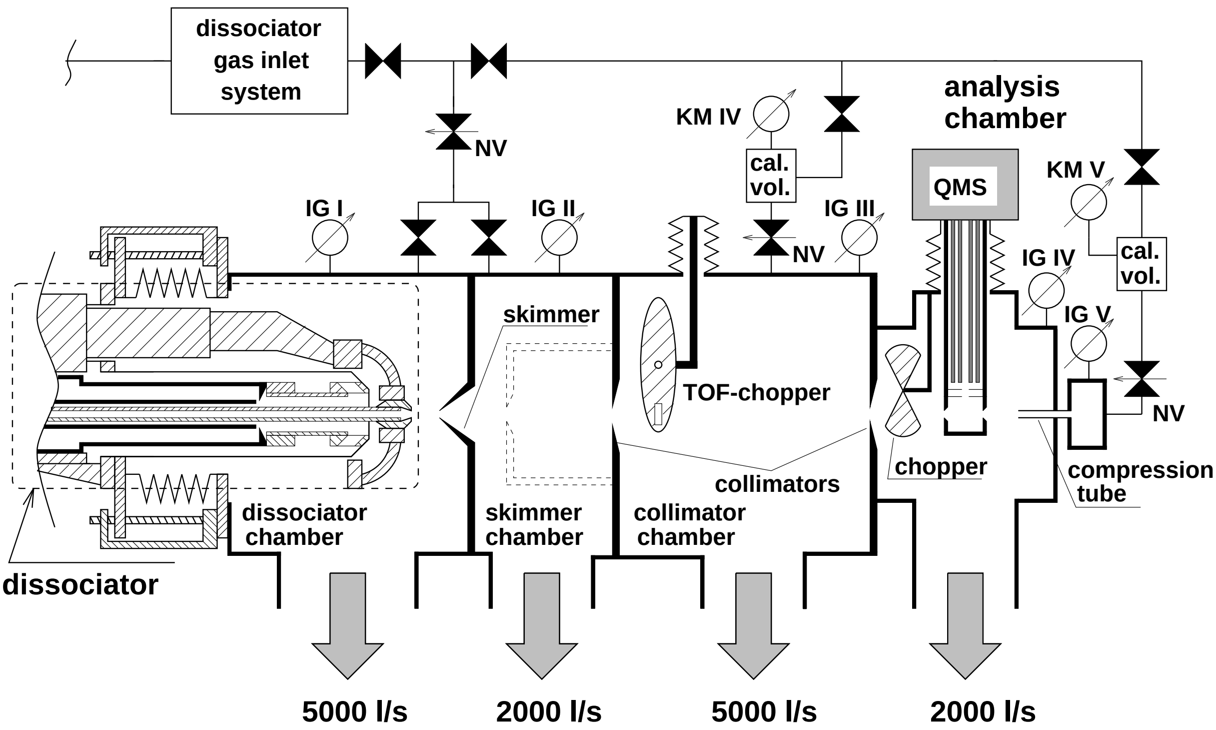

Fig. 6.1: Schematic picture of the Atomic Beam Test Stand (ABT). The symbols NV, IG and KM denote needle valves, ion and capacitive pressure gauges. The large arrows indicate the effective pumping speed.

four–stage, differentially pumped vacuum system with a total effective pumping speed for hydrogen of 14,000 l/s. All vacuum chambers are pumped by means of turbomolecular pumps or a combination of turbomolecular and cryo pumps, with its own forevacuum system for each chamber. A detailed view on the chamber geometries and aperture sizes is given in Appendix E. The first three chambers have a cylindrical shape with a nominal diameter of 400 mm and are attached to each other by means of standard ISO–K connections. The chambers are mounted on two rails with two linear motion bearings per chamber. The mounting is done such, that the separating apertures can be precisely aligned to the chamber axis.

In the dissociator chamber, the MWSD is mounted on a large manipulator with a free diameter of 250 mm. The manipulator allows for axial variation of the nozzle–to–skimmer distance in a range of about 5 . . . 80 mm. Axial movement is performed by means of four coupled mandril–driven linear motion bearings. Those can be decoupled from each other to provide the possibility of a spatial adjustment of the nozzle position with respect to the chamber axis. A large side window is mounted, through which the discharge outside the vacuum vessel of the MWSD can be observed. A photograph of the dissociator mounted on the atomic beam test stand is shown in fig. 6.2. The dissociator chamber is pumped by two turbomolecular pumps (PFEIFFER, TPH 2200) with a total effective pumping speed of about 5000 l/s. Forevacuum is provided using either a rotary pump (PFEIFFER, DUO 170) or a pump stand consisting of a rotary pump and a Roots blower (LEYBOLD, SV 200 and WS 1001). A knife–edged skimmer with a diameter of 6.4 mm separates the dissociator chamber from the skimmer chamber.

The skimmer chamber has an initial length of 300 mm. It can be adapted to the compact skimmer–collimator geometry of the HERMES–ABS by means of cylinder shaped separation baffles, as indicated by the dashed lines. Two turbomolecular pumps (LEYBOLD, Turbovac 1000 and PFEIFFER, TPH 1600) provide an effective pumping speed of about 2000 l/s. The forevacuum system consists of a rotary pump and a Roots blower (LEYBOLD, Trivac D 65 B and WS 251). The skimmer chamber is separated from the collimator chamber by means of a plane knife–edged collimator with a diameter of 11 mm.

In the collimator chamber, a fast rotating chopper wheel with a narrow slit for time–of–flight (TOF) measurements is mounted. The chopper frequency is as high as 310 Hz resulting in a maximum circumference velocity at the slit position of about 100 m/s. This reduces strongly the influence of the opening function of the chopper slit. The unit consisting of water cooled chopper motor and chopper wheel is placed on an axial manipulator with a mandril–driven linear motion bearing, so that the slit of the chopper wheel can be precisely aligned to the beam axis. A high effective pumping speed of about 5000 l/s is achieved, owing to a cryo pump (LEYBOLD, RPK 3500) and a widerange turbomolecular pump (PFEIFFER, TPH 450), the forevacuum of which is provided by a rotary pump (PFEIFFER, DUO 030) followed by an oil trap. A second collimator with a diameter of 7 mm separates the collimator chamber from the analysis chamber.

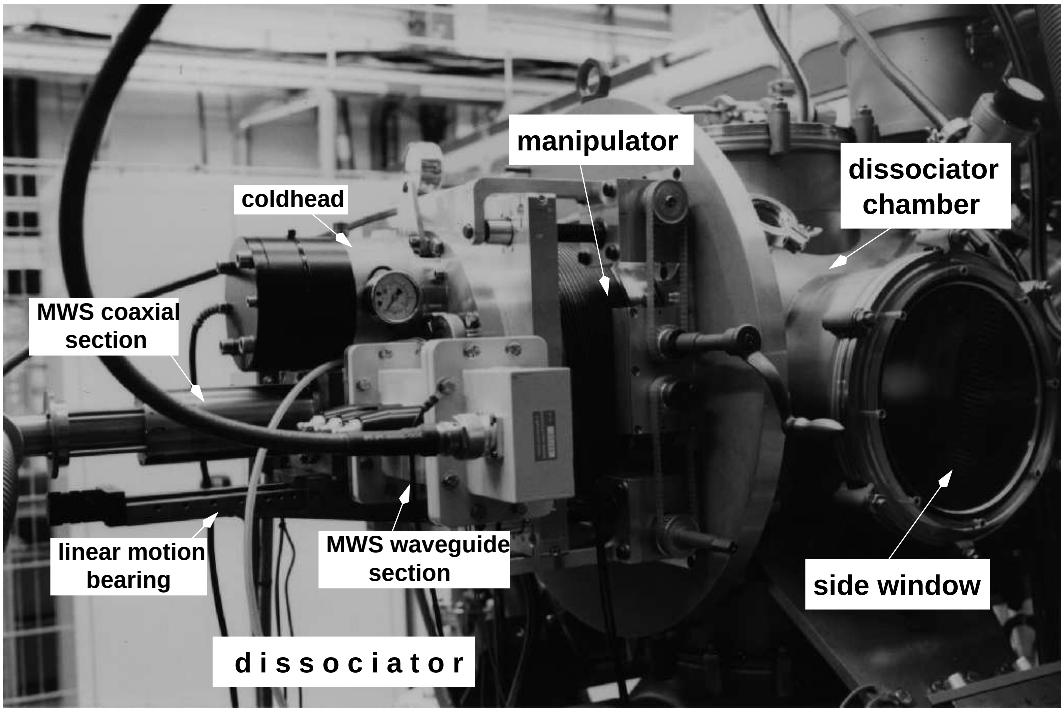

Fig. 6.2: Photograph of the MWSD mounted at the dissociator chamber by means of a large manipulator. The different dissociator components according to fig. 5.1 are mentioned as well.

The analysis chamber is based on a T–piece with a nominal tube diameter of 250 mm. It is attached to the rear of the collimator chamber. In the analysis chamber, the main diagnostic tools of the ABT are accomodated. These are a quadrupole mass spectrometer (QMS) and a calibrated compression tube (CT), which are placed in an axial distance to the skimmer of about 1100 mm and 1250 mm, respectively. The two mass spectrometers used (either VG, Masstorr DX 100, or BALZERS, modified Prisma 200 analyzer with QME 125 and QMG 422 electronics) have open crossed–beam electron sources providing electron energies of 65 eV and 70 eV, respectively. Both mass spectrometers are equipped with a faraday cup (FC) and an off–axis channeltron secondary electron multiplier (CEM) as detectors. In front of the QMS, a motor–driven six–bladed chopper wheel with a frequency range of 10 . . . 100 Hz and a hand driven beam flapper (not shown in fig. 6.1) are mounted in order to separate the beam partial pressure from the residual gas pressure in the analysis chamber. The chopper frequency triggers a lock–in amplifier (EG & G, Model 5209). This is used to determine directly the background–corrected beam partial pressures. Since the QMS is mounted on an axial manipulator, it can be precisely aligned with respect to the chamber axis for the determination of the partial pressures in the beam, or removed out of the beam path in order to perform intensity measurements by means of the compression tube. The CT has an inner diameter of 10 mm and a length of 100 mm in order to simulate the conductance of the storage cell entrance tube. It is attached to a small vacuum chamber, the pressure gauge of which is calibrated following the principle described below. The effective pumping speed in the analysis chamber is 2000 l/s provided by a cryo pump (LEYBOLD, RPK 1500) and a turbomolecular pump (LEYBOLD, Turbovac 360), which is pumped by a rotary pump (LEYBOLD, Trivac D 16 B) followed by an oil trap.

All chambers of the ABT are equipped with pirani manometers (LEYBOLD, TR 211 KF) reading out the pressure for interlock issues in a range between 10^{-3} mbar and 1000 mbar, and with ion gauges (LEYBOLD, IM 221 and ITR 100) for a precise determination of the pressure in the range of $10^{-8} \ldots 10^{-2}$ mbar.

A system of calibrated volumes and needle valves is used for the gas inlet into the dissociator as well as for rest gas injection into the various vacuum chambers. The gas inlet and flux calibration system is described in section 6.2. As shall be shown in section 6.3, the dimensions of the various apertures and the pumping speeds have been chosen to achieve suitable conditions for measurements involving the mass spectrometer or the compression tube. In order to assure safe and reliable running, all components of the atomic beam test stand are controlled by a computer based interlock system. Together with the data aquisition system, the required long–term studies with the MWSD can be performed. Interlock and and data aquisition are described in section 6.4.

6.2 Gas inlet and flux calibration

The dissociator gas feed system is schematically shown in fig. 6.3. It consists of two gas supply systems, one for H_2 or D_2 and one for O_2 or Ar. The necessity of an oxygen admixture has been discussed previously. Argon is used for discharge tests and as purge gas.

At the gas bottles, which are typically filled up to 200 bar, two–stage pressure reducers (DRUVA, Series 500) are mounted to reduce the pressure to about 1.2 bar. Because of safety issues, the gas bottles are placed outside the experimental hall of the ABT. The gases are fed into calibrated volumes using ultra–clean electro–polished stainless steel tubes (DOCKWEILER, TCC quality). Each volume is equipped with a capacitive pressure gauge (LEYBOLD, CM 1000) and an electromagnetic dosing valve (BALZERS, RME 010), which is regulated by a proportional–integral (PI) regulator (BALZERS, RVE 040). The gas inlet into the discharge tube is performed using needle valves, in front of which a shut–off valve is placed. The pressure in the dissociator is measured with a capacitive gauge (LEYBOLD, CM 10).

The flux calibration of the gas inlet into the dissociator as well as into the different vacuum chambers is based on the measurement of the pressure decay in a calibrated

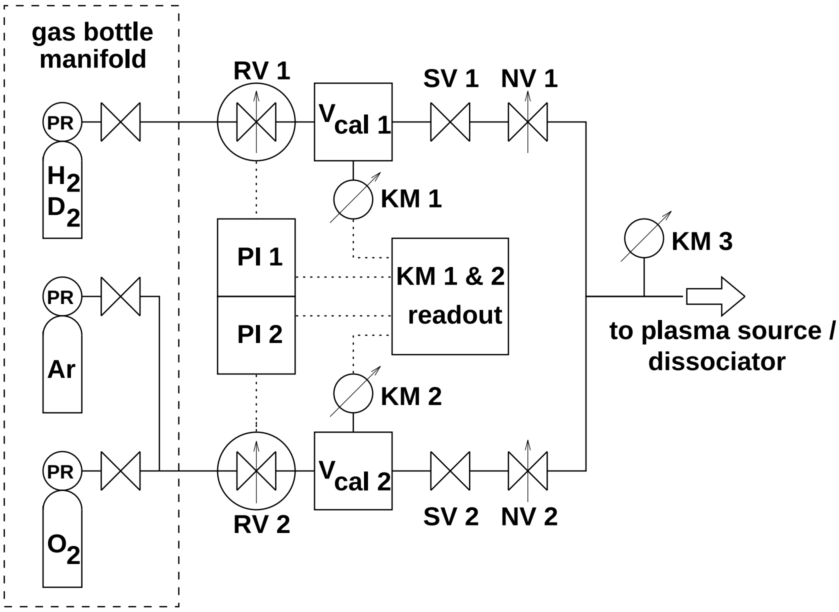

Fig. 6.3: Scheme of the dissociator gas inlet system. The PR are pressure reducers, RV 1/2 electromagnetic dosing valves, PI 1/2 proportional–integral regulators, SV 1/2 shut off valves, NV 1/2 needle valves, $V_{\mathrm{cal}\ 1/2}$ calibrated volumes and KM 1/2/3 capacitive pressure gauges.

volume V_{cal}. The flow Q out of the volume is given by the time evolution of the pressure p_{cal} as

$$Q = \frac{\mathrm{d}p_{\mathrm{cal}}(t)}{\mathrm{d}t}\, V_{\mathrm{cal}}\,. \tag{6.1}$$

Assuming an exponential decrease with time, i.e.,

$$p_{\mathrm{cal}} = p^0_{\mathrm{cal}}\, \exp\left(-a\, t\right),$$

where $p^0_{\mathrm{cal}} = p_{\mathrm{cal}}(t=0)$ and a is the decay constant, one obtains for the throughput from eq. (6.1)

$$Q = a\, p_{\mathrm{cal}}(t)\, V_{\mathrm{cal}}\,. \tag{6.2}$$

Hence, for each pressure value in the calibrated volume, the corresponding throughput can be determined after a has been obtained from an exponential fit to the time evolution of p_{cal}.

For a calibration of the molecular hydrogen flow Q_{m} out of the dissociator nozzle, the calibrated volume with $V_{\mathrm{cal}\ 1} = 3.10\,\mathrm{l}$ is filled to about $p^0_{\mathrm{cal}} = 1000\,\mathrm{mbar}$. A typical flux calibration measurement is shown in fig. 6.4. The pressure in the calibrated volume and the discharge tube pressure have been recorded by the data aquisition system (see section 6.4) every ten seconds for 30 min, corresponding to 180 data points. Due to the

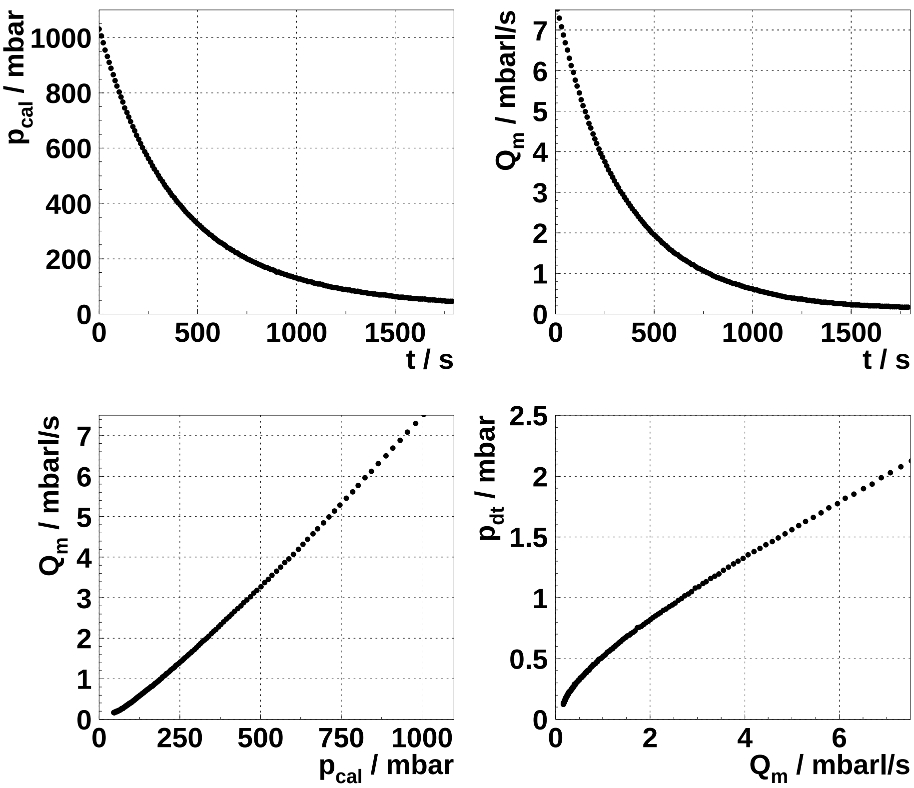

Fig. 6.4: Example of a flux calibration for the dissociator gas inlet. From the time evolution of the pressure in the calibrated volume $p_{\mathrm{cal}}(t)$, the gas throughput $Q_{\mathrm{m}}(t)$ is calculated, and one obtains the throughput as a function of the pressure in the calibrated volume and the pressure in the discharge tube p_{dt} as a function of the throughput.

wide spread in p_{cal}, the flow regime through the needle valve and hence its conductance change, resulting in a non–exponential decay of $p_{\mathrm{cal}}(t)$. This problem is circumvented fitting each datapoint $p_{\mathrm{cal}}(t_n\,, n = 1 \ldots 180)$, exponentially in the range $p_{\mathrm{cal}}(t_{(n-15)}) \leq p_{\mathrm{cal}}(t_n) \leq p_{\mathrm{cal}}(t_{(n+15)})$. The resulting decay constants a_n are then used to calculate the throughput $Q_{\mathrm{m}}(t_n)$. This yields the dependence of the throughput on the pressure in the calibrated volume $Q_{\mathrm{m}}(p_{\mathrm{cal}})$ at a fixed position of the needle valve, and the pressure in the discharge tube $p_{\mathrm{dt}}(Q_{\mathrm{m}})$ as a function of throughput. Hence the throughput can be varied over a wide range by setting p_{cal} to the corresponding value. For dissociator operation with a constant throughput, p_{cal} is stabilized by the PI regulator controlling the voltage of the electromagnetic dosing valve.

The gas inlet and flow calibration system provides an adjustable throughput over a wide range with a systematic uncertainty of less than 1 % determined by the precision of the capacitive gauge and the uncertainty in the determination of V_{cal}. For constant throughput operation, the fluctuations in $p_{\rm cal}$ have been found to be below 0.2 %.

The flux calibration of the ion gauges by means of a rest gas injection system in each of the pumping stages as well as the calibration of the compression tube ion gauge follow the same principle. For rest gas injection into the dissociator chamber and the skimmer chamber, the calibration volume for the dissociator gas inlet is used. The collimator chamber and compression tube chamber have their own flux calibration unit each, which consists of a calibrated volume, a capacitive gauge (LEYBOLD, CR 090) and a needle valve (BALZERS, UVD 035).

6.3 Differential pumping layout

In the following it shall be shown, that the differential pumping layout of the ABT satisfies the requirements for precise beam diagnostics. As mentioned previously, the main diagnostic tools of the ABT are a crossed–beam quadrupole mass spectrometer and a calibrated compression tube.
For precise beam diagnostics with the QMS, two conditions have to be fulfilled:

1.) The contribution of residual gas to the nozzle beam arising from effusive flow between the pumping stages has to be negligible.

2.) The background pressure in the analysis chamber must be sufficiently low in order to obtain a high signal–to–background ratio.

For the estimate of the effusive flow contribution arising from the dissociator chamber, the skimmer is assumed to be a point–like effusive source. Taking into account eq. (2.1), the effusive flow from the skimmer into the ionisation volume of the QMS can be written as

$$Q^{\rm eff}_{\text{dis-ch}} = \left(p^{\rm rg}_{\text{dis-ch}} - p^{\rm rg}_{\text{sk-ch}}\right) \, C_{\rm sk} \, \left(1 - \cos^2 \vartheta'_{\rm iv}\right) \, , \tag{6.3}$$

where $p^{\rm rg}_{\text{dis-ch}}$ and $p^{\rm rg}_{\text{sk-ch}}$ are the rest gas pressures in the dissociator chamber and the skimmer chamber, $C_{\rm sk}$ is the skimmer conductance, and $\vartheta'_{\rm iv}$ is the polar opening angle of the QMS ionisation volume with respect to the skimmer.
Neglecting beam attenuation and assuming the nozzle to be a point–like source, the rest gas pressure in the dissociator chamber is given as

$$p^{\rm rg}_{\text{dis-ch}} = \frac{1}{\mathcal{S}_{\text{dis-ch}}} \, Q_{\rm m} \, \cos^{n+1} \vartheta_{\rm sk} \, , \tag{6.4}$$

where $Q_{\rm m}$ is the nozzle throughput, $\vartheta_{\rm sk}$ is the skimmer opening angle with respect to the nozzle and $\mathcal{S}_{\text{dis-ch}}$ is the effective pumping speed in the dissociator chamber.
The ballistic flow from the nozzle into the QMS ionisation volume can be written as (again neglecting attenuation)

$$Q^{\rm bal}_{\rm nz} = Q_{\rm m} \, \left(1 - \cos^{n+1} \vartheta_{\rm iv}\right) \, , \tag{6.5}$$

where ϑ_{iv} is the opening angle of the QMS ionisation volume with respect to the nozzle. For a given skimmer conductance and effective pumping speed in the dissociator chamber, the effusive contribution from the dissociator chamber $\xi_{\text{dis-ch}}$ to the total flow into the QMS will be maximum for $p^{\text{rg}}_{\text{dis-ch}} \gg p^{\text{rg}}_{\text{sk-ch}}$ and $n \to 1$. Taking into account that $\vartheta'_{\text{iv}} \approx \vartheta_{\text{iv}}$, one can write:

$$\xi_{\text{dis-ch}} \equiv \frac{Q^{\text{eff}}_{\text{dis-ch}}}{Q^{\text{eff}}_{\text{dis-ch}} + Q^{\text{bal}}_{\text{nz}}} \leq \frac{(C_{\text{sk}}/\mathcal{S}_{\text{dis-ch}})\,\cos^2\vartheta_{\text{sk}}}{(C_{\text{sk}}/\mathcal{S}_{\text{dis-ch}})\,\cos^2\vartheta_{\text{sk}} + 1} < \frac{C_{\text{sk}}/\mathcal{S}_{\text{dis-ch}}}{(C_{\text{sk}}/\mathcal{S}_{\text{dis-ch}}) + 1}\,. \tag{6.6}$$

The conductance of the applied skimmer can be calculated as [32]

$$C_{\text{sk}} = A_{\text{sk}}\sqrt{\frac{R\,T_{\text{sk}}}{2\,\pi\,M_{\text{mol}}}} = \begin{cases} 14.3\,\text{l/s for } H_2 \\ 10.1\,\text{l/s for } D_2 \end{cases}$$

where A_{sk} is the skimmer cross section, R is the gas constant, $T_{\text{sk}} = 300\,\text{K}$ the skimmer temperature and M_{mol} the molar mass.
Consequently, considering the effective pumping speed in the dissociator chamber of $\mathcal{S}_{\text{dis-ch}} = 5000\,\text{l/s}$, the maximum effusive contribution from the dissociator chamber to the total flow into the QMS can be estimated as $\xi_{\text{dis-ch}} < 3 \times 10^{-3}$.

Similar calculations have been done to estimate the effusive contributions from the other ABT chambers. It has been found, that for the given collimator sizes and effective pumping speeds, the largest effusive contribution arises from the dissociator chamber. In conclusion, the total effusive contribution to the ballistic nozzle flow can be neglected, as anticipated.

The signal–to–background ratio can be expressed as

$$\mathcal{F} = \frac{p^{\text{iv}}_{\text{beam}}}{p^{\text{an-ch}}_{\text{rg}}}\,, \tag{6.7}$$

where $p^{\text{iv}}_{\text{beam}}$ is the pressure in the beam crossing the QMS ionisation volume and $p^{\text{an-ch}}_{\text{rg}}$ is the residual gas pressure in the analysis chamber.
For the pressure in the beam one can write:

$$p^{\text{beam}}_{\text{iv}} = \frac{Q^{\text{bal}}_{\text{nz}}}{A_{\text{iv}}\,v^{\text{beam}}}\,, \tag{6.8}$$

where A_{iv} is the cross section of the ionisation volume and v_{beam} is the velocity of the beam particles.
In order to get a rough estimate for v^{beam}, the beam particles are assumed to thermalize on the cold nozzle surface, and one obtains[3] (see e.g., ref. [111]):

$$v^{\text{beam}} = \sqrt{\frac{8\,k\,T_{\text{nz}}}{\pi\,m_{\text{a,m}}}}\,,$$

[3]Since the beam expands adiabatically after passing the nozzle exit, the actual mean velocity has been measured to be a factor of up to 1.3 higher than the mean thermal velocity [50].

where the $T_{\rm nz}$ is the nozzle temperature and $m_{\rm a,m}$ is the atomic or molecular hydrogen or deuterium mass.
Since the effusive contribution to the total flow can be neglected, the rest gas pressure in the analysis chamber is given as

$$p^{\rm rg}_{\text{an-ch}} = \frac{Q^{\rm bal}_{\text{an-ch}}}{\mathcal{S}_{\text{an-ch}}}, \quad \text{with} \quad Q^{\rm bal}_{\text{an-ch}} = Q_{\rm m}\left(1-\cos^{n+1}\vartheta_{\rm c2}\right), \tag{6.9}$$

where $Q^{\rm bal}_{\text{an-ch}}$ and $\mathcal{S}_{\text{an-ch}}$ are the ballistic gas flow and the effective pumping speed in the analysis chamber, and $\vartheta_{\rm c2}$ is the opening angle of the second collimator separating the collimator chamber from the analysis chamber.
Taking into account eqs. (6.8) and (6.9), one can estimate the effective pumping speed required in the analysis chamber in order to obtain the desired signal–to–background ratio:

$$\mathcal{S}_{\text{an-ch}} = \frac{\mathcal{F}\,(1-\cos^{n+1}\vartheta_{\rm c2})\,A_{\rm iv}\,v^{\rm beam}}{1-\cos^{n+1}\vartheta_{\rm iv}}. \tag{6.10}$$

Hence the signal–to–background ratio is independent of the nozzle throughput and also independent of n, since $\vartheta_{\rm iv}$ and $\vartheta_{\rm c2}$ are rather small (about $0.075°$ and $0.25°$, respectively). The larger value of $\vartheta_{\rm c2}$ is necessary in order to illuminate the entire cross section of the compression tube with the nozzle beam. Anticipating a high signal–to–background ratio of $\mathcal{F} \geq 10$ also for a nozzle at room temperature, one can estimate the necessary effective pumping speed in the analysis chamber in the case of a molecular hydrogen beam to be about $\mathcal{S}_{\text{an-ch}} \geq 1450\,\text{l/s}$.

Therefore the effective pumping speed of 2000 l/s in the analysis chamber should be sufficient in order provide both a high signal–to–background ratio as well as a low background pressure. This has been verified in the course of a mass scan for hydrogen with the BALZERS–QMS with open and closed beam flapper. For the measurement shown in fig. 6.5, the FC detector has been used. The molecular throughput has been 1.5 mbar l/s, the nozzle temperature 100 K and the atomic fraction in the beam with running discharge was about 0.7. The signal–to–background ratios obtained are 8 : 1 for molecular hydrogen with the discharge switched off and 60 : 1 for atomic and 4 : 1 for molecular hydrogen with running discharge. This result is close to the expected value and demonstrates the proper design of the differential pumping system. The high signal–to–background ratio for atomic hydrogen arises from recombination of atoms on the stainless steel surface of the vacuum chamber, which substantially reduces the atomic background. As a consequence of the high signal–to–background ratio, the background–corrected signals can be determined with a low systematic uncertainty only by using the beam flapper in front of the QMS. This allows important cross–checks for measurements employing the lock–in amplifier.

In summary, one can conclude that the differential pumping layout of the atomic beam test stand provides suitable conditions for a precise diagnostic of the nozzle beam properties.

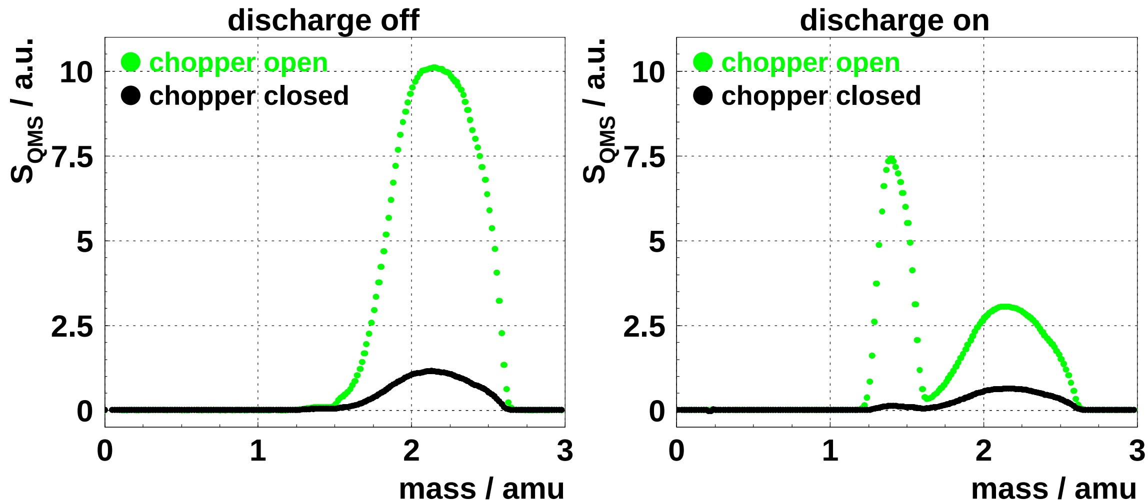

Fig. 6.5: Mass scan for atomic and molecular hydrogen with open and closed chopper measured for switched off and running discharge. Shown are the output voltages of the FC of the QMS in arbitrary units versus the uncorrected mass in atomic mass units.

6.4 Interlock System and Data Aquisition

For safe and reliable operation, all components of the ABT are controlled by an interlock–system. This consists of a computer based relais unit (SIEMENS, SPS S 7), which controls the power switches of the different devices (pumps, He–compressors, etc.) The SPS–unit provides high flexibility in case additional devices are introduced at the ABT. The parameters which are controlled during operation of the various devices are summarized in table 6.1.

In order to read out all relevant parameters needed for a precise beam diagnosis, a data aquisition system has been set up. A schematic diagram of the DAQ is shown in fig. 6.6. The DAQ reads out the analog output voltages of the various devices by means of a 32–channel analog–to–digital converter (ADC) (KINETIC SYSTEMS, 3516), which is linked to the computer (DIGITAL, DECstation 5000/200) via a CAMAC–FASTBUS bus system. This provides a readout of all ion gauges and capacitive manometers, of the nozzle temperature and the heater current for nozzle temperature regulation, as well as of all relevant QMS output signals and of the lock–in amplifier. Additionally, mass selection of the QMS can be performed externally by means of a digital–to–analog converter (DAC) (KINETIC SYSTEMS, 3110).

device	controlled parameters
MWS plasma source	∗ cooling water for magnetron and circulator ∗ discharge tube pressure ∗ discharge tube cooling ∗ nozzle temperature ∗ dissociator chamber pressure ∗ speed of turbo pumps
dissociator gas inlet	∗ discharge tube pressure ∗ dissociator chamber pressure ∗ speed of turbo pumps
nozzle cooling	∗ speed of turbo pumps ∗ cooling water of coldhead He compressor
vacuum system	∗ cooling water for turbo pumps ∗ speed of turbo pumps ∗ pressures in all chambers ∗ power consumption of forepumps ∗ cooling water of cryo pump He compressor
mass spectrometer	∗ pressure in analysis chamber

Tab. 6.1: Parameters of the various ABT devices controlled by the interlock–system

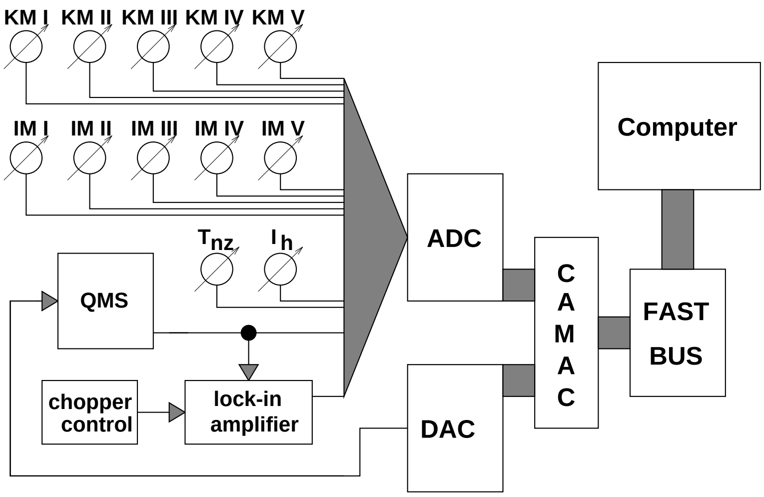

Fig. 6.6: Schemic overview of the data aquisition system for the atomic beam test stand. KM I–V, IM I–V, $T_{\rm nz}$ and $I_{\rm h}$ denote the analog outputs of the capacitive and ionisation pressure gauges and the nozzle temperature and heater current, respectively. ADC and DAC are analog–to–digital and digital–to–analog signal converters.

7 Degree of Dissociation Measurements

The achievable degree of dissociation α in the nozzle beam for given plasma and nozzle parameters is one of the main dissociator characteristics.

In case of the studies presented below, α has been determined by means of a mass spectrometer, where it has been verified in the previous section, that the differential pumping layout of the atomic beam test stand provides suitable conditions for mass spectroscopical investigations.

The principle and systematic errors of the degree of dissociation measurements for the given set–up are discussed in section 7.1. The degree of dissociation has been studied for a large range of plasma source parameters such as gas throughput and incident microwave power (section 7.2) as well as oxygen admixture (section 7.3). The long–term behaviour has been investigated, as shown in section 7.4. In section 7.5, studies on the recombination properties of various nozzle surfaces are presented. Comparative measurements with the radio frequency dissociator of the HERMES–ABS are shown in section 7.6. A summary of the degree of dissociation measurements is given in section 7.7.

The studies presented below are partially published in ref. [95].

7.1 Principle and systematic errors

In order to calculate the ABS output intensity according to eq. (2.11), the intensity–related degree of dissociation α in the nozzle beam at the entrance of the sixpole magnet system is of interest. This is defined via the atomic and molecular partial pressures in the beam taking into account the atomic and molecular velocity:

$$\alpha = \frac{p_{x_1}}{p_{x_1} + 2\,\kappa_v\,p_{x_2}}\,, \tag{7.1}$$

where x = H, D, p_{x_1} and p_{x_2} are the atomic and molecular partial pressures and $\kappa_v = v_{x_2}/v_{x_1}$ is the ratio of the most probable molecular to atomic velocity.
Effusive flow out of the nozzle would result in $\kappa_v = 1/\sqrt{2}$. In case of the given conditions however, the nozzle flow is rather laminar than effusive, as shown in section 2.1. Therefore, an assimilation of the atomic and molecular drift velocities may be expected, resulting from the so–called seeded–beams effect [31]. This expectation is partially confirmed by preliminary results from TOF measurements being currently performed at the ABT [112]. However, it has been found, that the ratio of the most probabale velocities is $\kappa_v \approx 1/\sqrt{2}$ as for the effusive case. Hence, for the studies presented, $\kappa_v = 1/\sqrt{2}$ has been assumed.

Since the degree of dissociation is determined by means of a quadrupole mass spectrometer, the different ionisation and detection probabilities of atoms and molecules have to be taken into account, resulting in:

$$\alpha = \frac{S^*_{x_1}}{S^*_{x_1} - 2\,\kappa_{\text{ion}}\,\kappa_{\text{det}}\,\kappa_v\,S_{x_2}}\,, \tag{7.2}$$

where $S^*_{x_1}$ and S_{x_2} are the background corrected partial pressures measured by the QMS, and κ_{ion} and κ_{det} are the ratios for the atomic–to–molecular ionisation cross sections and detection probabilities, respectively. $S^*_{x_1}$ denotes the atomic signal corrected for the contribution from dissociative ionisation of molecules:

$$S^*_{x_1} = S_{x_1} - \delta^{\text{dission}}\,S_{x_2}, \qquad \delta^{\text{dission}} = \frac{S^{\text{off}}_{x_1}}{S^{\text{off}}_{x_2}} = \begin{cases} 0.0125 & \text{for hydrogen} \\ 0.0085 & \text{for deuterium} \end{cases}$$

where S_{x_1} is the initial atomic signal, and $S^{\text{off}}_{x_1}$ and $S^{\text{off}}_{x_2}$ are the atomic and molecular signals with the discharge being switched off. The contribution to the atomic signal arising from dissociative ionisation of water caused by the oxygen admixture was found to be neglibible. $\kappa_{\text{ion}} = \sigma^{\text{ion}}_{x_1}/\sigma^{\text{ion}}_{x_2}$ can be determined to be 0.64 ± 0.04 for the electron energies of 65 eV and 70 eV provided by the crossed–beam source of the two mass spectrometers used [28, 113]. In case the Faraday cup (FC) is used as detector, κ_{det} is equal to 1. Using the channeltron (CEM), κ_{det} is determined by the different conversion of atomic and molecular ion currents into QMS output voltage signals. κ_{det} can be determined experimentally comparing the atomic–to–molecular signal ratios $(S^*_{x_1}/S_{x_2})_{\text{CEM}}$ and $(S^*_{x_1}/S_{x_2})_{\text{FC}}$ measured with CEM and FC, respectively, as follows:

$$\kappa_{\text{det}} = \frac{\epsilon_{x_1^+}}{\epsilon_{x_2^+}} = \frac{\left(S^*_{x_1}/S_{x_2}\right)_{\text{CEM}}}{\left(S^*_{x_1}/S_{x_2}\right)_{\text{FC}}}\,,$$

where $\epsilon_{x_1^+}$ and $\epsilon_{x_2^+}$ are the conversion rates for atomic and molecular ion currents into CEM voltages. For both mass spectrometers used, κ_{det} has been determined to 0.85, in agreement with ref. [114].

Based on the considerations above, the systematic uncertainty $\Delta\alpha_{\text{sys}}$ in the determination of α is dominated by the error on the ionisation cross sections. Obviously, $\Delta\alpha_{\text{sys}}$ depends on α; $\Delta\alpha_{\text{sys}} \leq 2\,\%$ for $\alpha = 30 \ldots 80\,\%$ and $\Delta\alpha_{\text{sys}} \to 0$ for $\alpha \to 0$ and $\alpha \to 100\,\%$, respectively. If the background corrected QMS–signals S_{x_1} and S_{x_2} are determined with the beam flapper, the signal fluctuations obtained are below 2 %. In order to further reduce the statistical uncertainty, a lock–in amplifier has been used. Setting the chopper frequency and the lock–in integration constant in order to provide about 20 cycles per integration time, the fluctuations have been less than 0.5 %. For the measurements presented below, the lock–in amplifier has been used. Prior to each measurement and to each change in the lock–in settings, the signal ratio S_{x_1}/S_{x_2} obtained with the lock–in has been cross–checked with the corresponding ratio measured by using the beam flapper.

It is important to note, that the degree of dissociation obtained from eq. (7.2) denotes the atomic fraction in the nozzle beam at the position of the QMS. As mentioned above, for a determination of the ABS intensity however, α has to be known at the entrance of the sixpole system. Therefore, the different attenuation of atoms and molecules along the whole path to the QMS has to be considered. As shown later in section 8, the experimental conditions for the degree of dissociation measurements presented here have been such, that differences in the attenuation of atoms and molecules can be neglected. Therefore one can assume, that the measured degree of dissociation is rather close to the atomic fraction at the entrance to the first sixpole magnet.

7.2 Dependence on gas throughput and microwave power

Two of the main plasma parameters affecting the degree of dissociation in the nozzle beam are the gas throughput Q_{m} and the incident microwave power P_{i}. For the following studies, α has been measured in a range of $Q_{\mathrm{m}} = 1 \ldots 5\,\mathrm{mbar\,l/s}$ and $P_{\mathrm{i}} = 180 \ldots 1200\,\mathrm{W}$ for both hydrogen and deuterium. The nozzle used was made of Al 99.5 following the geometry given in fig. 5.2 and was operated at a temperature of 100 K. The oxygen admixture was set to 0.1 . . . 0.2 flux% to obtain a maximum degree of dissociation. A quartz discharge tube has been used, which had been prepared in order to yield a low recombination coefficient as described appendix D.

The dependence of the degree of dissociation α in the hydrogen beam on the incident microwave power P_{i} for various throughput levels Q_{m} is shown in fig. 7.1. In general it is found, that α rises with incident power and decreasing throughput. For gas flows up to 3 mbar l/s, the degree of dissociation rises continuously with increasing microwave power, then saturates and rises again for higher power levels. The highest values in a range of $\alpha = 70 \ldots 80\,\%$ have been obtained for $Q_{\mathrm{m}} \leq 3\,\mathrm{mbar\,l/s}$ and microwave powers of at least 600 W. In this throughput range, the discharge column could always be propagated up to the nozzle entrance, provided the microwave power was sufficiently high. It has also been observed for $Q_{\mathrm{m}} = 1\,\mathrm{mbar\,l/s}$ and a corresponding gas pressure of about 0.7 mbar, that a variation of the distance d_{cn} between coupling slit and nozzle entrance by sliding the MWS on the linear motion bearing over the discharge tube did not affect the degree of dissociation in the nozzle beam. This behaviour is in agreement with the results obtained in the course of the test bench studies presented in section 4.3.2 and confirms the negligible atomic loss rate in the afterglow for a properly prepared discharge tube and low gas pressures. For throughput levels beyond 3 mbar l/s, α decreases continuously to about 43 % at 5 mbar l/s despite of high power levels of up to 1200 W. In this throughput range, the discharge tube pressure is about $p_{\mathrm{dt}} = 2 \ldots 3\,\mathrm{mbar}$, and the discharge ends well before the nozzle entrance, although d_{cn} was set to the minimum of 150 mm. In case of $Q_{\mathrm{m}} \geq 4.0\,\mathrm{mbar\,l/s}$, the plasma column could not even be propagated through the front flange of the vacuum vessel (see fig. 5.1).

The decrease of the degree of dissociation in the nozzle beam with increasing throughput can be explained both by a decrease of the degree of dissociation α_{pl} in the discharge and by atomic losses in the afterglow of the plasma. Taking into account the power den-

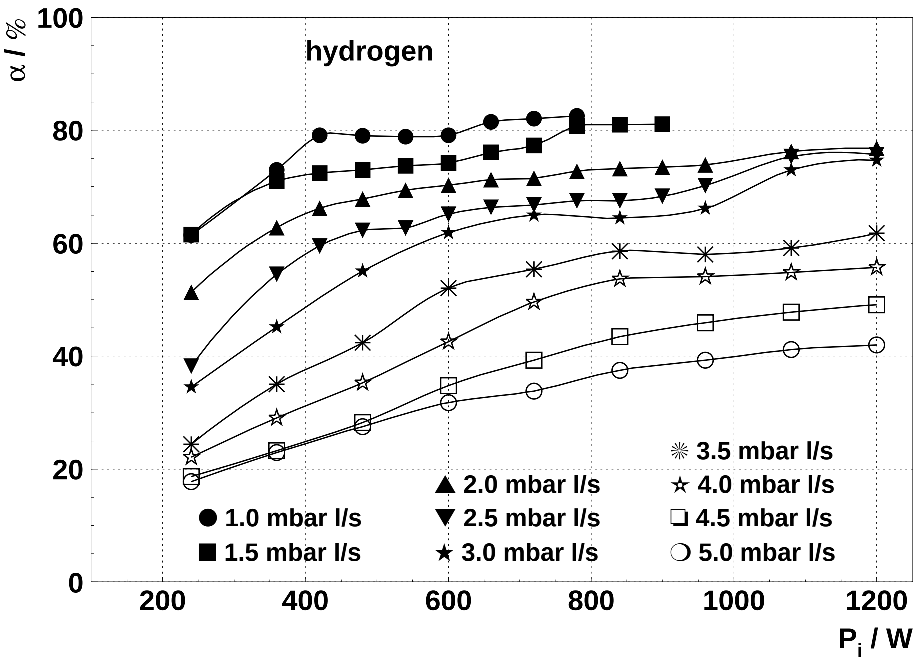

Fig. 7.1: Degree of dissociation α as a function of incident microwave power P_{i} for hydrogen throughput values Q_{m} ranging from 1 mbar l/s to 5 mbar l/s.

sity dependence of α_{pl} (fig. 3.11) as it is predicted by the discharge model in section 3, the measured decrease in α with increasing gas throughput should be caused in first order by throughput–induced atomic losses, which cannot be compensated by a sufficiently high dissociation rate. Considering the results about the MWS plasma source from the test bench studies, the additional rise of α for high microwave powers at throughputs below 3 mbar l/s can be explained by the formation of a standing wave and consequently a higher dissociation rate at the plasma end and hence at the nozzle entrance. Since at a given incident power level, the pressure and consequently the power density rise with increasing throughput, the discharge length decreases. Therefore, the available microwave power is not sufficient to form a standing wave at throughput levels beyond 3 mbar l/s in case of the given minimum distance of $d_{\mathrm{cn}} = 150\,\mathrm{mm}$, and the dissociation rate at the plasma end is not high enough anymore to compensate for the atomic losses. For $Q_{\mathrm{m}} \geq 4.0\,\mathrm{mbar\,l/s}$, additional volume recombination losses in the afterglow contribute to the measured decrease of α.

The dependence of the degree of dissociation in the deuterium beam on incident microwave power and gas throughput is shown in fig. 7.2. A quite similar evolution of α is observed in comparison to hydrogen. The main difference is a higher degree of dissociation in the deuterium beam already at lower microwave power levels, especially

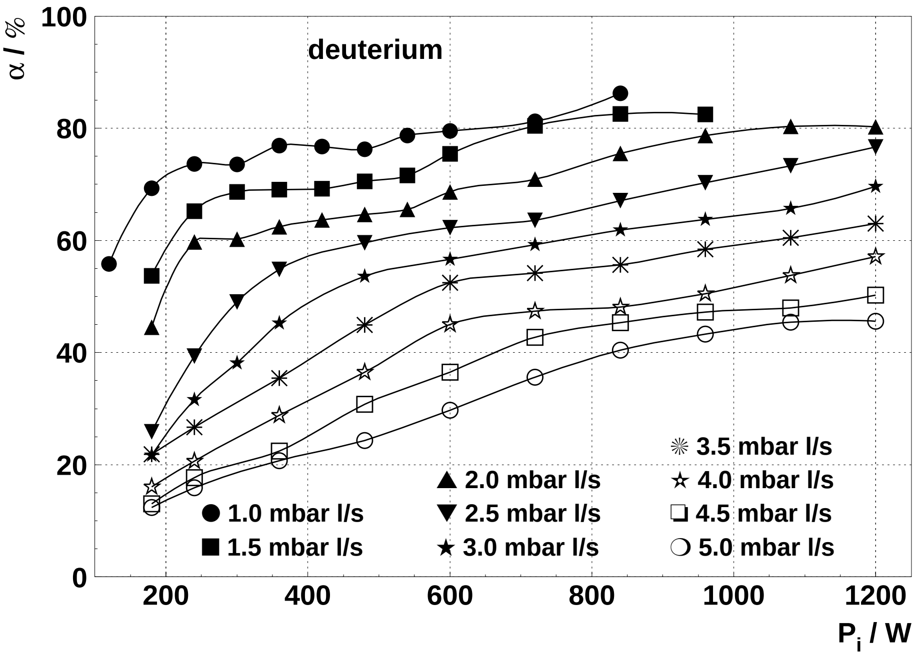

Fig. 7.2: Degree of dissociation α as a function of microwave power $P_{\rm mw}$ for deuterium throughput values $Q_{\rm m}$ ranging from $1\,\rm mbar\,l/s$ to $5\,\rm mbar\,l/s$.

---

for low gas throughputs. This behaviour and the lower oxygen admixture of 0.1 flux% are explained by the lower power loss per electron due to the different mass of deuterium (see section 4.3.2 and eq. (3.21)), by which the elastic energy transfer to the neutrals is reduced. However, in case of deuterium, the nozzle conductance is about 1.3 times higher than for hydrogen. This leads to a 1.3 times higher pressure in the discharge tube at a given gas throughput and consequently, given the same atomic fraction in both gases, to a volume recombination rate which is 1.7 times higher than for hydrogen, since the volume recombination frequency is proportional to the square of the atomic density (see eq. (3.37)). Therefore, the lower power loss per electron in the deuterium discharge is partly compensated by a higher volume recombination rate, which explains the rather similar dependence of α for both hydrogen and deuterium on the incident microwave power for higher gas throughput levels.

As a consequence, the dissociator set–up was changed such, that the minimum distance $d_{\rm cn}$ has been reduced from 150 mm to 90 mm. This should provide the possibility of standing wave propagation and hence a higher power density in the discharge also in case of high gas throughputs. Fig. 7.3 shows the dependence of the degree of dissociation on the gas throughput summarized from the results presented above and the measurements for the reduced distance d_{cn} for both hydrogen and deuterium. The data

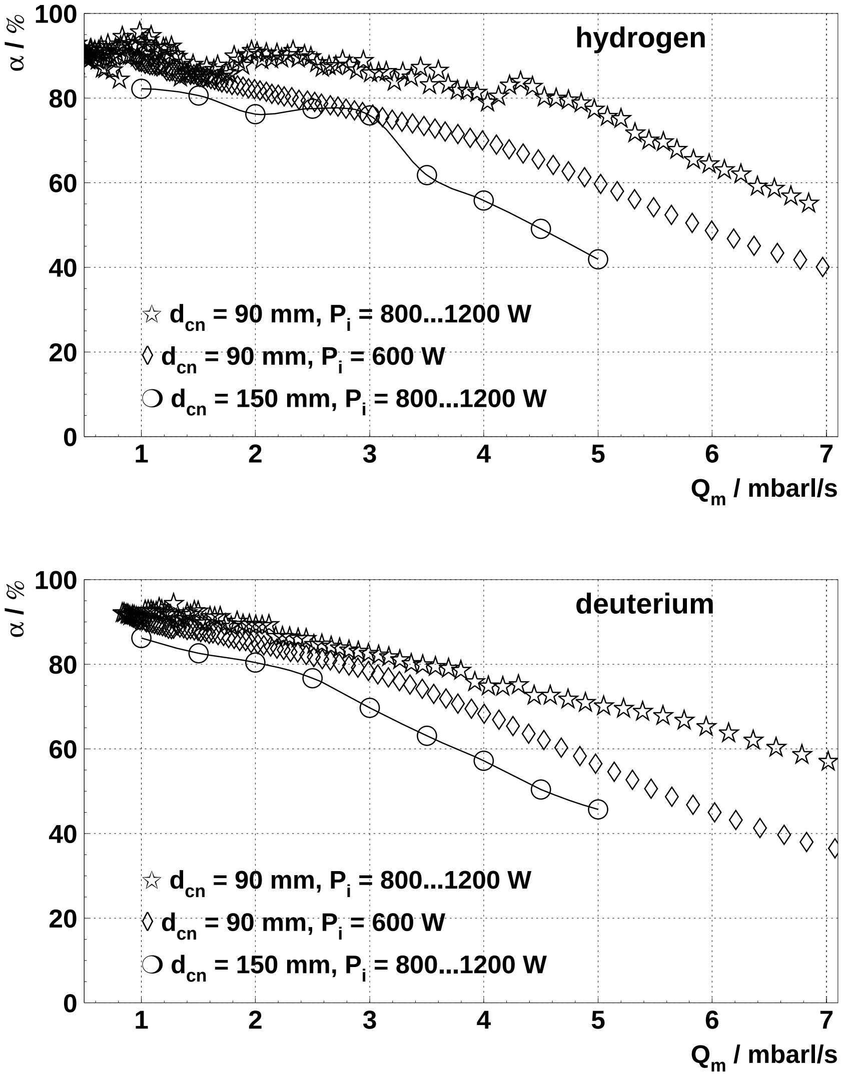

Fig. 7.3: Dependence of the degree of dissociation α on the gas throughput Q_m for hydrogen (upper picture) and deuterium (lower picture). Shown are the summarized data from the previous measurements for a distance between coupling slit and nozzle entrance of $d_{cn} = 150$ mm and the results obtained after reducing d_{cn} to 90 mm for various incident microwave power levels.

for $d_{cn} = 90$ mm have been obtained during a flux calibration with running discharge. In this case, the incident microwave power has been either set to a constant value of 600 W or it has been varied between 1200 W for the range of high Q_m values and 800 W for low gas throughputs[4].

It is found, that in case of reduced distance d_{cn}, the degree of dissociation is clearly higher for both hydrogen and deuterium, especially for gas throughputs of more than 3.0 mbar l/s. This behaviour follows exactly the expectation from above, namely that a reduced distance d_{cn} at a given incident microwave power results in a higher power density in the downstream half of the surface wave discharge and hence a higher dissociation rate close to the nozzle entrance. This effect yields substantial benefits in case of high gas throughputs, where throughput–induced atomic losses and volume recombination in the afterglow are the dominant loss mechanisms.

In summary, the MWSD yields high atomic fractions over a wide range of gas throughputs and pressures. It could be observed, that the creation of a standing wave discharge is necessary in order to efficiently dissociate high gas throughputs. Such a behaviour is simulated by the discharge model from section 3, which predicts the need of high power densities in the discharge in order to compensate for throughput–induced atom losses.

7.3 Influence of the oxygen admixture

In order to verify the results obtained from the test bench studies with the MWS plasma source given in section 4.3, the dependence of the degree of dissociation in the nozzle beam on the oxygen admixture $Q^{\mathrm{rel}}_{\mathrm{O_2}}$ has been studied. For these investigations, the throughput was set to 1.5 mbar l/s, the nozzle temperature was 100 K and the incident microwave power 480 W. α has been measured for two differently prepared discharge tubes made of borosilicate glass. One tube had been solely rinsed by methanol and destilled water, and the other one had been prepared with the acid bath as described in appendix D, which yielded the best results in case of the test bench studies.

As shown in fig. 7.4, for both discharge tubes only a low atomic fraction in the beam is observed for oxygen admixtures below 0.1 flux%. In case of the prepared tube ("tube II"), the degree of dissociation reached its maximum already at $Q^{\mathrm{rel}}_{\mathrm{O_2}} \geq 0.2$ flux% confirming the results from the test bench studies. An about 3 times higher oxygen admixture is required, if the "unprepared" tube ("tube I") is used instead. Studies in which the cooling air flow has been reduced from nominal 140 m^3/h to about 80 m^3/h resulted in an additional increase of the required oxygen content by up to a factor of 2. In comparison with a surface wave dissociator developed at CERN, the required oxygen admixture in case of the MWSD with a prepared discharge tube and the full air cooling flow available, is about five to seven times lower [115, 116, 117, 119].

[4]For gas throughputs below 1.5 mbar l/s and an incident microwave power exceeding about 1000 W, the degree of dissociation suddenly decreased drastically, and at the same time the discharge tube emitted a bright yellowish light indicating that its temperature is close to the melting point. In order to avoid a melting of the discharge tube, the incident microwave power has been continuously decreased from 1200 W to 800 W for gas throughputs below 2.0 mbar l/s.

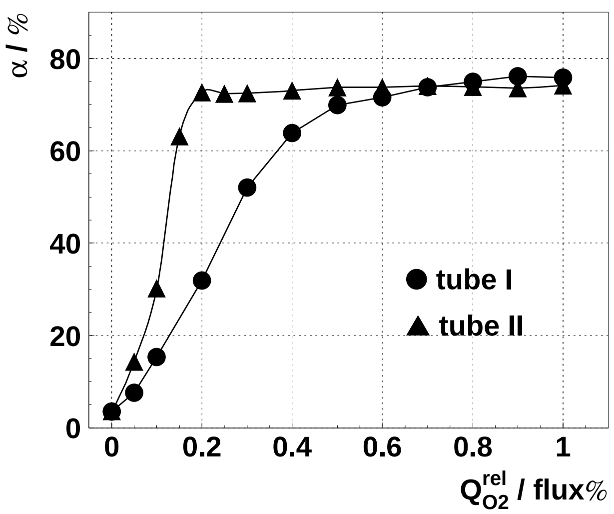

Fig. 7.4: Degree of dissociation α as a function of relative oxygen admixture $Q^{\rm rel}_{\rm O_2}$ for two different discharge tube surfaces: "tube I" denotes a unprepared discharge tube and "tube II" a prepared one with a low recombination coefficient.

From the considerations given in section 4, one can conclude that at least partly the oxygen admixed to the discharge is transformed into water, since it is actually the water layer which reduces the surface recombination rate on the discharge tube. However, it was not clear whether the layer of discharge products freezing on the cold nozzle and leading to a decrease in the ABS intensity with running time consisted only of water or additionally of H_2O_2. Therefore, the composition of the nozzle beam has been analyzed. The studies have been performed for a deuterium beam. The background corrected oxygen and water partial pressure signals $S_{\rm O_2}$ and $S_{\rm D_2O}$ were measured with the lock–in amplifier and recorded by means of the data aquisition system for running and switched off discharge. After reaching steady–state conditions, the running discharge has been switched off and both signals have been recorded for another 30 s. The time dependence of the signals has been recorded for two different nozzle temperatures, where the oxygen admixture was set to about 0.2 flux% in both cases.

Figure 7.5 shows the dependence of $S_{\rm O_2}$ and $S_{\rm D_2O}$ for a nozzle temperature of 220 K. In this case, the adsorption of water on the nozzle surface should be negligible. It is found, that the water signal $S_{\rm D_2O}$ indicated at the left abscissa, has a mean value of about 0.5 in case of the running discharge and drops down to less than 0.01 as soon as the discharge is switched off. The oxygen signal $S_{\rm O_2}$, displayed on the right abscissa, behaves exactly opposite: it has a mean value of about 0.005 in case of the running discharge and increases to 0.5 after the discharge has been switched off. Since no signal on mass 36 corresponding to D_2O_2 could be observed, one can conclude that nearly all of the oxygen admixed is transformed into water. Consequently, the O_2 molecule must have undergone

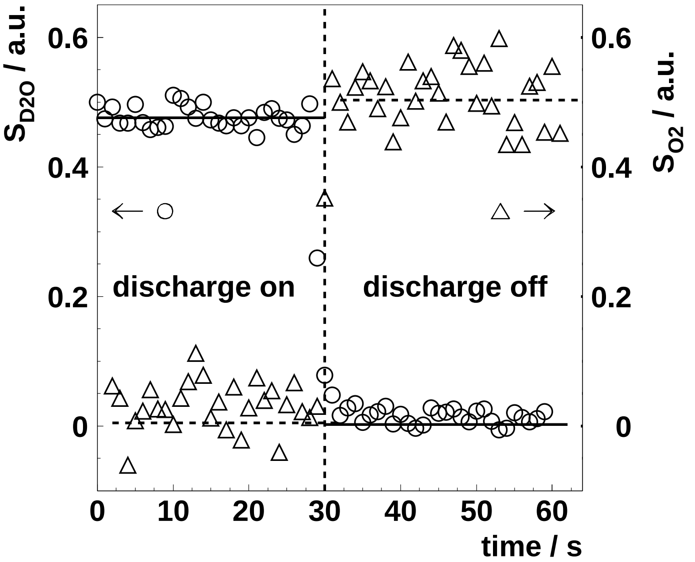

Fig. 7.5: Water and oxygen partial pressures $S_{\mathrm{D_2O}}$ (dots) and $S_{\mathrm{O_2}}$ (triangles) in the beam measured with the QMS with running (time $\leq 30\,\mathrm{s}$) and switched off discharge (time $> 30\,\mathrm{s}$) at a nozzle temperature of $220\,\mathrm{K}$. The continuous and dotted lines denote fits to the $S_{\mathrm{D_2O}}$ and $S_{\mathrm{O_2}}$ data points, respectively.

the following reactions in the deuterium discharge:

$$\text{(i) formation of OD–radicals:} \quad \begin{cases} & \mathrm{e^- + O_2 \rightarrow 2\,O + e^-} \\ & \text{and } \mathrm{O + D_2 \rightarrow D + \underline{OD}} \\ \\ \text{or} & \mathrm{2\,D + O_2 \rightarrow 2\,\underline{OD}} \end{cases}$$

$$\text{(ii) formation of water:} \quad \mathrm{OD + D \rightarrow \underline{D_2O}}$$

Regarding these reactions, both oxygen–driven mechanisms reducing the recombination on the discharge tube surface in the plasma region mentioned in section 4.3 can contribute: the lower adsorption probability of hydrogen or deuterium atoms on a water–covered glass surface or the catalytic dissociation of H_2 or D_2 molecules on the surface by OH or OD radicals.

The measurement was repeated for a cold nozzle at a temperature of 100 K, typical for ABS operation. The result is shown in fig. 7.6. Comparing these data with those obtained for the warm nozzle shows nearly the same evolution of the oxygen partial pressure $S_{\mathrm{O_2}}$ in the beam. However, $S_{\mathrm{D_2O}}$ with running discharge is about a factor of 5 lower compared to the warm nozzle. This indicates, that a substantial fraction of the water produced in the discharge is adsorbed on the surface of the cold nozzle. In summary, the results lead to the following conclusions:

1. In the discharge, the admixed oxygen is nearly completely converted into water.

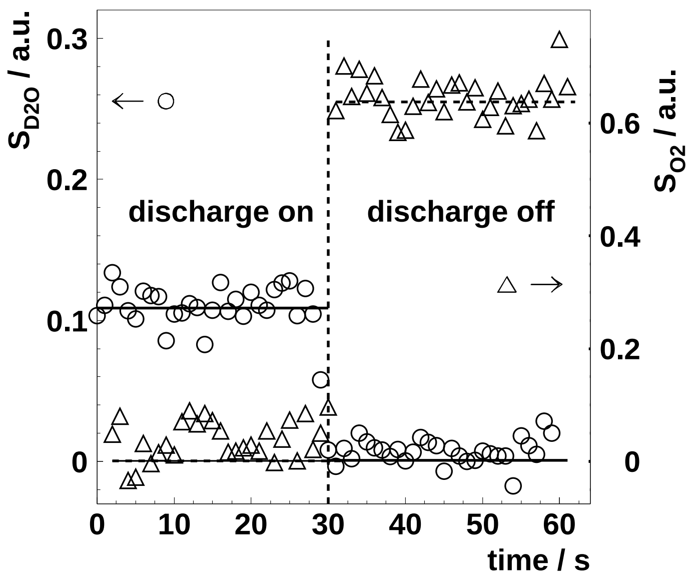

Fig. 7.6: Water and oxygen partial pressures S_{D_2O} (dots) and S_{O_2} (triangles) in the beam measured with the QMS with running (time ≤ 30 s) and switched off discharge (time > 30 s) at a nozzle temperature of 100 K. The continuous and dotted lines denote fits to the S_{D_2O} and S_{O_2} data points, respectively.

2. For typical dissociator nozzle temperatures of about 100 K, a significant amount of the water produced freezes on the cold nozzle surface.

Consequently, the observation of a decrease in ABS output intensity with increasing running time of the discharge mentioned previously (see section 4.3.2), may be caused by an excessive water or ice layer on the nozzle surface. However, since the MWSD has been optimized to yield high degrees of dissociation already at low oxygen admixtures, long–term stable operation is expected at nominal nozzle temperatures around 100 K. This problem is investigated in the next subsection.

7.4 Long–term behaviour

A reliable and stable operation of the MWSD is decisive for the application in the HERMES target source. Therefore, a series of long–term measurements has been performed with the MWSD running in continuous mode. All relevant data have been recorded using the data aquisition system.

As an example, fig. 7.7 shows the degree of dissociation in a hydrogen beam as a function of running time, where the gas throughput has been set to 1.5 mbar l/s, the oxygen admixture to 0.2 flux%, the nozzle temperature to 100 K and the incident microwave power to 480 W. It can be seen, that the degree of dissociation in the beam stays nearly constant and decreases only slightly from about 80 % to 75 % during a continuous running time of six days.

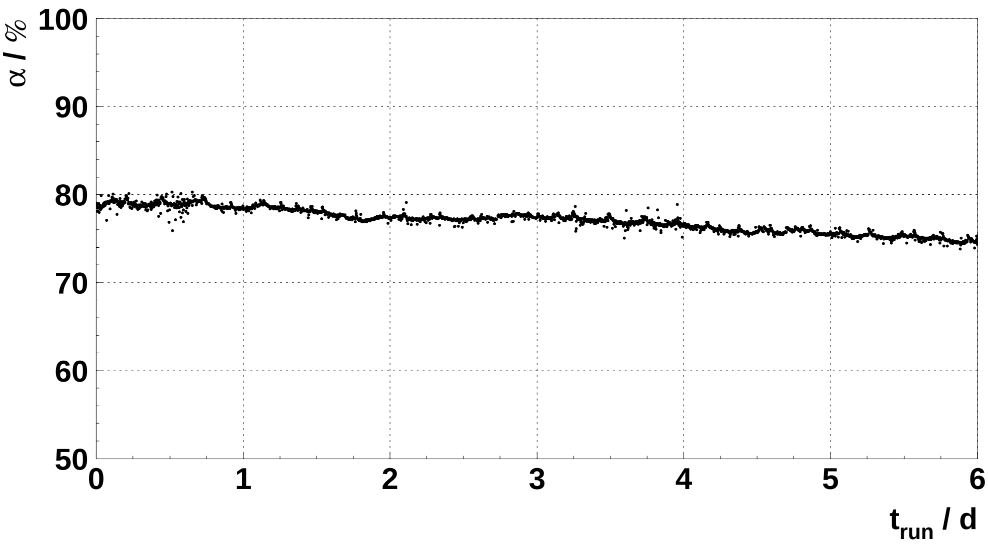

Fig. 7.7: Degree of dissociation α as a function of continuous running time t_{run} with a low oxygen admixture of $0.2\,\text{flux\%}$ under typical running conditions for the HERMES–ABS.

After regenerating the nozzle, the initial high value of $\alpha = 80 \ldots 85\,\%$ could always be reproduced. Comparing this long–term stable behaviour with the short running times reported for a surface wave dissociator developed at CERN [116, 117, 118] and with the experience at the CERN set–up made in the course of this thesis, the running times obtained with the MWSD are a factor of 7 up to 30 higher.

In order to analyze the discharge products frozen onto the nozzle during continuous operation, the composition of the nozzle beam evaporating from the inner nozzle surface has been determined warming up the nozzle after a longterm–measurement. No partial pressure signals apart from that of water could be observed. As shown in fig. 7.8, the water signal $S_{\mathrm{H_2O}}$ from the nozzle beam and the pressure in the discharge tube p_{dt} have been recorded as a function of warming up time t_{warmup}. Both p_{dt} and $S_{\mathrm{H_2O}}$ show a quite similar evolution with t_{warmup}. A rise in the discharge tube pressure can only arise from evaporation of discharge products frozen on the cold nozzle during dissociator operation. Since the water signal in the beam is very similar to the evolution of p_{dt}, one can conclude that only water is frozen on the nozzle, confirming the results from the previous subsection.

In order to verify the negative effect of a high oxygen admixture, a long–term measurement has been performed using the same parameters as for the measurement shown in fig. 7.7 except that the oxygen admixture has been set to $Q^{\mathrm{rel}}_{\mathrm{O_2}} = 2.5\,\text{flux\%}$. The degree of dissociation and the pressure in the discharge tube have been measured as a function of continuous running time. As shown in fig. 7.9, the atomic fraction in the nozzle beam

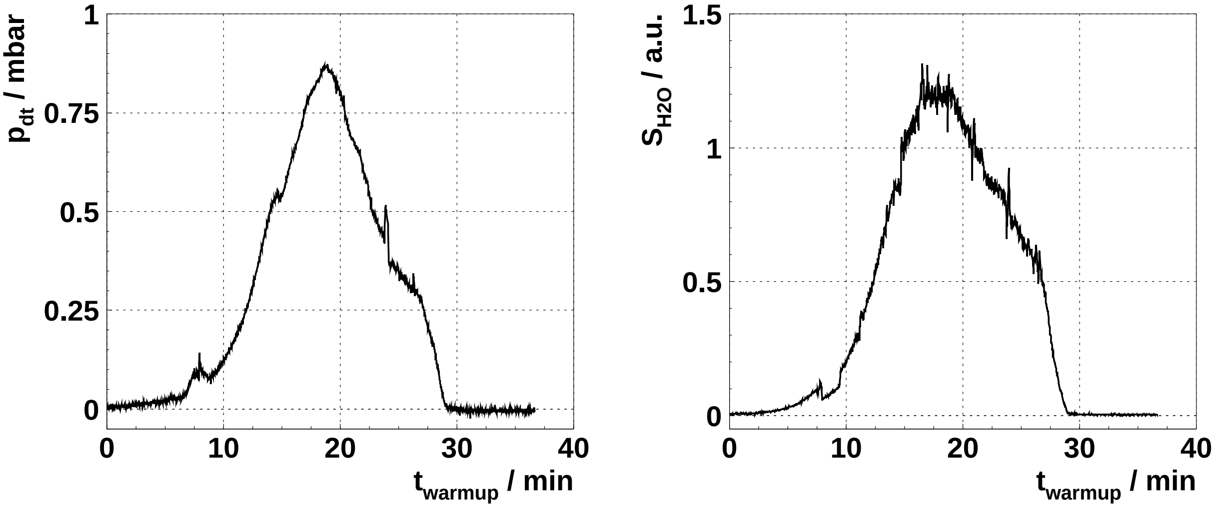

Fig. 7.8: Pressure in the discharge tube p_{dt} (left plot) and water partial pressure signal from the beam out of the nozzle detected by the QMS $S_{\mathrm{H_2O}}$ (right plot) as a function of warming up time t_{warmup} during a nozzle regeneration cycle.

starts to drop already after a short running time of 1 h. Within the first ten hours of operation, α decreases from 80 % to 70 % and afterwards even more steep below 40 % at $t_{\mathrm{run}} = 20$ h. At the same time, the discharge tube pressure rises strongly from initially 0.9 mbar to 2 mbar after a running time of 20 h. The rise in p_{dt} is a result of water accumulating on the nozzle in macroscopic quantities which effectively reduces the conductance of the nozzle. As a consequence, the pressure in the discharge tube rises, since the gas throughput is kept constant. It is important to mention, that in parallel to the rise of p_{dt}, the heater current needed to stabilize the nozzle temperature at 100 K dropped continuously from initially about 5.2 A to less than 3.5 A. This indicates a dramatic rise of the heating power deposited on the nozzle due to surface recombination.

In summary, it has been shown that the oxygen admixture needed to obtain a high degree of dissociation in the discharge, is predominantly transformed into water. At the typical gas pressures and nozzle temperatures, water freezes on the nozzle and forms a macroscopic layer. This layer seems to enhance surface recombination once a critical thickness is exceeded. Consequently, long–term stable operation with high atomic fractions in the beam can only be obtained by minimizing of the necessary oxygen admixture.

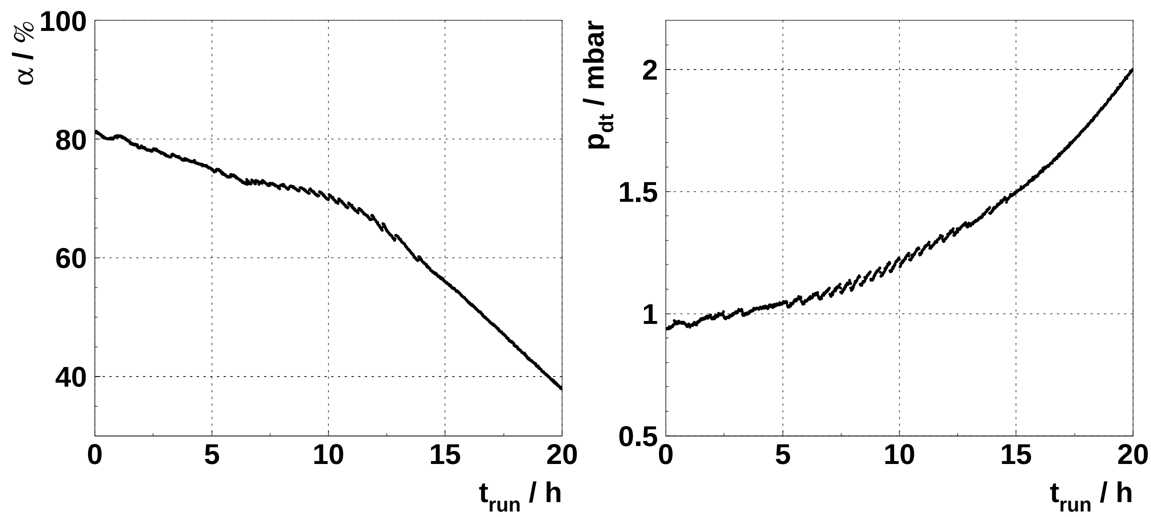

Fig. 7.9: Degree of dissociation α and pressure in the discharge tube p_{dt} as a function of continuous running time t_{run} with a high oxygen admixture of $2.5\,\mathrm{flux}\%$ under the same running conditions as for the measurement shown in fig. 7.7.

7.5 Investigation of recombination losses on the nozzle

Throughout the previous studies, the influence of the plasma source parameters on the degree of dissociation has been investigated. For all measurements presented, an aluminum nozzle made of Al 99.5 has been used, which had been found to provide the best recombination properties in the course of earlier studies [41].
In this section, investigations of the atomic losses on various nozzle surfaces are presented. The degree of dissociation in the nozzle beam has been measured in a temperature range of $T_{\mathrm{nz}} = 45\ldots310\,\mathrm{K}$ for the following nozzle surfaces:

- Silicone–coated aluminum and copper nozzles.
- an anodized aluminum (purity 99.5 %) nozzle.
- a quartz–coated aluminum nozzle,
- a bare copper nozzle.

Silicone and Al_2O_3 should strongly inhibit wall recombination [120, 121]. According to ref. [119], a quartz surface is superior compared to Silicone. In contrast, bare copper exhibits a high recombination rate. The various nozzle surfaces were prepared and coated as described in Appendix F.

The nozzles investigated had a cylindrical shape as shown in fig. 7.5, in order to provide high thermal conductivity also at the nozzle tip. This design is expected to yield a homogenious temperature distribution on the inner nozzle surface. The experimental

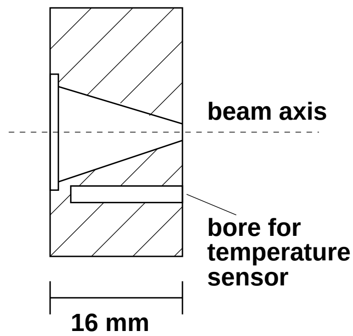

Fig. 7.10: Scale drawing of the nozzles used for the surface recombination studies. The cylindrical shape provides high thermal conductivity and hence a homogenious temperature distribution on the inner nozzle surface.

conditions have been chosen such, that surface recombination on the nozzle is the dominant atomic loss factor. The gas throughput was set to 1 mbar l/s corresponding to a discharge tube pressure between 0.5 mbar and 0.7 mbar. It had been verified experimentally in section 4.3 and 7.2, that in this range of gas parameters both volume and surface recombination losses in the afterglow are negligible. In order to provide a sufficiently high atomic fraction in the discharge, the incident microwave power was chosen to 450 W for hydrogen and 300 W for deuterium. The distance d_{pn} between plasma end and nozzle entrance has been set to a constant value of 45 mm. The position of the plasma end could be observed by means of the side window mounted at the dissociator chamber. Since the gas pressure and hence the discharge length changes with changing nozzle temperature as a result of the temperature dependence of the nozzle conductance, the MWS has been slided over the discharge tube on its linear motion bearing in order to keep d_{pn} constant.

During a measurement cycle, the nozzle has been cooled down to the minimum achievable temperature of about 45 K in steps of 10 K ("scan–down"), and α has been measured for each temperature step about 5 min after the nozzle temperature had been stabilized. In order to study eventual hysteresis effects, the degree of dissociation measurement has been repeated in the same way, whilst the nozzle was warmed up from 45 K to 300 K ("scan–up").
A comparison of the α values for the various nozzle surfaces during a scan–down measurement is shown in fig. 7.11.
It is found, that all curves show the same shape and differ only slightly in α in case of nozzle temperatures below 200 K. A more or less flat top at $\alpha \approx 80\,\%$ is reached in the temperature range between 100 K and 200 K. For temperatures below 100 K, the atomic fraction decreases with decreasing nozzle temperature in the same way for all surfaces under study. A quite pronounced evolution of α is observed in case of the bare copper nozzle. The atomic fraction is close to zero for nozzle temperatures above 220 K and increases

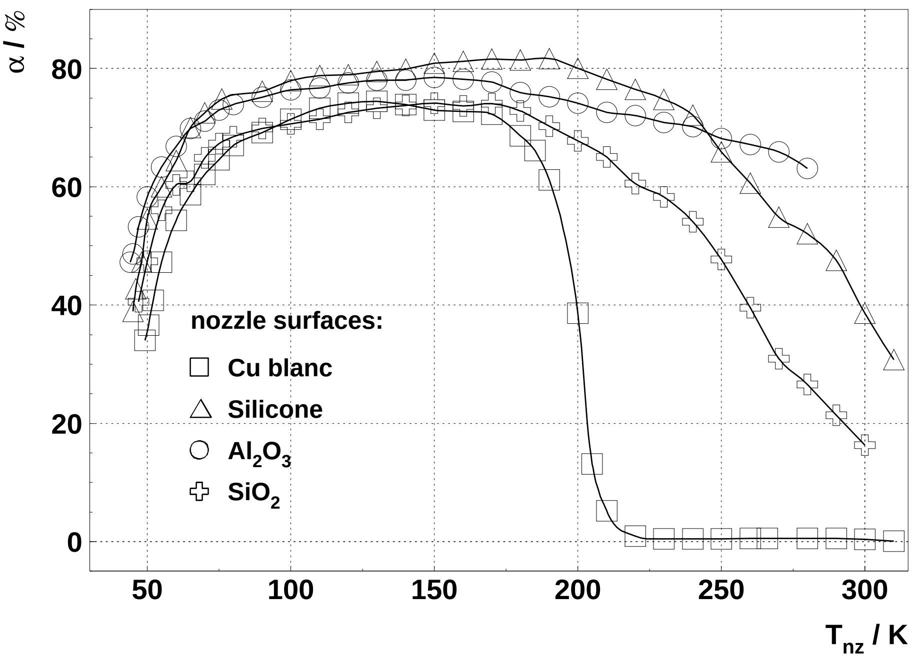

Fig. 7.11: Degree of dissociation α as a function of nozzle temperature T_{nz} for various nozzle surfaces durin a "scan–down" measurement (for explanation see text).

quickly for lower temperatures, where it adapts to the other curves. This behaviour cannot be explained by the temperature dependence of the copper surface recombination coefficient [122, 123], since in this case a maximum in the atomic fraction at a nozzle temperature of about 40 K is predicted.

The recombination properties of the bare copper nozzle have been investigated in more detail performing additionally a scan–up measurement. Figure 7.12 shows the comparison of the scan–down and the scan–up measurement for the bare copper nozzle. When the bare copper nozzle is warmed up, it is found that the atomic fraction breaks down to zero exactly at that temperature, where the water adsorbed on the nozzle evaporates. The evaporation of water at $T_{\mathrm{nz}} \approx 230\,\mathrm{K}$ has been verified in a second measurement where the water partial pressure in the nozzle beam and the pressure in the dissociator chamber have been observed.
From the results above one can conclude, that it is actually the water layer adsorbed on the cold nozzle surface, which determines the wall recombination properties in the nozzle.

Finally, the surface recombination properties of hydrogen and deuterium have been compared. The results of a scan–down measurement for both gases using a Silicone coated copper nozzle are shown in fig. 7.13. It can be seen, that α behaves in exactly the same

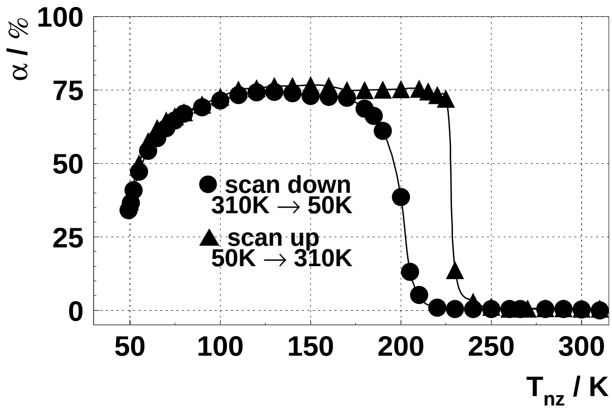

Fig. 7.12: Degree of dissociation α as a function of nozzle temperature T_{nz} for a scan–down and a scan–up measurement showing the hysteresis behaviour.

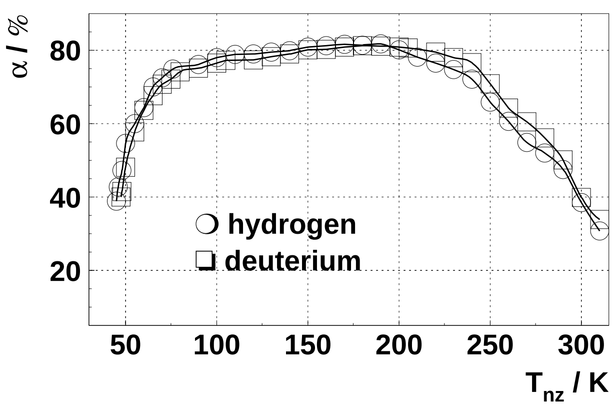

Fig. 7.13: Comparison of the degree of dissociation α as a function of nozzle temperature T_{nz} for hydrogen and deuterium for a scan–down–measurement.

way within the systematic uncertainties for both hydrogen and deuterium. Taking into account eqs. (3.35) and (4.12), and this results in an about 1.4 times higher recombination coefficient in case of deuterium compared to that of hydrogen in the entire temperature range investigated.

In summary, individual recombination properties of the various nozzle surfaces are suppressed to a large extend by the adsorbed water layer in the relevant temperature range typical for dissociator operation. Only for nozzle temperatures exceeding a value of about 220 K, one could benefit from the lower recombiation coefficient of an Al_2O_3 or a silicone layer. A substantial increase of the atomic fraction in the beam using a nozzle with a SiO_2 surface as reported in ref. [119] could not be observed.

7.6 Comparison with the radio frequency dissociator

The general design criteria of the radio frequency dissociator (RFD) are described in previous works [55, 41]. The latest modifications concerned the nozzle cooling system and are documented in ref. [43]. The main difference with respect to the MWSD is the plasma source sustaining the discharge via resonant coupling of the applied electromagnetic high frequency field. As mentioned in section 2.2, the RFD field applicator consists of an oscillating LC–circuit tuned resonant to 13.56 MHz by means of an impedance matching network. The discharge tube has an inner diameter of 11 mm and is surrounded by a water cooling jacket.
In comparison to the results obtained with the RFD in the course of former studies [41, 49, 50, 42], the MWSD yields atomic fractions in the nozzle beam which are a factor of 1.2 to 2 higher. In order to obtain a direct comparison of the performance of both dissociators, the RFD has been mounted at the ABT for a short period during the 1997/1998 shutdown of the HERMES–experiment.

The degree of dissociation achieved with the RFD has been measured for both hydrogen and deuterium as a function of incident radio frequency power for various gas throughputs. In analogy to similar studies with the MWSD, the nozzle temperature was set to 100 K, and the oxygen admixture was about 0.1 flux % in order to minimize the surface recombination losses.

Fig. 7.14 shows the results obtained for hydrogen. The atomic fraction rises with

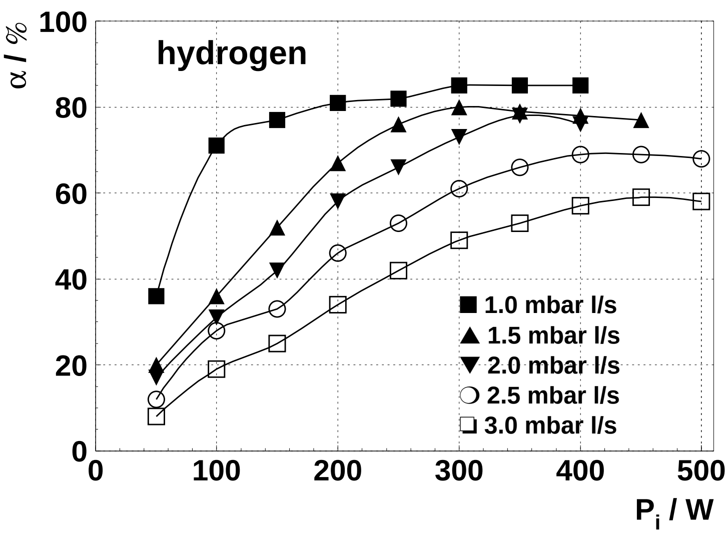

Fig. 7.14: Degree of dissociation α as a function of incident radio frequency power P_{i} for various hydrogen throughputs Q_{m} ranging from 1 mbar l/s to 3 mbar l/s.

increasing radio frequency power and decreasing gas throughput. For throughput levels below 2 mbar l/s, high degrees of dissociation are obtained ranging from 74 % up to 85 %. It is found, that an increase of Q_{m} to values beyond 2 mbar l/s leads to a significant decrease in α below 60 % at $Q_{\mathrm{m}} = 3\,\mathrm{mbar\,l/s}$. For all throughput levels investigated, the atomic fraction saturates and even slightly decreases in case the power exceeds the saturation value. Moreover it has been observed, that the discharge burns slightly out of the nozzle for power levels exceeding about 250 W. A sort of change in the plasma mode occured in case of gas throughputs and incident radio frequency powers of more than 1.5 mbar l/s and 350 W, where the plasma has been observed to burn out of the nozzle with a jet like shape. At the same time, the heating power stabilizing the nozzle temperature decreased strongly, and for throughput and power levels exceeding 2 mbar l/s and 400 W, respectively, the cooling power was not sufficient to keep the nozzle at 100 K. Coincident with the appearence of the plasma jet, the discharge tube pressure steeply increased by a factor of about 1.3, which indicates a strong heating of the nozzle tip resulting in a decreased conductance.

Finally, the dissociation efficiency of the RFD for deuterium has been investigated. The dependence of the atomic fraction in the nozzle beam on the incident radio frequency power and the gas throughput is shown in fig. 7.15. It is found, that the degree of

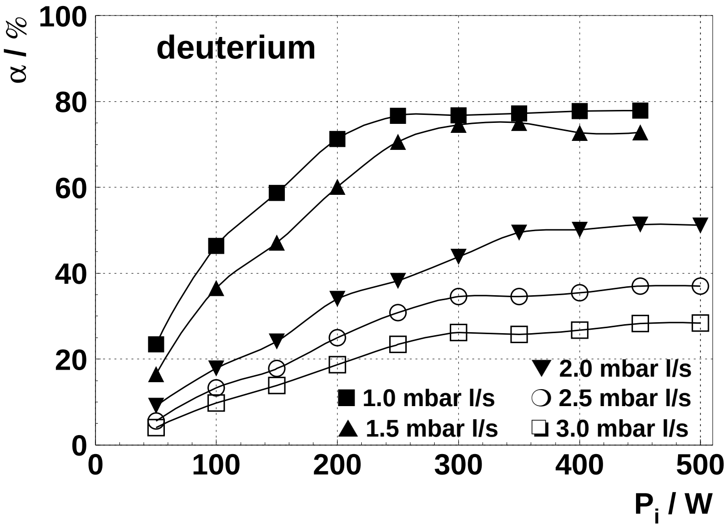

Fig. 7.15: Dependence of the degree of dissociation α on the incident radio frequency power P_{i} for various deuterium throughput levels Q_{m} ranging from 1 mbar l/s to 3 mbar l/s.

dissociation in general rises with increasing radio frequency power, however the decrease in α for increasing gas throughputs is more pronounced than in the case of hydrogen. The obtained maximum α values range between 78 % at a gas flow of 1 mbar l/s and 30 % at 3 mbar l/s. The formation of the plasma jet has been observed to occur for all throughput levels investigated provided the incident radio frequency power exceeded 300 W.

In summary, it is found for both hydrogen and deuterium, that an increase in incident radio frequency power does not yield a higher degree of dissociation, once α reached its saturation value. Atomic losses in the afterglow cannot explain this behaviour, since for higher power levels the discharge burns even out of the nozzle. Consequently, the degree of dissociation in the nozzle beam should be approximately the same as the atomic fraction in the plasma. Therefore, the strong decrease in the degree of dissociation at high gas throughputs can only be explained by a low atomic fraction in the discharge region itself caused by gas flow and volume recombination induced atomic losses. The latter loss mechanism is assumed to be responsible for the more steep decrease of α with increasing gas throughput observed for deuterium.

Regarding the discharge model from section 3, an increase in the degree of dissociation in the plasma with increasing power density is predicted, provided the recombination losses on the discharge tube surface are kept on a reasonably low level. This should be the case, since the discharge tube is water cooled and the surface prepared according to the standard procedure. Therefore one can conclude in case of the RFD, that an increase of the incident radio frequency power does not yield an increase in power density sufficient to dissociate high gas throughputs. This may be due to a reflection of the applied radio frequency at the plasma surface, if a certain electron density is exceeded, which is a typical drawback of resonantly sustained discharges (see also section 4).

The observed plasma jet, occurring for sufficiently high gas densities and radio frequency powers, is a typical example for a mode change observed for resonantly coupled discharges, as had been pointed out in section 4. As a result, the nozzle tip has been strongly heated up. The measurements of the velocity distribution and the ABS intensity given in refs. [50, 42] under similar conditions imply, that in case of the appearence of the plasma jet, the beam temperature is increased by up to a factor of 5 and the output intensity dropped by a factor of more than 2, resulting from a decreased transmission of the sixpole system.

In fig. 7.16, the throughput dependence of the degree of dissociation in the hydrogen and deuterium beam is shown for both dissociators. The data points obtained with the RFD are summarized from the measurements above, and the MWSD results are taken from fig. 7.3. It is found, that the new MWSD is clearly superior to the conventional RFD, especially for deuterium and in the range of high gas throughputs. This is caused by a higher power density in the discharge resulting from the different mechanisms involved to sustain the discharge. In contrast to a standing surface wave discharge, the power density of which can be steadily increased by increasing the incident high frequency power, the results obtained with the RFD indicate a saturation in the achievable power density.

7.7 Summary

The MWS based dissociator has been investigated over the whole range of parameters relevant for the application within a polarized atomic beam source.

For the degrees of dissociation in the nozzle beam, up to 90 % for throughputs around 1 mbar l/s have been obtained for both hydrogen and deuterium. Even for gas flows as high as 5 mbar l/s, the atomic fraction is still above 70 %. The high power densities

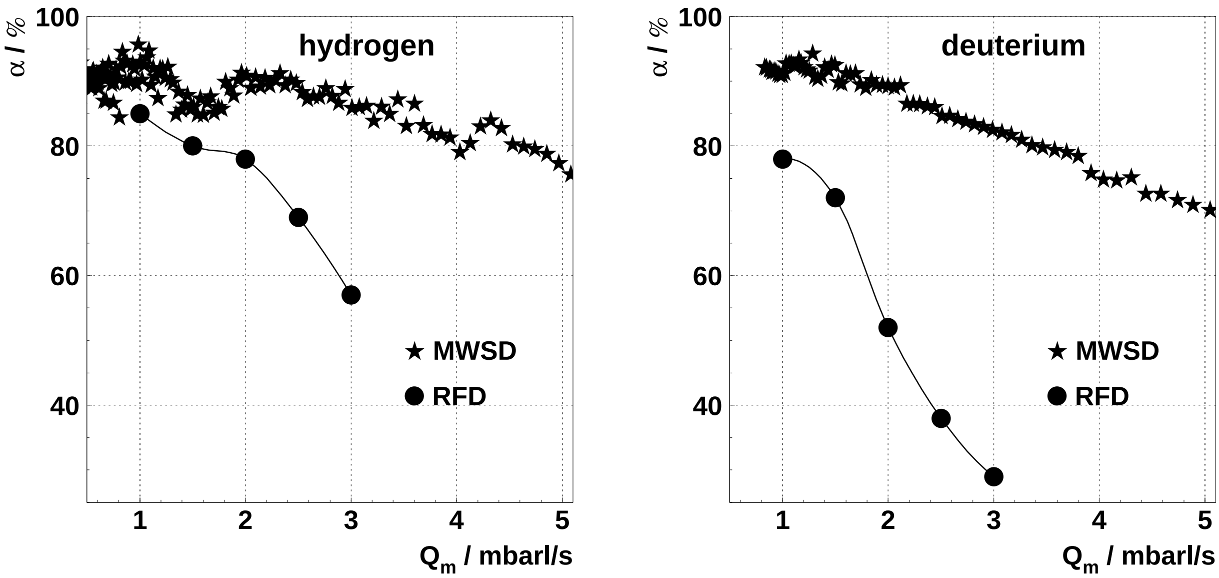

Fig. 7.16: Dependence of the degree of dissociation α on the gas throughput Q_{m} for the RFD (dots) and the final version of the MWSD (stars). The achievable atomic fractions in a hydrogen and a deuterium beam are shown in the left and the right graph, respectively.

close to the nozzle entrance, which are especially needed to efficiently dissociate high gas throughputs, are achieved by means of a standing wave discharge, where the surface wave is reflected at the downstream end of the discharge tube. This mechanism has already been disclosed in the course of the test bench studies presented in section 4.3. The final version of the MWSD with a minimized distance between coupling slit and nozzle entrance yielded mean power densities of up to $70\,\mathrm{W/cm^3}$.

It has been found, that only a low oxygen admixture of about $0.1\ldots0.2$flux% is needed to obtain a maximum degree of dissociation, owing to the test bench optimization of the MWS based plasma source. Moreover, it could be verified that the oxygen admixed to the hydrogen or deuterium discharge is nearly exclusively transformed into water, and that the water produced is adsorbed on the nozzle surface for temperatures below 200 K.

As a consequence of the low oxygen admixture, long running times without the need of nozzle regeneration are expected. This expectation has been verified in the course of a series of long–term measurements. Under the running conditions of the HERMES–ABS, a stable atomic fraction in the beam in the order of 80 % has been obtained for typical continuous running times of six days. Moreover, a high oxygen admixture could be clearly identified to be the cause for a reduction in long–term stability, since the resulting excessive ice layer on the nozzle enhances surface recombination.

The recombination properties of various nozzle surfaces have been investigated for a large temperature range. It has been found, that the adsorbed water layer dominates the individual recombination properties of the surfaces under study. Consequently, nozzle coating procedures are dispensable, in case the operational temperatures are below 200 K.

Since the water layer exhibits a rather low recombination coefficient, which is also reported in ref. [124], the increased surface recombination losses observed for excessive water layers may be explained by the formation of ice or irregular surface structures. This results in a sort of cryo trapping of the atoms and hence an extended dwell time on the surface increasing the recombination probability.

Comparative measurements with the radio frequency dissociator of the HERMES–ABS have been performed. The MWSD has been found to yield higher degrees of dissociation for higher gas throughputs especially with respect to the production of an atomic deuterium beam. This is a result of the higher power densities in the discharge obtained with the MWS based plasma source.

It should be mentioned, that the output flow rate provided by the HERMES–ABS saturates at throughputs below 1.5 mbar l/s, which can be traced back to substantial attenuation losses of the atomic beam. At this low gas throughput, both dissociator types show nearly equal performance. Therefore, in order to benefit from the high dissociation efficiency provided by the MWSD at high gas throughputs, the attenuation mechanisms have to be understood quantitatively and suppressed as far as possible. This problem is investigated in detail in the following section.

8 Beam Attenuation Studies

8.1 Overview

From the considerations on the ABS output intensity $\Phi_{\bar{a}}^{\text{cell}}$ in section 2.3 and from the degree of dissociation measurements with the radio frequency dissociator given in the previous section, one can conclude that the saturation of the HERMES–ABS intensity already at moderate gas throughputs around $1 \ldots 1.5\,\text{mbar l/s}$ is not caused by a limited atomic flow out of the nozzle, but by a strong increase in beam attenuation losses with increasing gas throughput. On the other hand, the new MWSD has shown a high dissociation efficiency also at high gas throughput levels (see section 7.3). Therefore, the ABS output intensity will benefit from the MWSD development only, if the mechanisms attenuating the beam can be understood quantitatively. According to eq. (2.11), which describes the ABS output intensity injected into the entrance tube of the storage cell, the total attenuation factor is composed of the factors S_{RGA} and S_{IBS} denoting rest gas and intra–beam scattering induced beam losses. In both cases, a hard sphere potential and single scattering losses are assumed. Since it has been shown, that IBS losses are negligible for the typical flow conditions in the beam [54], the studies presented below are restricted to a detailed investigation of the RGA induced beam losses.

All measurements shown in the following have been performed for molecular and atomic beams in the absence of sixpole magnets using the atomic beam teststand. The flow rate of an unfocussed molecular or atomic beam into the ABT compression tube can be written as

$$\Phi_{\text{m,a}}^{\text{ct}} = Q_{\text{m,a}} \left(1 - \cos^{n+1} \vartheta_{\text{ct}}\right) S_{\text{RGA}} , \tag{8.1}$$

where $Q_{\text{m,a}}$ is the molecular or atomic flow rate out of the nozzle, $Q_{\text{a}} = Q_{\text{m}}\, 2\,\alpha$, ϑ_{ct} is the opening angle of the compression tube and n is the peaking exponent.
The attenuation factor is given as

$$S_{\text{RGA}} = \exp\left[-\frac{1}{k\,T_{\text{rg}}} \sum_{i=1}^{4} \left(\sigma_{\text{rg}}^{\text{eff}}\, l\, p\right)_i\right] , \tag{8.2}$$

where $T_{\text{rg}} = 300\,\text{K}$ is the rest gas temperature and $\left(\sigma_{\text{rg}}^{\text{eff}}\, l\, p\right)_i$, $i = 1 \ldots 4$, is the product of effective single scattering loss cross section, attenuation length and rest gas pressure on the beam axis for each of the four ABT chambers.

As a first step towards the determination of S_{RGA}, the effective single scattering loss cross section has been measured (section 8.2). Owing to the flexible geometry of the atomic beam test stand, the restricted pumping conductance in the nozzle–skimmer and skimmer–collimator region of the HERMES–ABS could be simulated experimentally, which allowed to measure the actual rest gas pressure in the vicinity of the beam (section 8.3). In section 8.4, a quantitative estimate of the peaking exponent is given based on the intensity description from eq. (8.1), and the throughput dependence of the beam intensity into the compression tube is calculated and compared with the measured data in section 8.5. The RGA losses occuring within the HERMES–ABS are estimated in section 8.6. In section 8.7, the results obtained for the rest gas attenuation studies are summarized.

The studies presented below are partially published in ref. [125].

8.2 Measurement of the effective single scattering loss cross sections

Regarding the standard geometry of the ABT skimmer chamber (see Appendix E), one can assume an unrestricted pumping conductance in the vicinity of the beam and hence a homogenious rest gas distribution. Consequently, the pressure read out by means of the ionization gauges at the circumference of the skimmer chamber should be the same as the rest gas pressure in the beam region. Injecting additional rest gas into the skimmer chamber from the side gas inlet, the increased rest gas pressure will result in a decreased beam intensity detected by the compression tube or the mass spectrometer. Considering eqs. (8.1) and (8.2), the effective single scattering loss cross section can be derived from the ratio of attenuated to initial intensity as

$$\sigma_{\mathrm{rg}}^{\mathrm{eff}} = \frac{k\,T_{\mathrm{rg}}}{d_{\text{sk-col}}} \left(\frac{\Delta \ln \Phi_{\mathrm{m}}^{\mathrm{ct}}}{\Delta p_{\text{sk-ch}}} \right) , \tag{8.3}$$

where $d_{\text{sk-col}}$ is skimmer–collimator distance equal to the attenuation length in the skimmer chamber, $\Delta p_{\text{sk-ch}}$ is the difference between the initial pressure and the pressure caused by the rest gas inlet and $\Delta \ln \Phi_{\mathrm{m}}^{\mathrm{ct}}$ is the logarithm of the ratio between attenuated and initial intensity.
Since an exponential decrease in the intensity is expected in case of single scattering losses, $\sigma_{\mathrm{rg}}^{\mathrm{eff}}$ can be determined from the slope of the logarithmicly plotted intensity as a function of the pressure in the skimmer chamber.

The main systematic uncertainty in the cross section measurement arises from the determination of the absolute pressure in the attenuation chamber. For the ion gauges used at the ABT, the producer gives an uncertainty of 10 % of the measured value. Moreover it has been found, that the distribution of the residual gas injected from the side inlet is not homogenious. This was recognized comparing the effective pumping speed in the skimmer chamber, derived from the nominal pumping speed of the turbomolecular pumps and the conductance of the tubing to the chamber, with the pumping speeds determined from the pressure rise caused by the side gas inlet. Therefore, as shown in fig. 8.1, the rest gas inlet is designed in order simulate the rest gas distribution as arising from the beam particles hitting the aperture to the next chamber. H_2 or D_2 from the calibrated gas inlet system is injected by a tube onto the separation wall on which the collimator is placed. The inlet into the dissociator chamber is illustrated as well. This type of gas inlet is realized in each of the first three pumping stages. A comparison of the effective

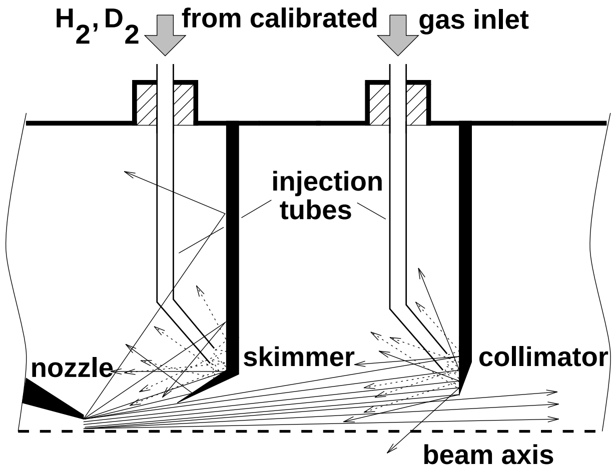

Fig. 8.1: Scheme of the rest gas side inlet at the skimmer chamber and the dissociator chamber. The solid and dotted lines represent the trajectories from the gas particles emitted by the nozzle and those injected by the tubes, respectively.

pumping speeds with the pumping speed derived from ion gauge calibrations using the side gas inlet with the injection tube shows a deviation of less than 5 %.

A typical measurement of the effective cross section of molecular hydrogen is shown in fig. 8.2 for a nozzle temperature of 100 K and a gas throughput of 1.5 mbar l/s. The

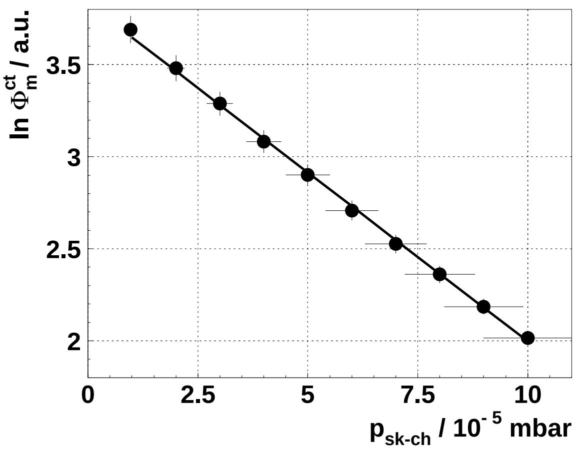

Fig. 8.2: Logarithm of the molecular hydrogen intensity $\Phi_{\mathrm{m}}^{\mathrm{ct}}$ measured with the compression tube as a function of H_2 rest gas pressure $p_{\mathsf{sk\text{-}ch}}$ in the skimmer chamber for a nozzle temperature of 100 K. The line represents a linear fit to the data.

resulting cross section is $1.05 \times 10^{-14}\,\mathrm{cm}^2$. The linear evolution of $\ln \Phi_{\mathrm{m}}^{\mathrm{ct}}$ proves, that the beam attenuation actually is caused by single scattering losses. It is important to mention, that for the determination of the cross sections, the signal measured with the intensity detector has always been corrected for the effusive contribution from the skimmer chamber.

8.2.1 Dependence on the nozzle temperature

The dependence of the effective single scattering loss cross section $\sigma_{\mathrm{rg}}^{\mathrm{eff}}$ on the nozzle temperature has been studied as a function of nozzle temperature for a standard ABS gas throughput of 1.5 mbar l/s. The scattering losses have been investigated for both atomic and molecular hydrogen and deuterium.

In fig. 8.3, $\sigma_{\mathrm{rg}}^{\mathrm{eff}}$ is shown for hydrogen and deuterium atoms and molecules and for the discharge switched on and off. In general it is found, that the effective atomic and molec-

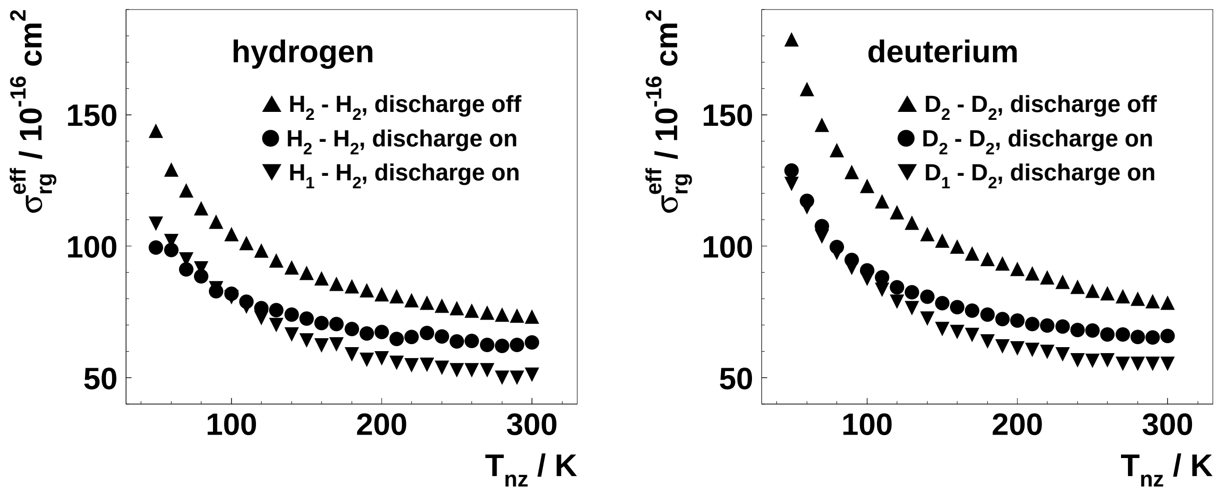

Fig. 8.3: Effective single scattering loss cross sections $\sigma_{\mathrm{rg}}^{\mathrm{eff}}$ for both hydrogen and deuterium as function of nozzle temperature T_{nz}. The full triangels, squares and dots denote the cross sections for $x_2 - x_2$ scattering with running and switched off discharge and for $x_1 - x_2$ ($x =$ H, D) scattering with running discharge, respectively.

ular loss cross section rises for a decreasing nozzle temperature. Since the mean velocity of the beam has been measured to rise nearly linearly with the nozzle temperature [50], this behaviour indicates a velocity dependence of $\sigma_{\mathrm{rg}}^{\mathrm{eff}}$. The increase of $\sigma_{\mathrm{rg}}^{\mathrm{eff}}$ with decreasing nozzle temperature results in a stronger RGA induced beam attenuation and may hence explain the saturation in the output intensity at lower gas throughputs for lower nozzle temperatures observed for an undissociated beam [41, 127].

As shown in the left graph of fig. 8.3, the cross section for H_2–H_2 scattering is a factor of 1.15 . . . 1.45 higher in case the discharge is switched off compared to the value with running discharge. Hence it can be concluded, that the velocity of the molecules in the nozzle beam with running discharge is higher than the one with discharge switched off. This could be caused by the high gas temperatures in the MWS discharge close to the nozzle entrance, which might affect the cooling of the beam [126]. A more precise picture on the velocity dependence of $\sigma_{\rm rg}^{\rm eff}$ will be given in the future after finalizing the TOF studies which are currently performed [112]. Comparing the loss cross sections for H_2–H_2 and H_1–H_2 scattering with running discharge reveals very similar values for nozzle temperatures in the range between 80 K and 120 K. For lower temperatures, the atomic cross section becomes slightly higher, at most by about 10 % compared to the molecular one. For higher nozzle temperatures, the atomic loss cross section decreases stronger than the molecular one and is around 1.2 times lower for $T_{\rm nz} = 300\,{\rm K}$. Hence, in a partially dissociated beam, the molecules will be attenuated stronger than the atoms for nozzle temperatures above 110 K. It is important to note, that this effect requires no corrections of the degree of dissociation measurements presented in section 7, since for the investigations done in this range of nozzle temperatures, the gas throughput and hence the integrated pressure was too low to cause significant attenuation.

The effective loss cross sections for deuterium are shown in the right graph of fig. 8.3. Comparing the evolution of the atomic and molecular cross sections for running and switched off discharge, the situation is very similar to what has been observed for hydrogen. However, the cross sections for deuterium are in general higher by a factor of about 1.2 … 1.3 at lower and 1.05 … 1.15 at higher nozzle temperatures. This may be one reason for the fact that the output intensity of AB sources measured for deuterium is below that obtained for a hydrogen beam [129, 23].

8.2.2 Dependence on the gas throughput

Regarding the nozzle temperature dependence and thus the implicit velocity dependence of $\sigma_{\rm rg}^{\rm eff}$, a dependence on the gas throughput may be expected, since this affects the beam velocity as well. Due to the small opening angles of the intensity detectors used (compression tube: 0.25°, QMS: 0.075°), single scattering losses will reduce the intensity into the compression tube only, if the residual gas molecules penetrate into the center of the beam. Therefore, one might additionally expect a sort of shielding effect towards residual gas attenuation in the nozzle–skimmer region especially at higher gas throughputs, since the gas density in the beam behind the nozzle is still relatively high and thus the mean free path of the rest gas molecules penetrating into the beam accordingly low. In order to verify this effect, the effective loss cross section has been measured in the dissociator chamber and the skimmer chamber, where the beam density is expected to be too low to cause a shielding effect.

In case of the cross section measurement in the dissociator chamber, the nozzle–skimmer distance has been set to the maximum of 78 mm to avoid pressure bumps in the nozzle–skimmer region. The rest gas has been injected with a tube as shown in fig. 8.1. Figure 8.4 shows the dependence of $\sigma_{\rm rg}^{\rm eff}$ for a molecular hydrogen and deuterium beam on the nozzle throughput $Q_{\rm m}$. The nozzle temperature has been set to the standard value of 100 K. From the left graph measured for hydrogen, it can be seen that $\sigma_{\rm rg}^{\rm eff}$ decreases strongly with decreasing throughput between 1 mbar l/s and 0.25 mbar l/s. For

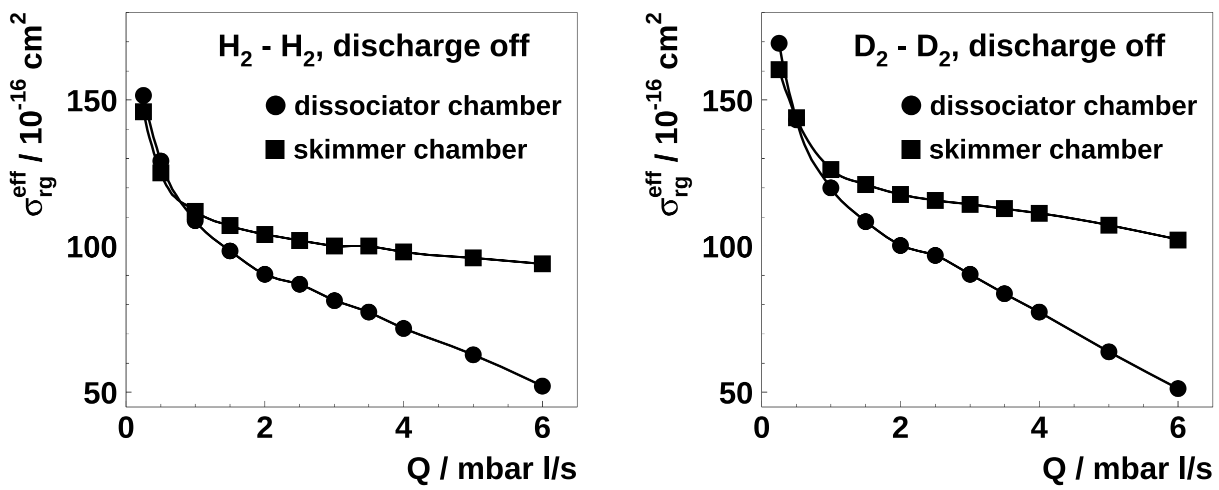

Fig. 8.4: Dependence of the single scattering loss cross sections $\sigma_{\mathrm{rg}}^{\mathrm{eff}}$ for both hydrogen and deuterium molecules on the gas throughput Q_{m} for the standard nozzle temperature of 100 K. The squares and dots denote the values obtained attenuating the beam in the skimmer and the dissociator chamber, respectively.

$Q_{\mathrm{m}} > 1\,\mathrm{mbar\,l/s}$, the beam attenuated in the skimmer chamber shows only a slight, nearly linear decrease with increasing throughput, resulting in a change from $\sigma_{\mathrm{rg}}^{\mathrm{eff}} \approx 1.1 \times 10^{-14}\,\mathrm{cm}^2$ at $1\,\mathrm{mbar\,l/s}$ down to $0.95 \times 10^{-14}\,\mathrm{cm}^2$ at $6\,\mathrm{mbar\,l/s}$. The effective loss cross sections measured in the dissociator chamber have the same values with respect to those observed in the skimmer chamber for $Q_{\mathrm{m}} < 1\,\mathrm{mbar\,l/s}$. From this behaviour one can conclude, that a nozzle–skimmer distance of 78 mm actually provides free conductance to the pumps. Moreover it seems, that in the range of low gas throughputs the density in the beam behind the nozzle is not high enough to avoid rest gas penetration into the beam core. However, for throughputs beyond $1\,\mathrm{mbar\,l/s}$, $\sigma_{\mathrm{rg}}^{\mathrm{eff}}$ in the dissociator chamber decreases much stronger than in the skimmer chamber, resulting in a value of about $0.55 \times 10^{-14}\,\mathrm{cm}^2$ at $6\,\mathrm{mbar\,l/s}$. Therefore, one can conclude a pronounced shielding effect of the beam in the nozzle–skimmer region at high nozzle throughputs.

The results obtained for deuterium are shown in the right graph of fig. 8.4. The behaviour is qualitatively the same as that of hydrogen. For gas throughputs below $1\,\mathrm{mbar\,l/s}$, the cross sections measured in both chambers have the same values and decrese strongly with increasing throughput. It is observed for $Q_{\mathrm{m}} > 1\,\mathrm{mbar\,l/s}$, that $\sigma_{\mathrm{rg}}^{\mathrm{eff}}$ decreases stronger with increasing throughputs compared to hydrogen. In the skimmer chamber, $\sigma_{\mathrm{rg}}^{\mathrm{eff}}$ decreases by a factor of 1.21 when the throughput is increased from 1 to $6\,\mathrm{mbar\,l/s}$ and in the dissociator chamber even by a factor of 2.31. Since no shielding effect is expected in the skimmer chamber due to correspondingly low beam densities, the stronger decrease of $\sigma_{\mathrm{rg}}^{\mathrm{eff}}$ for deuterium in both chambers compared to hydrogen may be attributed to a different evolution of the velocities with increasing throughput or to a different velocity dependence of the cross sections.

Comparing the relative decrease in $\sigma^{\mathrm{eff}}_{\mathrm{rg,H}}$ for $Q_{\mathrm{m}} = 1 \ldots 6\,\mathrm{mbar\,l/s}$ for hydrogen in the dissociator chamber and the skimmer chamber, one obtains

$$\frac{\sigma^{\mathrm{eff}}_{\mathrm{rg,dis\text{-}ch,H}}(Q_{\mathrm{m}} = 1\,\mathrm{mbar\,l/s})/\sigma^{\mathrm{eff}}_{\mathrm{rg,dis\text{-}ch,H}}(Q_{\mathrm{m}} = 6\,\mathrm{mbar\,l/s})}{\sigma^{\mathrm{eff}}_{\mathrm{rg,sk\text{-}ch,H}}(Q_{\mathrm{m}} = 1\,\mathrm{mbar\,l/s})/\sigma^{\mathrm{eff}}_{\mathrm{rg,sk\text{-}ch,H}}(Q_{\mathrm{m}} = 6\,\mathrm{mbar\,l/s})} = \frac{2}{1.16} = 1.72\,.$$

In case of deuterium the above ratio is equal to $2.31/1.21 = 1.91$. From this ratio one can conclude, that the shielding effect in the nozzle–skimmer region is somewhat more pronounced for deuterium than for hydrogen.

In order to extract the velocity dependence of the single scattering loss cross section, without explicitly performing velocity measurements, the compression tube pressure p_{ct} being proportional to the beam intensity has been compared with the beam partial pressure signal $S^{\mathrm{QMS}}_{\mathrm{D_2}}$ detected by the QMS for a molecular deuterium beam. Since $p_{\mathrm{ct}} \propto v^{\mathrm{beam}}\, S^{\mathrm{QMS}}_{\mathrm{D_2}}$, the ratio $p_{\mathrm{ct}}/S^{\mathrm{QMS}}_{\mathrm{D_2}}$ is proportional to the mean beam velocity v^{beam}. The measured dependence of $p_{\mathrm{ct}}/S^{\mathrm{QMS}}_{\mathrm{D_2}}$ on the gas throughput is shown in fig. 8.5. The data have been obtained in the course of a flux calibration measurement recording p_{ct} and $S^{\mathrm{QMS}}_{\mathrm{D_2}}$ measured by means of the lock–in amplifier. In order to obtain the relative

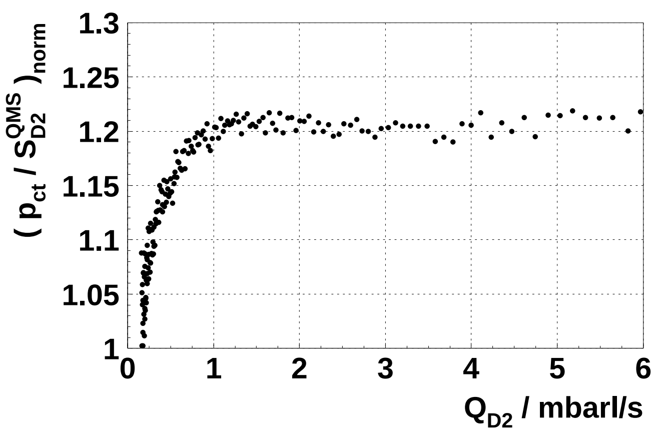

Fig. 8.5: Dependence of of the normalized relative beam velocity given by the ratio $(p_{\mathrm{ct}}/S^{\mathrm{QMS}}_{\mathrm{D_2}})_{\mathrm{norm}}$ on the gas throughput Q_{m} for a molecular deuterium beam at a nozzle temperature of 100 K.

change in velocity, $p_{\mathrm{ct}}/S^{\mathrm{QMS}}_{\mathrm{D_2}}$ is normalised to 1 at the minimum throughput investigated of $Q_{\mathrm{m}} = 0.25\,\mathrm{mbar\,l/s}$ corresponding to molecular flow out of the nozzle and hence to thermal velocity of the D_2 molecules. Due to adiabatic expansion, the velocity increases steeply with increasing throughput by up to a factor of 1.2 at $1.25\,\mathrm{mbar\,l/s}$. For higher throughputs, the measured data indicate a saturation in the mean velocity of the beam. A similar behaviour is found measuring $p_{\mathrm{ct}}/S^{\mathrm{QMS}}_{\mathrm{H_2}}$ for a molecular hydrogen beam. Therefore, it can be assumed, that the steep decrease of the effective single scattering loss cross section measured in the skimmer chamber for gas throughputs between 0.25 mbar l/s and 1 mbar l/s is due to a $1/v^{\text{beam}}$–dependence of $\sigma_{\text{rg}}^{\text{eff}}$.

8.3 Pressure bumps

Based on the results obtained for the effective single scattering loss cross sections, a method has been developed to determine the residual gas pressure in the vicinity of the beam. The motivation is to get a quantitive estimate of the pressure bumps in the nozzle–skimmer and the skimmer–collimator area for the compact ABS geometry, where the pumping conductances are assumed to be limited. Since the residual gas is injected in direct vicinity to the beam, an obstruction of the conductance to the pumps will result in an increased residual gas pressure close to the beam, a so–called "pressure bump". In this case, the pressure measured at the circumference of the vacuum chamber, which is still the same as in the case of a non–restricted conductance, will not represent the rest gas pressure on the beam axis anymore. Consequently, the effective cross section determined with an obstructed conductance will be higher. The pressure bump factor β, which denotes the ratio between the increased rest gas pressure caused by a restricted conductance and the initial rest gas pressure, is then obtained from the ratio of the corresponding cross sections.

In order to determine the pressure bump in the dissociator chamber, the nozzle skimmer distance has been varied in the range of $d_{\text{nz-sk}} = 8\ldots78\,\text{mm}$. Taking into account eq. (8.3), the pressure bump factor $\beta_{\text{dis-ch}}$ in the nozzle–skimmer region as a function of $d_{\text{nz-sk}}$ can then be written as

$$\beta_{\text{dis-ch}}(d_{\text{nz-sk}}) \equiv \frac{p(d_{\text{nz-sk}})}{p(78\,\text{mm})} = \frac{78\,\text{mm}}{d_{\text{nz-sk}}}\,\frac{\Delta\ln\Phi_{\text{m}}^{\text{ct}}(d_{\text{nz-sk}})}{\Delta\ln\Phi_{\text{m}}^{\text{ct}}(78\,\text{mm})}\,, \tag{8.4}$$

where it is assumed, that a nozzle–skimmer distance of 78 mm yields free conductance to the pumps.

It has been observed, that $\beta_{\text{dis-ch}}$ depends only on $d_{\text{nz-sk}}$ and shows no dependence on the gas throughput in a range between 0.25 and 6 mbar l/s. The independence of the gas throughput is an indication for the expected molecularity of the rest gas flow. Moreover, $\beta_{\text{dis-ch}}$ is practically the same for an atomic and a molecular beam.

In fig. 8.6, the pressure bump factor $\beta_{\text{dis-ch}}$ is shown as a function of the nozzle–skimmer distance $d_{\text{nz-sk}}$ for a molecular hydrogen and deuterium beam at the standard nozzle temperature of 100 K. In case of deuterium it was found for $d_{\text{nz-sk}} = 78\ldots15\,\text{mm}$, that $\beta_{\text{dis-ch}}$ rises linearly with a moderate slope up to a value around 1.35. For nozzle positions closer to the skimmer, a steep increase in the pressure bump factor has been observed. For hydrogen, $\beta_{\text{dis-ch}}$ has been determined for only three distances. The behaviour is similar to that of deuterium for distances beyond 15 mm, however for the lowest possible distance $d_{\text{nz-sk}} = 8\,\text{mm}$, the pressure bump factor is clearly lower.

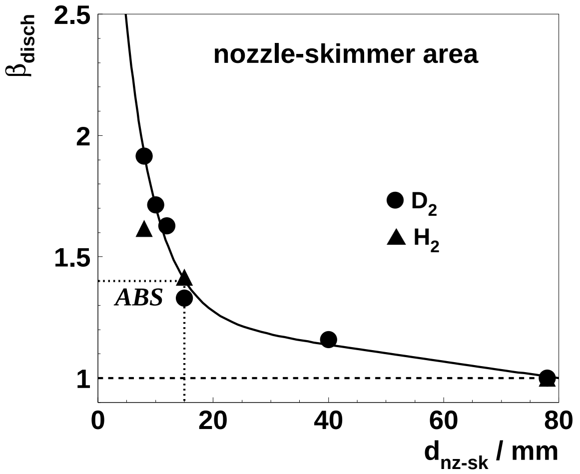

Fig. 8.6: Dependence of the pressure bump factor $\beta_{\text{dis-ch}}$ in the nozzle–skimmer area on the nozzle–skimmer distance $d_{\text{nz-sk}}$. Shown are the results for a molecular hydrogen and deuterium beam at a nozzle temperature of 100 K. The curve shows a fit to the data points taken for deuterium. The nozzle–skimmer distance of the HERMES–ABS and the resulting pressure bump factor is indicated.

In order to predict $\beta_{\text{dis-ch}}(d_{\text{nz-sk}})$ for the HERMES–ABS, the data points have been fitted with a function of the form:

$$\beta_{\text{dis-ch}}(d_{\text{nz-sk}}) = c_0 + c_1\, d_{\text{nz-sk}} + c_2\, \exp\left(c_3\, d_{\text{nz-sk}}\right),$$

where $c_i\, , i = 1 \ldots 3$, are fit parameters.
For typical ABS nozzle–skimmer distances $d_{\text{nz-sk}} = 12 \ldots 16\,\text{mm}$, $\beta_{\text{dis-ch}}$ ranges between 1.6 and 1.4.

The expected rest gas pressure bump in the skimmer–collimator area has been determined varying the geometry of the separation wall between the skimmer chamber and the collimator chamber. Three cylinders with a diameter of 200 mm and different lengths have been used to experimentally simulate the restricted conductance in the ABS skimmer–collimator area. The setup of the modified skimmer chamber is illustrated in fig. 8.7. The skimmer–collimator distances $d_{\text{sk-col}}$ obtained this way are 50, 100, 150 and 300 mm, the latter value corresponding to a plane separation wall according to the standard geometry of the ABT as shown in figs. 6.1 and E.1. Hence, taking into account a skimmer length of $l_{\text{sk}} = 20\,\text{mm}$, in case of a skimmer–collimator distance of 50 mm the pumping conductance for removing the rest gas out of the beam region is defined by two large parallel plates with a gap of only 30 mm in between. This situation is rather similar to that of the HERMES–ABS[5] . The pressure bump factor $\beta_{\text{sk-ch}}$ in the skimmer chamber is obtained in analogy to eq. (8.4), and one has:

$$\beta_{\text{sk-ch}}(d_{\text{sk-col}}) \equiv \frac{p(d_{\text{sk-col}})}{p(300\,\text{mm})} = \frac{300\,\text{mm}}{d_{\text{nz-sk}}}\, \frac{\Delta \ln \Phi_{\text{m}}^{\text{ct}}(d_{\text{sk-col}})}{\Delta \ln \Phi_{\text{m}}^{\text{ct}}(300\,\text{mm})}\,, \tag{8.5}$$

[5]However, regarding the sophisticated design of the ABS skimmer chamber as indicated in fig. 2.4, the actual conductance should be somewhat larger despite of the smaller skimmer–collimator distance of about 40 mm.

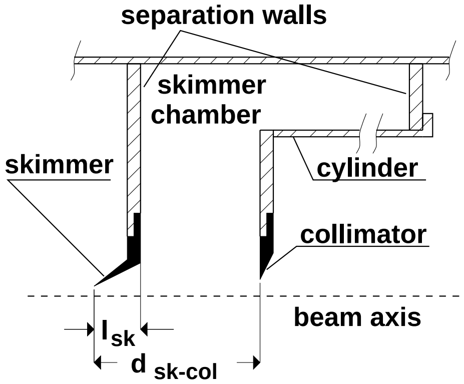

Fig. 8.7: Illustration of the setup for pressure bump simulation in the skimmer chamber. Three cylinders were used to subsequently reduce the pumping conductance for the residual gas in the vicinity of the beam.

where $d_{\text{nz-sk}}$ is the skimmer–collimator distance. It is assumed, that for a plane separation wall between skimmer chamber and collimator chamber, equal to $d_{\text{nz-sk}} = 300\,\text{mm}$, free conductance to the pumps is provided.

Figure 8.8 shows the dependence of $\beta_{\text{sk-ch}}$ on $d_{\text{sk-col}}$ for a molecular deuterium and hydrogen beam at a nozzle temperature of 100 K. For both hydrogen and deuterium, the pressure bump adopts the same values for a given skimmer–collimator distance. Compared to the situation of free conductance obtained for $d_{\text{sk-col}} = 300\,\text{mm}$, hardly a pressure bump effect is observed for a distance of 150 mm. If $d_{\text{sk-col}}$ is reduced further to 100 mm and finally 50 mm, $\beta_{\text{sk-ch}}$ rises strongly up to values of about 1.35 and 2.2, respectively. In

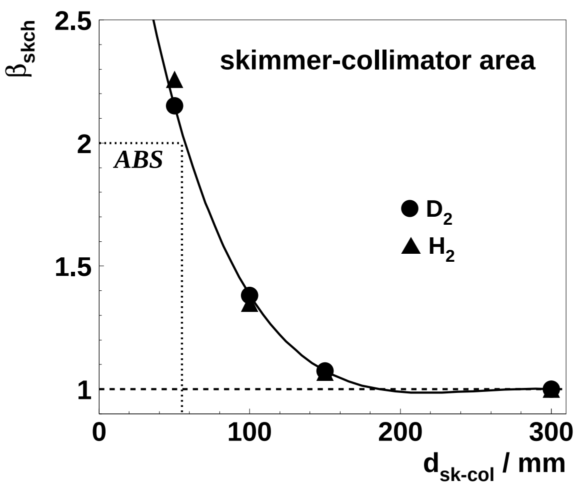

Fig. 8.8: Dependence of the pressure bump factor $\beta_{\text{sk-ch}}$ in the skimmer–collimator area on the skimmer–collimator distance $d_{\text{sk-col}}$. The results were obtained for a molecular hydrogen and deuterium beam at a nozzle temperature of 100 K. The curve shows a fit to the data points. The pressure bump expected for the HERMES–ABS is indicated.

order to predict $\beta_{\text{sk-ch}}$ for intermediate values of $d_{\text{sk-col}}$, the data points have been fitted as

$$\beta_{\text{sk-ch}}(d_{\text{sk-col}}) = c_0 + c_1\, d_{\text{sk-col}} + c_2\, d^2_{\text{sk-col}} + c_3\, d^3_{\text{sk-col}} + c_4\, \exp\left(c_5\, d_{\text{sk-col}}\right),$$

where $c_i\,, i = 1 \ldots 4$ are fit parameters.
In case of the HERMES–ABS, a pressure bump factor of $\beta_{\text{sk-ch}} \approx 2$ can be extracted.

8.4 Determination of the peaking exponent

In the following, the peaking exponent will be determined based on the intensity description in section 8.1. Since the dependence of the effective single scattering loss cross section on the gas throughput as well as the pressure bump factor have been measured, all parameters needed to predict the molecular intensity according to eq. (8.1) are known, except for the peaking exponent n. In order to determine n, the skimmer chamber has been used as intensity detector. The flow rate $Q_{\text{sk-ch}}$ into the skimmer chamber can be determined from the pressure rise measured with the ion gauge, which has been calibrated by means of the side gas inlet as described in section 6.2.

Injecting gas from the dissociator, $Q_{\text{sk-ch}}$ is composed of the attenuated ballistic nozzle beam and the effusive contribution $Q^{\text{dis-ch}}_{\text{eff}}$ arising from the pressure difference between dissociator and skimmer chamber as follows:

$$\begin{aligned} Q_{\text{sk-ch}}(Q_{\text{m}},\, d_{\text{nz-sk}}) = \;& Q_{\text{m}} \left(1 - \cos^{n(Q_{\text{m}})+1} \vartheta_{\text{sk}}(d_{\text{nz-sk}})\right) S_{\text{dis-ch}}(Q_{\text{m}},\, d_{\text{nz-sk}}) \\ +\;& Q^{\text{dis-ch}}_{\text{eff}}(Q_{\text{m}}), \end{aligned} \tag{8.6}$$

where ϑ_{sk} is the polar opening angle of the skimmer and $S_{\text{dis-ch}}(Q_{\text{m}},\, d_{\text{nz-sk}})$ is the RGA induced attenuation factor in the dissociator chamber.
Taking into account eq. (8.2), $S_{\text{dis-ch}}$ can be written as

$$S_{\text{dis-ch}}(Q_{\text{m}},\, d_{\text{nz-sk}}) = \exp\left[-\frac{d_{\text{nz-sk}}}{k\, T_{\text{rg}}}\, p_{\text{dis-ch}}(Q_{\text{m}})\, \beta_{\text{dis-ch}}(d_{\text{nz-sk}}) \left(\sigma^{\text{eff}}_{\text{rg}}(Q_{\text{m}})\right)_{\text{dis-ch}}\right], \tag{8.7}$$

where $p_{\text{dis-ch}}$ is the pressure in the dissociator chamber read out by means of the ion gauge and $\left(\sigma^{\text{eff}}_{\text{rg}}\right)_{\text{dis-ch}}$ is the effective scattering loss cross section in the dissociator chamber as determined previously.
Rearranging eq. (8.6) yields:

$$n = \frac{\ln\left\{\left[\left(Q^{\text{dis-ch}}_{\text{eff}} - Q_{\text{sk-ch}}\right)/Q_{\text{m}}\, S_{\text{dis-ch}}\right] + 1\right\}}{\ln\left(\cos\vartheta_{\text{sk}}\right)} - 1\,. \tag{8.8}$$

The effusive contribution $Q^{\text{dis-ch}}_{\text{eff}}$ has been determined recording the pressure $p_{\text{sk-ch}}$ in the skimmer chamber, whilst gas has been injected into the dissociator chamber with the side inlet. Since the ion gauge in the skimmer chamber has been calibrated, one obtains $Q^{\text{dis-ch}}_{\text{eff}}$ as a function of the pressure $p_{\text{dis-ch}}$ in the dissociator chamber, $p_{\text{dis-ch}}$

being a function of the nozzle throughput Q_{m}. In order to approach the point–source situation assumed for the description of the intensity distribution despite of the finite nozzle diameter of 2 mm, the nozzle–skimmer distance has been set to the maximum of $d_{\text{nz-sk}} = 78\,\text{mm}$. In addition, this results in $\beta_{\text{dis-ch}} = 1$. Hence, all parameters appearing in eq. (8.8) are parametrized as a function of Q_{m} and n can be determined in the course of a flux calibration, recording the ion gauge pressures in the first two chambers.

The determination of the peaking exponent as a function of nozzle throughput shown in fig. 8.9 has been done for a molecular deuterium beam at a nozzle temperature of 100 K. For throughputs up to 3.5 mbar l/s, n rises nearly linear up to a value around

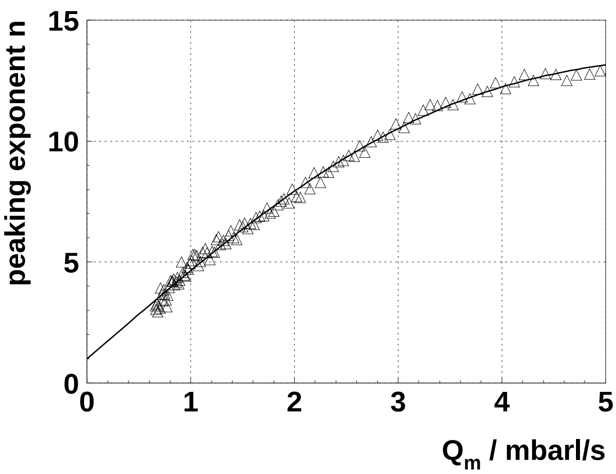

Fig. 8.9: Dependence of the peaking exponent n on the nozzle throughput Q_{m} for a molecular deuterium beam at a nozzle temperature of 100 K. The line denotes a fit to the experimental data.

12. If Q_{m} is increased further, the increase in n is less strong, and around 5 mbar l/s, n starts to saturate at a value around 13. Extrapolating the values to $Q_{\mathrm{m}} \to 0$ yields $n \to 1$ as expected for molecular flow. The increase of n with increasing gas throughput is expected from beam formation theory, since a higher throughput and hence pressure in the nozzle results in a more pronounced beam expansion (see section 2.1). However, it is in contradiction to a constant value of n around 2 used for ABS–intensity modelling in ref. [128].

In order to verify the description of RGA losses applied in this work, Mach–numbers $M(n)$ have been derived from the extracted peaking exponents given in fig. 8.9 following eq. (2.15). The values obtained this way have been compared to preliminary data on Mach–numbers M_{TOF}, derived from beam temperatures and drift velocities according to eq. (2.14), which are currently being measured in the course of TOF studies [112] for the same nozzle geometry and temperature. In fig. 8.10, $M(n)$ and M_{TOF} are shown as a function of nozzle throughput. Qualitatively, $M(n)$ and M_{TOF} show a similar evolution with Q_{m}. The Mach–numbers rise with increasing nozzle throughput and saturate for throughputs beyond about 4 mbar l/s. Comparing the Mach–numbers quantitatively, one

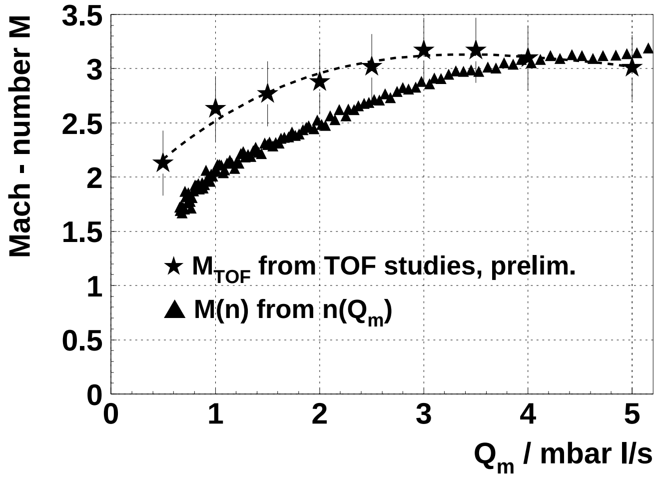

Fig. 8.10: Dependence of the Mach–number M on the nozzle throughput Q_{m}. The triangles and stars denote the Mach–numbers $M(n)$ and M_{TOF} derived from the peaking exponent n determined above, and preliminary results from TOF studies, respectively. The dashed curve represents a fit to the M_{TOF} values.

can see that M_{TOF} saturates somewhat earlier than $M(n)$ and is up to a factor of 1.3 higher at the lowest throughputs investigated. For $Q_{\mathrm{m}} \geq 3\,\mathrm{mbar\,l/s}$, $M(n)$ and M_{TOF} are equal within the systematic errors. However, there is an indication of a slight drop in M_{TOF} beyond saturation. In general, one can conclude that the Mach–numbers derived from the intensity model using the skimmer chamber as intensity detector are in reasonable agreement with the values derived from the measured velocity distributions.

8.5 Intensity prediction

In order to check the validity of the model assumption according to which the losses are exclusively due to rest gas attenuation, the expected flow rate into the compression tube $(\Phi_{\mathrm{m}}^{\mathrm{ct}})_{\mathrm{calc}}$ for a given configuration has been calculated based on eq. (8.1) and compared to the measured values. For a prediction of $(\Phi_{\mathrm{m}}^{\mathrm{ct}})_{\mathrm{calc}}$ as a function of nozzle throughput, the throughput dependences of the effective loss cross section and peaking exponent determined in the previous sections have been parametrized as a function of throughput. It has been assumed, that the loss cross section in the collimator and the analysis chamber is equal to the one measured for the skimmer chamber. Due to the calibration of the compression tube ion gauge, $(\Phi_{\mathrm{m}}^{\mathrm{ct}})_{\mathrm{calc}}$ can be expressed as pressure rise in the compression tube and hence directly compared with the measured pressure rise p_{ct}.

As for the determination of the peaking exponent, the nozzle–skimmer distance has been set to 78 mm and p_{ct} has been determined in the course of a flux calibration, where all chamber pressures have been read out. Hence the dependence of the rest gas pressures on the throughput are known, and the attenuation losses in the different chambers of the atomic beam test stand can be determined. The attenuation factors $S_{\text{dis-ch}}$, $S_{\text{sk-ch}}$, $S_{\text{col-ch}}$ and $S_{\text{an-ch}}$ of the dissociator, skimmer, collimator and analysis chamber are shown

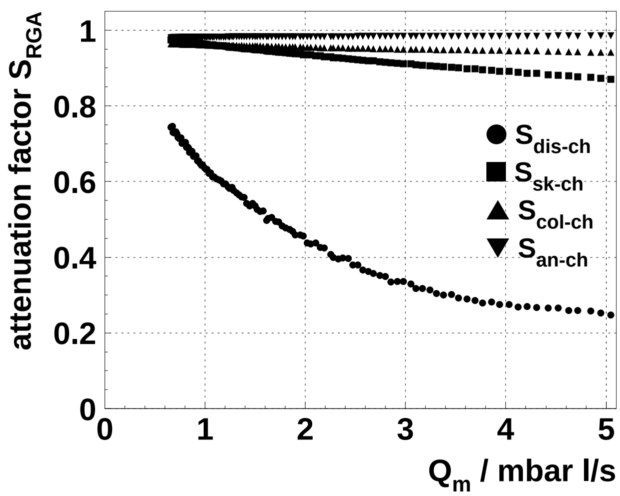

Fig. 8.11: Dependence of the attenuation factor S_{RGA} in the various ABT chambers on the nozzle throughput Q_{m} for a molecular deuterium beam at a nozzle temperature of 100 K and nozzle–skimmer distance of 78 mm and a skimmer–collimator distance of 300 mm.

in fig. 8.11. It is found, that the RGA induced attenuation is dominated by the losses in the dissociator chamber. At the lowest throughput investigated, already 25 % of the nozzle beam are lost, and the loss increases to about 75 % at $Q_{\mathrm{m}} = 5\,\mathrm{mbar\,l/s}$. The beam losses in the skimmer chamber are at maximum 15 %, and rest gas attenuation in the collimator and analysis chamber is negligible.

Based on the determined attenuation factors, the expected throughput dependence of $(\Phi_{\mathrm{m}}^{\mathrm{ct}})_{\mathrm{calc}}$ has been calculated for different peaking exponents n. Apart for $n = n(Q_{\mathrm{m}})$ determined above by using the skimmer chamber as intensity detector, the calculations have additionally been performed for a constant peaking exponent of $n = 2$, as assumed in ref. [128] and for $n = n(M_{\mathrm{TOF}})$ derived from the measured Mach–numbers M_{TOF}.

A comparison of the measured intensity with the calculated intensities is shown in fig. 8.12. The measured intensity increases for throughputs below 1.5 . . . 2 mbar l/s and then starts to decrease indicating strong beam attenuation. In case of all calculated curves, one observes a clear difference between the measured intensity and the model expectation. Only for a constant value of $n = 2$, reasonable agreement is found for gas throughputs below 1.5 mbar l/s. Using the peaking exponents $n = n(M_{\mathrm{TOF}})$ derived from measured Mach–numbers and $n = n(Q_{\mathrm{m}})$, which both rise with increasing throuhput, leads to a large deviation compared to the measured intensity over the entire range. None of the peaking values applied explains the drop of the measured intensity beyond $Q_{\mathrm{m}} = 2.0\,\mathrm{mbar\,l/s}$. All calculated curves show a nearly linear increase with throughput below 1 . . . 2 mbar l/s, however with a different slope. For higher throughputs, the evolution is again nearly linear, with a smaller slope than for the low range. In case of $n = n(M_{\mathrm{TOF}})$, the predicted increase in intensity for low throughputs is the largest of all curves. Due to the saturation of M_{TOF}, the expected intensity flattens out for $Q_{\mathrm{m}} \geq 2.5\,\mathrm{mbar\,l/s}$. The intensity predicted by using the peaking exponent derived from the TOF studies is

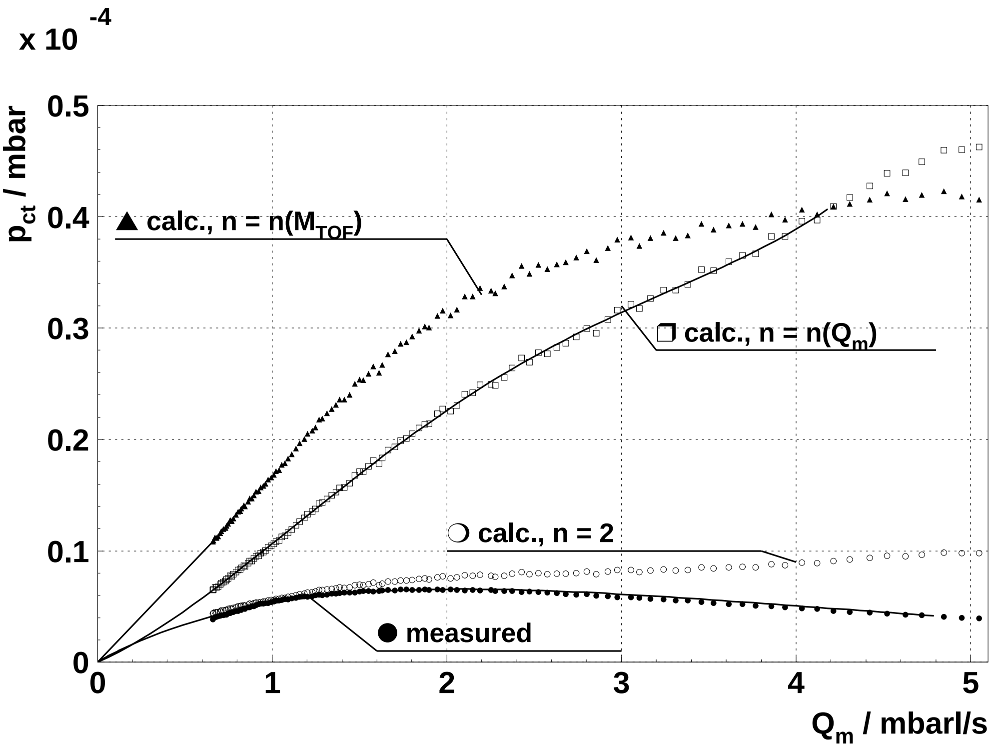

Fig. 8.12: Dependence of the pressure rise p_{ct} in the compression tube on the nozzle throughput Q_m for a molecular deuterium beam at a nozzle temperature of 100 K. Shown are the measured values (full dots), and those calculated for various peaking exponents (for explanation see text). The lines denotes a fit to the data for the extrapolation to $Q_m \rightarrow 0$.

a factor of 3 to 10 higher than the measured one over the entire range investigated. A similar result is obtained for the intensity calculated for $n = n(Q_m)$. The curve shows a nearly linear increase with throughput over the entire range. Only for values beyond 4.5 mbar l/s, the predicted intensity saturates. Compared to the measured curve, the model predicts higher intensities by a factor of 1.5 for low throughputs and by more than 10 for the highest throughputs investigated.

8.6 Rest gas attenuation within the HERMES–ABS

Owing to the previous studies, the RGA induced beam losses in the dissociator chamber and skimmer chamber of the HERMES–ABS can be calculated. In the following, only the attenuation losses at the ABS working point for both hydrogen and deuterium shall be estimated. For a given gas throughput and nozzle temperature, the rest gas attenuation factors in the first two chambers can be written as

$$S_{\text{dis-ch}} = \exp\left(-\frac{1}{k\,T_{\text{rg}}}\left(\sigma^{\text{eff}}_{\text{rg,dis-ch}}\,\beta_{\text{dis-ch}}\right)_{d_{\text{nz-sk}}}\,d_{\text{nz-sk}}\,p_{\text{dis-ch}}\right)$$

$$\text{and}\quad S_{\text{sk-ch}} = \exp\left(-\frac{1}{k\,T_{\text{rg}}}\left(\sigma^{\text{eff}}_{\text{rg,sk-ch}}\,\beta_{\text{sk-ch}}\right)_{d_{\text{sk-col}}}\,d_{\text{sk-col}}\,p_{\text{sk-ch}}\right) \tag{8.9}$$

The parameters appearing above are taken from the previous RGA studies and table A.1, and the resulting attenuation factors are summarized in table 8.1 for a standard gas throughput of 1.25 mbar l/s and 1.0 mbar l/s for hydrogen and deuterium, respectively, and a nozzle temperature of 100 K. It is found, that the rest gas induced beam

	dissociator chamber	**skimmer chamber**
pressure	$p_{\text{dis-ch,H}} = 3 \times 10^{-4}$ mbar $p_{\text{dis-ch,D}} = 2.4 \times 10^{-4}$ mbar	$p_{\text{sk-ch,H}} = 6 \times 10^{-5}$ mbar $p_{\text{sk-ch,D}} = 4.8 \times 10^{-5}$ mbar
attenuation length	$d_{\text{nz-sk}} = 15$ mm	$d_{\text{sk-col}} = 40$ mm
pressure bump factor	$\beta_{\text{dis-ch}} = 1.4$	$\beta_{\text{sk-ch}} = 2.0$
eff. loss cross sections	$\sigma^{\text{eff}}_{\text{rg,dis-ch,H}} = 0.72 \times 10^{-14}\,\text{cm}^2$ $\sigma^{\text{eff}}_{\text{rg,dis-ch,D}} = 0.81 \times 10^{-14}\,\text{cm}^2$	$\sigma^{\text{eff}}_{\text{rg,sk-ch,H}} = 0.80 \times 10^{-14}\,\text{cm}^2$ $\sigma^{\text{eff}}_{\text{rg,sk-ch,D}} = 0.91 \times 10^{-14}\,\text{cm}^2$
attenuation factors	$S_{\text{dis-ch,H}} = 0.90$ $S_{\text{dis-ch,D}} = 0.93$	$S_{\text{sk-ch,H}} = 0.91$ $S_{\text{sk-ch,D}} = 0.96$

Tab. 8.1: Pressures, attenuation lengths, pressure bump factors, effective single scattering loss cross sections and resulting rest gas attenuation factors for the dissociator chamber and the skimmer chamber of the HERMES–ABS under nominal working conditions for both an atomic hydrogen and a deuterium beam.

attenuation at the ABS working point is $S_{\text{dis-ch}}\,S_{\text{sk-ch}} = 0.82$ in case of hydrogen and 0.89 in case of deuterium.

In order to determine the total rest gas attenuation factor, also the RGA losses occuring in the sixpole magnets have to be considered. Rest gas attenuation in the sixpoles is caused by atoms or molecules hitting the inner walls of the magnets. Therefore, a rest gas pressure is built up, since the magnet bores have only low pumping conductances due to their small diameter. However, the pressure in the magnet bores cannot be accessed directly. In the course of previous studies, dummy magnets made of aluminum had been used to study the attenuation of molecular beams [41]. As a result, the (real) sixpole magnets have been split up into sets consisting of typically two or three magnets in order to provide a better pumping conductance (see section 2.2). However, it was not clear, whether the rest gas pressure caused by an atomic beam within the real sixpole magnets has a comparable order of magnitude, due to the different atomic and molecular trajectories. Molecules are not affected by the magnetic field and pass the magnet system on straight lines. In contrast, most of the atoms with $m_S = -1/2$ are deflected and collide with the inner magnet walls of the first sixpole set, whereas a substantial fraction of those with $m_S = +1/2$ are foccussed and leave the first sixpole set with trajectories parallel to the beam axis. Consequently, one might expect the rest gas pressures caused by atoms and molecules to be different.

A systematic investigation of this problem has been performed in the course of Monte–Carlo (MC) simulations [131]. The trajectories of both atoms and molecules have been calculated, taking into account the ABS geometry as well as the magnetic field gradients for the given sixpole magnet system. Atoms colliding with the inner magnet walls were assumed to recombine on the surface and to be re–emitted as molecules according to a cosine distribution. This allowed to calculate the rest gas pressure in the magnet bores. As a result, only a minor dependence of the rest gas pressure in the magnets on the atomic fraction in the beam has been found. The attenuation factor obtained ranged between 0.98 and 0.96 for $n = 2.2$ and $n = 5$, respectively. Therefore, RGA induced losses within the HERMES–ABS are dominated by the losses occuring in the dissociator and skimmer chamber.

Based on the results on RGA attenuation and of the degree of dissociation measurements with the radio frequency dissociator in section 7.6, the ABS output intensity can be predicted following eq. (2.11). The transmission for the sixpole magnet has been calculated in the course of the MC studies mentioned above to be $\mathcal{T}_{\rm mag} = 0.235$. In table 8.2, the expected intensities for two different peaking exponents are compared with the measured intensity. Similar to the results on attenuation of molecular beams, the

	intensity
measured	$6.4 \times 10^{16}\,\mathrm{s}^{-1}$
calculated, $n = 2$	$7.5 \times 10^{16}\,\mathrm{s}^{-1}$
calculated, $n = 5$	$1.5 \times 10^{17}\,\mathrm{s}^{-1}$

Tab. 8.2: Comparison between measured and calculated intensities of the HERMES–ABS.

predicted ABS intensity considering exclusively RGA losses is in rough agreement with the measured value only, if a small peaking exponent of $n = 2$ is assumed, and deviates by a factor of 2.3 in case of $n = 5$.

Finally it will be estimated, to which extent the difference in the measured output intensities for hydrogen and deuterium provided by the ABS can be explained by the different RGA factors and degrees of dissociation obtained above and in section 7, respectively. Considering eq. (2.11), the ABS output flow rate into the storage cell entrance tube is proportional to a factor F given by the product of throughput, degree of dissociation at the optimum incident radio frequency power and total RGA attenuation factor as

$$F = Q_{\mathrm{m}}\,\alpha(P^{\mathrm{opt}})\,S_{\mathrm{RGA}}\,. \tag{8.10}$$

The parameters appearing in eq. (8.10) and the resulting factor F are summarized in table 8.3 for the working point parameters of the HERMES–ABS for hydrogen and deuterium. Based on former TOF studies [50], the transmission $\mathcal{T}_{\mathrm{mag}}$ through the sixpole

	hydrogen	**deuterium**
nozzle throughput	$Q_{\mathrm{m,H}} = 1.25\,\mathrm{mbar\,l/s}$	$Q_{\mathrm{m,D}} = 1.0\,\mathrm{mbar\,l/s}$
optimum radio frequency power	$P^{\mathrm{opt}} = 300\,\mathrm{W}$	$P^{\mathrm{opt}} = 250\,\mathrm{W}$
degree of dissociation	$\alpha_{\mathrm{H}} = 0.82$	$\alpha_{\mathrm{D}} = 0.75$
total RGA factor	$S_{\mathrm{RGA,H}} = 0.79$	$S_{\mathrm{RGA,D}} = 0.85$
factor F	$F_{\mathrm{H}} = 0.81\,\mathrm{mbar\,l/s}$	$F_{\mathrm{D}} = 0.64\,\mathrm{mbar\,l/s}$

Tab. 8.3: Working point parameters of the HERMES–ABS for the calculation of the factors F_{H} and F_{D} for hydrogen and deuterium, respectively.

system is equal for hydrogen and deuterium atoms. Moreover, an equal peaking exponent is assumed. Consequently, the expected output intensity $\left(\Phi_{\vec{\mathrm{D}}}^{\mathrm{cell}}\right)_{\mathrm{exp}}$ of deuterium normalized to the hydrogen intensity $\left(\Phi_{\vec{\mathrm{H}}}^{\mathrm{cell}}\right)_{\mathrm{meas}} = 6.4 \times 10^{16}\,\mathrm{s}^{-1}$ measured before the HERMES–ABS has been installed in the experiment is given as

$$\left(\Phi_{\vec{\mathrm{D}}}^{\mathrm{cell}}\right)_{\mathrm{exp}} = \frac{F_{\mathrm{D}}}{F_{\mathrm{H}}}\left(\Phi_{\vec{\mathrm{H}}}^{\mathrm{cell}}\right)_{\mathrm{meas}} = 5.1 \times 10^{16}\,\mathrm{s}^{-1}\,. \tag{8.11}$$

This in in good agreement with the measured deuterium output intensity of $\left(\Phi_{\vec{\mathrm{D}}}^{\mathrm{cell}}\right)_{\mathrm{meas}} = 5.2 \times 10^{16}\,\mathrm{s}^{-1}$ given in ref. [23].

8.7 Summary

Owing to a suitable choice of the experimental conditions, precise measurements of the parameters affecting beam losses caused by rest gas attenuation could be performed.

The effective single scattering loss cross section $\sigma_{\mathrm{rg}}^{\mathrm{eff}}$ has been measured as a function of nozzle temperature for atomic and molecular hydrogen and deuterium beams, showing a strong increase of $\sigma_{\mathrm{rg}}^{\mathrm{eff}}$ for decreasing temperatures. This implies a velocity dependence of the cross section, which has been indirectly confirmed by the observed decrease of $\sigma_{\mathrm{rg}}^{\mathrm{eff}}$

with increasing gas throughput. The lower effective cross section found in the dissociator chamber compared to the skimmer chamber especially for high gas flows indicates a shielding effect against rest gas penetration into the beam core close to the nozzle.

A method has been developed to quantitatively determine the rest gas pressure bumps arising in regions with restricted pumping conductance such as the nozzle–skimmer area and the skimmer–collimator area. It has been found, that in case of the compact geometry of the HERMES–ABS the pressure is about 1.5 and 2 times higher in the nozzle–skimmer and the skimmer–collimator region, compared to what is read out at the ion gauges placed at the circumference of the vacuum chambers.

The peaking exponent for a molecular deuterium beam has been determined using the skimmer chamber as intensity detector assuming exclusively rest gas attenuation and the nozzle to be a point–like source. The Mach–numbers derived from the peaking exponent obtained this way are in good agreement with the Mach–numbers determined in the course of currently performed TOF studies.

Using these peaking exponents, much higher molecular beam intensities into the compression tube are expected compared to the measured data. This indicates an additional attenuation mechanism occuring at large distances from the nozzle.

A similar result is obtained for the output intensity estimate of the HERMES–ABS, where additionally the degree of dissociation measurements with the radio frequency dissociator and results from Monte–Carlo calculations for the transmission and rest gas attenuation within the sixpole magnets have been considered: only a low peaking exponent can explain the measured output intensity, which is not in agreement with the expectations from the TOF studies. Moreover, it has been found, that the lower output intensity observed for a polarized deuterium beam compared to a hydrogen beam can be explained satisfactorily by the different evolution of the degree of dissociation investigated in section 7.6 and the different attenuation of both beams studied in this section.

9 Discussion and Outlook

In the course of this thesis, a new type of dissociator for the production of intense cold atomic hydrogen and deuterium beams has been developed. Additionally, an atomic beam test stand has been set up in order to investigate the dissociator performance and to study beam attenuation and formation in the range of parameters relevant for a polarized atomic beam source.

In the following, the dissociator development is summarized and the planned upgrades are presented in section 9.1. In section 9.2, the results obtained from the attenuation studies and the next steps towards a possible improvement of the beam phase space density are discussed.

9.1 Dissociator development

The processes in the hydrogen discharge have been described in the framework of a simple model considering the electron kinetics, the balance of charged particles and the atomic loss mechanisms. The model predicts the necessity of a high power density in the discharge in order to efficiently dissociate high gas throughputs and pressures. As a consequence, a 2.45 GHz surface wave plasma source, based on a modified waveguide surfatron field applicator (MWS) has been set up, which yields high power transfer efficiencies to the discharge. Taking into account the discharge model and the theoretical description of surface wave discharges, the observed evolution of the plasma length was used to optimize the plasma source on a test bench. The design of the dissociator takes into account the results of the test bench studies. Moreover, the MWSD is compatible with the geometry of the HERMES–ABS and fulfills the technical requirements arising from the operational mode of the experiment.

The dissociator has been tested in an atomic beam test stand, which was designed especially for the investigation of the nozzle beam properties. The degree of dissociation in the nozzle beam has been measured over a wide range of parameters relevant for the dissociator application in a polarized atomic beam source. High atomic fractions have been achieved up to high gas throughputs owing to a high power density in the discharge, and long running times have been obtained due to a low oxygen admixture. Investigating the recombination losses on various nozzle surfaces over a wide temperature range, it has been found, that at the nominal running conditions a water layer adsorbed on the nozzle dominates the recombination properties. A comparison of the dissociation efficiency with the radio frequency dissociator showed a clearly better performance of the MWSD, especially for higher gas throughputs and deuterium.

For a further improvement and better understanding of the MWS sustained hydrogen discharge, the test bench set–up has been upgraded (section 9.1.1). Furthermore, it is planned to set up an optical discharge monitor (section 9.1.2).

9.1.1 Test bench calorimeter

The possibility to create high power densities with the MWS field applicator as a result of a standing surface wave discharge and the optimization of the plasma source towards high degrees of dissociation at low oxygen admixtures have both been disclosed in the course of the test bench studies. Therefore, an calorimeter for the test bench has been developed in order to perform an absolute measurement of the atomic flow rate from the plasma source. The set–up is similar to fig. 4.6. However, instead of using the temperature rise at the glass–to–metal transition as recombination monitor, which yields only relative values for the atomic flow rate, a small vacuum chamber is placed at the downstream end of the discharge tube.

A schematic representation of the set–up for the test bench upgrade is given in fig. 9.1. Hydrogen or deuterium atoms coming from the plasma source are directed via the dis-

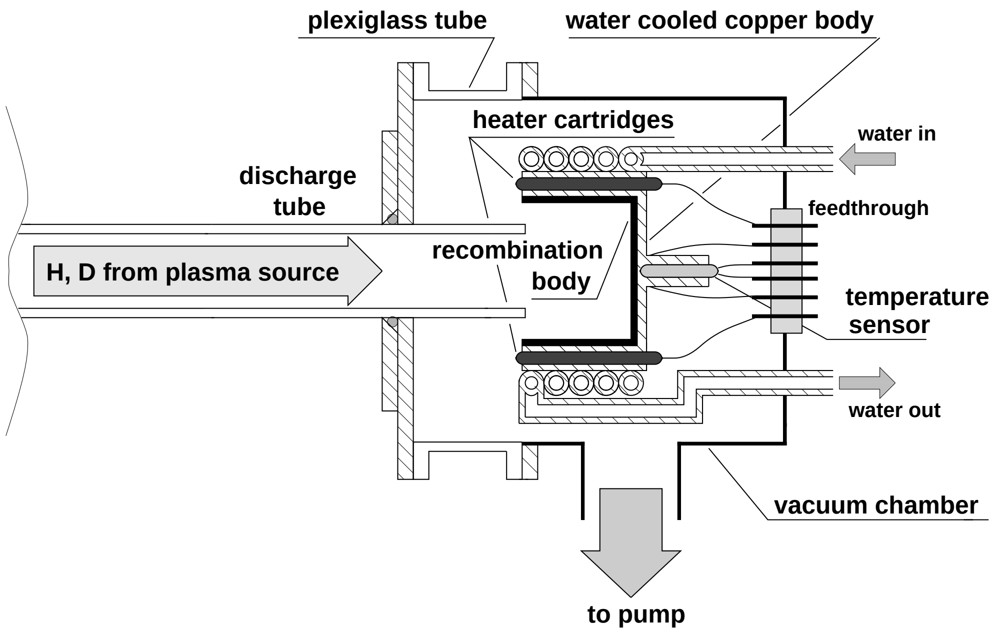

Fig. 9.1: Schematic picture of the calorimeter for the plasma source test bench set–up. The different components are explained in the text.

charge tube into a cylindrical, thin–walled stainless steel recombination body, which is tightly shrinked into a water cooled copper cylinder. Four heater cartridges (TÜRK & HILLINGER, HLP 2.8) with a maximum heating power of 30 W each and a Pt 100 temperature sensor are inserted into the copper cylinder. A plexiglas tube allows to observe the plasma, in case it is propagating towards the end of the discharge tube.

Due to the high recombination coefficient of stainless steel and because of the geometry chosen, the entire atomic flow should recombine on the surface of the recombination body. Therefore, heating powers of several ten watts deposited onto the stainless steel cylinder can be expected in case of a high degree of dissociation and a gas throughput in the range of several mbar l/s (see eq. (4.11)). The resulting temperature rise of the copper cylinder is measured, which is proportional to the atomic flow, provided that the cooling water flow is kept constant. The temperature rise can be calibrated by the heater cartridges, the power consumption of which is precisely determined. Consequently, the absolute heating power due to recombination and hence the atomic flow rate into the recombination body can be measured.

9.1.2 Optical discharge monitor

From all studies performed with the new dissociator, one can conclude that the MWS based plasma source provides a stable and high atomic fraction, and that running time at a degree of dissociation in the nozzle beam is only restricted by the ice layer frozen onto the cold nozzle. However, with respect to the application of the MWSD in the HERMES target source, it is not known, whether continuous running periods extending over months have an impact on the discharge tube surface and hence the degree of dissociation in the plasma. Therefore, it is planned to set up an optical discharge monitor, which would allow for a remote diagnostics of the plasma.

First results by analysing the intensities of the Balmer–H_α, H_β and H_γ lines emitted from the discharge of the radio frequency dissociator of the Erlangen laser–driven source (LDS) are reported in ref. [48]. Based on the optical monitor of a microwave sustained hydrogen discharge operated under similar gas conditions [132], studies on the radio frequency plasma of the LDS have been performed. Besides the intensity I_β of the H_β line, the height I_{cont} of the continuous emission spectrum is taken into account. The continuum arises from electron impact excitation of the molecular $(a)^3\sum_g^+$ state, which decays to the continuous $(b)^3\sum_u^+$–state [133, 134].

It has been found, that the ratio

$$\alpha_{\text{opt}} = \frac{I_\beta}{I_\beta + \kappa\, I_{\text{cont}}},$$

where κ is a calibration constant, reproduces the degree of dissociation α_{QMS} measured with a quadrupole mass spectrometer. This behaviour is illustrated in fig. 9.2 for the dependence of the degree of dissociation on the gas throughput.

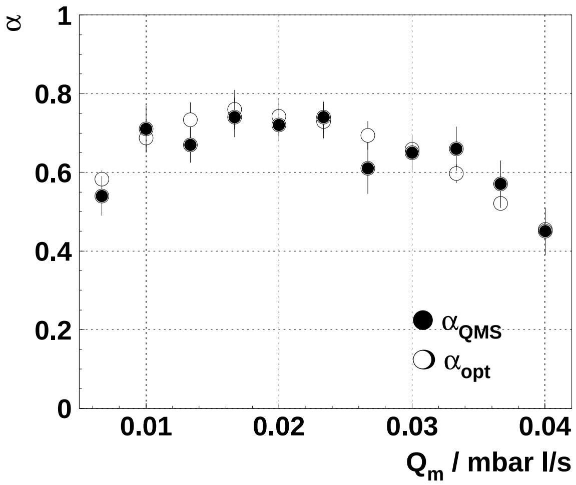

Fig. 9.2: Dependence of the degree of dissociation of the LDS radio frequency dissociator on the gas throughput. The full dots denote the data determined with a quadrupole mass spectrometer and the open circles those obtained with the optical monitor [133, 134].

9.2 Beam formation and attenuation

An improvement of the beam formation and a better understanding and suppression of the attenuation mechanisms are the key problems with respect to a further improvement of the output intensity of polarized atomic beam sources.

The beam attenuation studies have shown, that rest gas attenuation is not sufficient to explain the attenuation losses of the nozzle beam within the present model assumptions. The studies performed using the skimmer chamber as intensity detector clearly indicate an increased forward intensity with increasing throughput. The high peaking exponents are in good agreement with the ones derived from the velocity measurements in the framework of the point source assumption. However, using these peaking exponents obtained, the predicted intensity into the compression tube is much higher than what is actually measured. Assuming a more pronounced attenuation in the dissociator chamber would even result in a higher peaking exponent. In conclusion, there is evidence for an increase of the peaking factor with increasing nozzle throughput. Consequently, an additional attenuation mechanism might be concluded. Attenuation caused by intra–beam scattering following the modell given in section 2.3.1 can be excluded, since the losses would occur mainly in the region of high flow density, i.e., close behind the nozzle. Therefore, a mechanism attenuating the beam or decreasing substantially its phase space density at large distances from the nozzle may account for the observed losses.

In this context it has to be mentioned, that the beam formation was described by an empirical model assuming a point–like nozzle source. In order to improve the description on beam formation and transport, numerical studies based on the so–called "Direct Simulation Monte–Carlo Method" (DSMC) are planned [135]. First attempts to simulate a hydrogen beam under the conditions relevant for polarized atomic beam sources by means of DSMC are reported in ref. [136].

A method to substantially increase the phase space density of the beam is suggested in ref. [137]. The interaction of the nozzle beam with a surrounding hollow, ideally expanded carrier jet should result in a reduced longitudinal temperature of the inner beam and a significantly increased forward intensity. This effect is based on energy and momentum transfer from the inner gas particles to the gas particles of the carrier gas at the inner sheath of the carrier jet. Consequently, the mass of the carrier gas should be as low as possible implying that H_2 is the best alternative to be used. As a positive side effect, the dense carrier jet should shield the inner beam from rest gas attenuation in the dissociator chamber. A schematic picture of the carrier jet set–up is given in fig. 9.3. The inner conical nozzle is surrounded by a Laval nozzle. The carrier gas is fed into

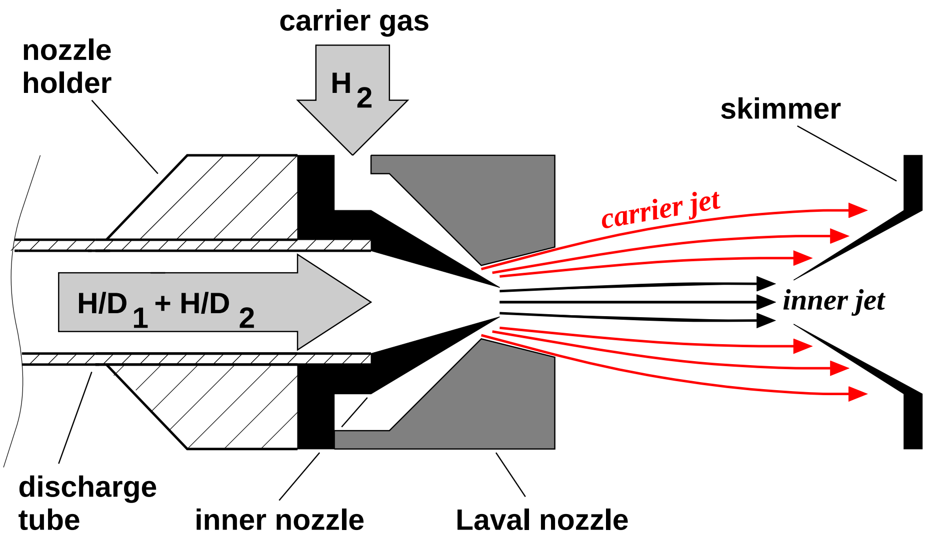

Fig. 9.3: Schematic representation of the carrier jet set–up. The carrier gas expands from an outer Laval–type nozzle surrounding coaxially the inner conical nozzle. The trajectories of the inner and the carrier jet are represented by the solid black and grey lines.

the azimuthal chamber inbetween the two nozzles and expands through an azimuthal slit formed by the edge between the convergent and divergent part of the Laval nozzle and the outer surface of the inner nozzle. The typical flow rate for the carrier jet is about 25 . . . 40 mbar l/s corresponding a pressure of a few tens of millibars in front of the nozzle. In order to minimize the contribution from the carrier jet to the inner beam, the gas flow through the inner nozzle has to be sufficiently high in the range of about 4 . . . 6 mbar l/s. The calculations of the beam properties are based on the solution of the Navier–Stokes equations. The results for an H_2 carrier jet are summarized in table 9.1. The degree of dissociation of the inner beam has been assumed to 50 %. The carrier jet method is

	hydrogen	deuterium
carrier gas flow	35.6 mbar l/s	23.4 mbar l/s
dissociator throughput	6.0 mbar l/s	4.0 mbar l/s
nozzle–skimmer–distance	27 mm	26 mm
temperature of inner beam	5.7 K	3.2 K
Mach–number	7.56	9.39

Tab. 9.1: Calculated results and parameters of the carrier jet set-up for an inner atomic hydrogen and deuterium beam and a molecular hydrogen carrier jet [137].

expected to increase the flow rate through the skimmer by a factor of about 10 compared to the normal nozzle beam.

The atomic beam test stand provides all diagnostics needed to characterize completely the beam produced with the carrier jet method. The partial pressures in the beam and hence the carrier gas admixture to the inner beam can be determined with the mass spectrometer. The intensity is measured by means of the compression tube, and the set–up for the time–of–flight measurements allows for verification of the calculated beam temperatures. The vacuum system of the dissociator chamber has been adapted to the high gas flows of the carrier jet replacing the two turbomolecular pumps by a Roots–blower (LEYBOLD, RUVAC 5001). Additionally, the MWS based disociator has shown to yield high degrees of dissociation in the beam of up to 70 . . . 75 % at gas throughputs of 5 mbar l/s, so that the high flow rates required for the inner beam can be provided with a high atomic fraction. Detailed experimental studies on the carrier jet method are in preparation [112].

A Geometrical Parameters of the HERMES–ABS

In the following table, the main geometrical parameters of the HERMES–ABS are given, taken from ref. [131].

	axial distance / mm	**aperture size** / mm	**length** / mm
nozzle	0	2.0	
skimmer	15	5.0	
collimator	55	9.0	
1st magnet	58	$8.6 \rightarrow 10.4$	30
2nd magnet	108	$12.0 \rightarrow 16.0$	55
3rd magnet	183	$16.7 \rightarrow 26.0$	75
4th magnet	608	26.6	75
5th magnet	723	$26.6 \rightarrow 11.0$	85
cell entrance tube	1208		

Tab. A.1: Geometrical parameters on the beam formation and the sixpole magnet system of the HERMES–ABS.

B Derivation of the Maxwellian EEDF

The Maxwellian velocity distribution $f(v)\,\mathrm{d}v$ denotes the probability to find a particle with a velocity between v and $v+\mathrm{d}v$ and is given in its general form by [110]

$$f(v)\,\mathrm{d}v = \mathcal{N}\,4\,\pi\,v^2\,\exp\left(-\frac{m\,v^2}{2\,k\,T}\right), \tag{B.1}$$

where $\mathcal{N}$ is the normalization constant, m the particle mass, $k = 1.38\times10^{-23}\,\mathrm{J/K}$ the Boltzmann constant and T the temperature.
In order to calculate the process rates and the quantities linked to it, the velocity distribution $f(v)\,\mathrm{d}v$ has to be converted into an energy distribution $f(u)\,\mathrm{d}u$, where the energy $u=(m/2)\,v^2$, and one obtains

$$\begin{aligned} f(v)\,\mathrm{d}v &= f(u(v))\,\frac{\mathrm{d}v}{\mathrm{d}u}\,\mathrm{d}u \\ &= \mathcal{N}\,4\sqrt{2}\,\pi\,m^{-\frac{3}{2}}\,\sqrt{u}\,\exp\left(-\frac{u}{k\,T}\right)\mathrm{d}u\,. \end{aligned} \tag{B.2}$$

$\mathcal{N}$ is obtained taking into account the normalization of the eedf from eq. (3.3) and hence

$$f(u) = \frac{2}{(k\,T)^2}\,\sqrt{u}\,\exp\left(-\frac{2}{k\,T}\,u\right). \tag{B.3}$$

The mean electron energy $\bar{u}$ is given as the first moment of $\sqrt{u}\,f(u)$

$$\bar{u} = \int_0^{+\infty} u\,\sqrt{u}\,f(u)\,\mathrm{d}u = 2\,k\,T, \tag{B.4}$$

and one finally obtains

$$f(u) = \frac{2}{\bar{u}^2}\,\sqrt{u}\,\exp\left(-\frac{2}{\bar{u}}\,u\right). \tag{B.5}$$

C Parametrization of the Inelastic Cross Sections

The experimental data of the inelastic cross sections $\sigma_{\rm in}$ have been paramatrized as a function of electron energy u given in eV for $U_{\rm onset} \le u \le 100\,{\rm eV}$ as follows:

process	**cross section paramatrization** $\Rightarrow\ \sigma_{\rm in}/10^{-16}\,{\rm cm}^2$	**onset energy** $U_{\rm onset}\,/\,{\rm eV}$
R1	$1.7\times10^{-6}\left(\frac{u}{U_{\rm onset}}\right)^{-0.5}\left[\left(\frac{u}{U_{\rm onset}}\right)^{10^{-5}}-1\right]\exp\left(-11\,u^{0.1}\right)$	0.11
R2	$1.305\times10^{-16}\left(\frac{u}{U_{\rm onset}}\right)^{-0.5}\left(\frac{u}{U_{\rm onset}}-1\right)\exp\left(-0.18\,u^{0.9}\right)$	8.8
R3	$1.305\times10^{-16}\left(\frac{u}{U_{\rm onset}}\right)^{-0.5}\left(\frac{u}{U_{\rm onset}}-1\right)\exp\left(-1.07\,u^{0.25}\right)$	15.4
R4	$1.85\times10^{-16}\left(\frac{u}{U_{\rm onset}}\right)^{-0.5}\left(\frac{u}{U_{\rm onset}}-1\right)\exp\left(-0.1\,u^{0.65}\right)$	15.6
R5	$4.69\times10^{-15}\,\frac{1}{u}\,(0.4343\,\ln u-1.01)$	10.2
R6	$2.5\times10^{-15}\,\frac{1}{u}\,(0.4343\,\ln u-1)\,\exp\left[-0.1\,(u-U_{\rm onset})\right]$	10.2

Tab. C.1: Parametrization of the cross sections as a function of electron energy for the predominant inelastic electron–neutral collisions in a hydrogen glow discharge.

D Discharge Tube Materials and Surface Preparation

The possible discharge tube materials for the application in a 2.45 GHz sustained hydrogen surface wave plasma source are listed in the following table.

material	**maximum temperature** $T_{\max}$	**recombination coefficient** $\gamma\,(T_s = 300\,\mathrm{K})$	**relative permitivitty** $\epsilon\,(f_{\mathrm{hf}} = 2.45\,\mathrm{GHz})$
DURAN 8330®	800 °C	$4 \ldots 22 \times 10^{-5}$	4.3
quartz glass	1600 °C	$2 \ldots 300 \times 10^{-5}$	4.0
ALSINT 99.7®	1700 °C	$5 \ldots 10 \times 10^{-5}$	4.5
PYTHAGORAS®	1500 °C	$5 \ldots 10 \times 10^{-5}$	4.5
HALSIC–I®	1350 °C	–	–

Tab. D.1: Possible discharge tube materials for the application in a 2.45 GHz sustained hydrogen SWD. $T_{\max}$ is the maximum applicable temperature specified by the producer.

DURAN 8330® is a borosilicate glass with similar properties as pyrex [139]. ALSINT 99.7® consists of 99.7 % Al_2O_3, PYTHAGORAS® of a mixture of about 60 % Al_2O_3, 35 % SiO_2 and 3 % alkali metals and HALSIC–I® of 90 % Si and 10 % C [138]. No specification could be given by the producer for the relative permittivity of HALSIC–I®. Sufficiently low dielectric losses of discharge tubes made of Al_2O_3 based ceramics for the use in a SWD driven ion source are reported in ref. [102], where also a higher chemical resistance compared to glass has been found. Concerning the recombination properties, the γ values of ALSINT 99.7® and PYTHAGORAS® have been assumed to be comparable those measured for VYCOR® [140].

Using glass tubes, a proper treatment of the tube surface has turned out to be essential in order to provide a low wall recombination rate of the hydrogen atoms. The best results are obtained cleaning the tubes successively with acetone, methanol and destilled water and exposing them to a 2 : 1 acid mixture of concentrated HF (40 %) and HCl (32 %) for approximately 5 min. Afterwards the tubes are extensively rinsed with destilled water and finally baked out under vacuum for 24 h at 150 °C. This procedure yields the same low recombination rates for both quarz and pyrex tubes.

E Geometry and Pressures of the Atomic Beam Test Stand

In fig. E.1 the axial positions and the sizes of the various apertures are shown, as well as the position of the QMS ionisation volume, the compression tube, the TOF–chopper and the QMS–chopper and the beam flapper.

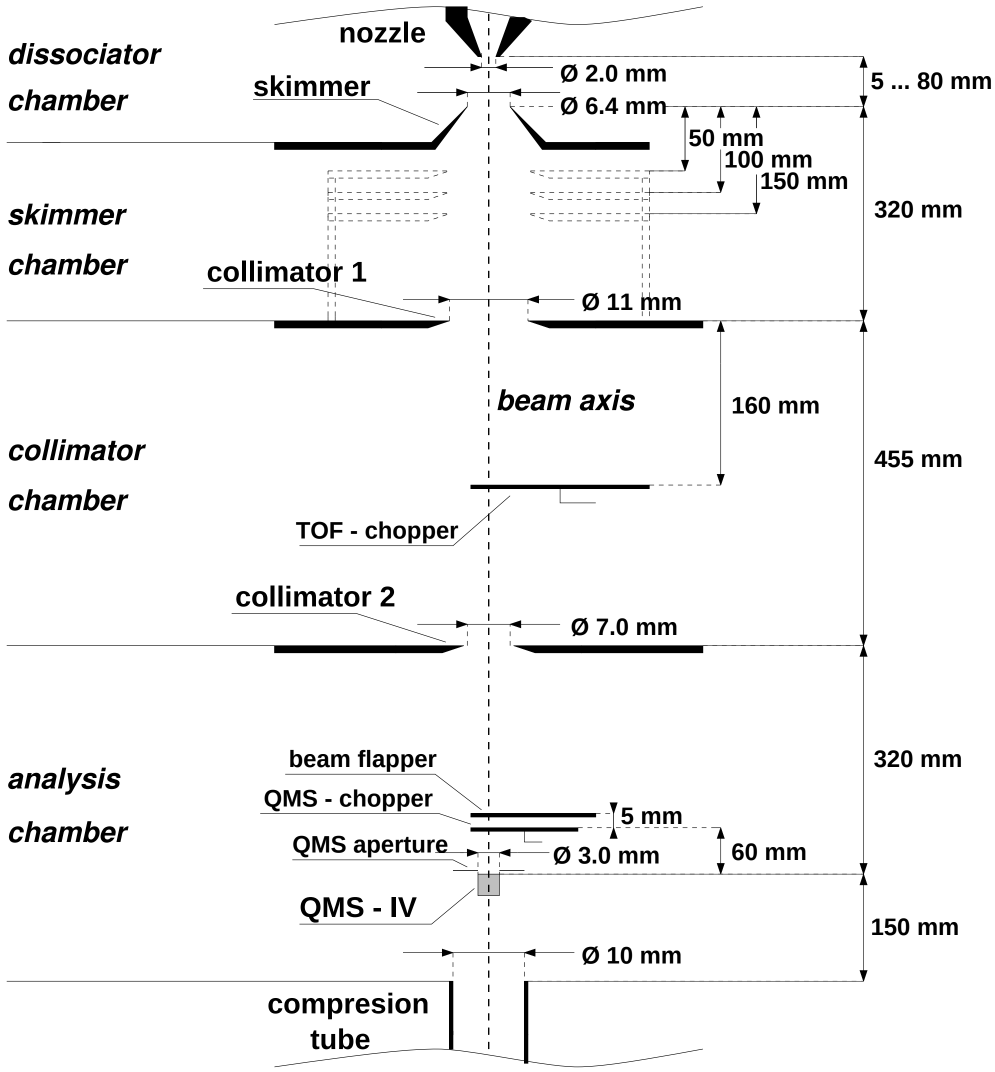

Fig. E.1: Geometrical parameters of the ABT. The beam TOF–chopper, the beam flapper and the QMS can be radially moved out of the beam path. The dashed lines denote the cylinders for modification of the skimmer chamber.

Table E.1 shows the hydrogen partial pressures in the various ABT chambers as a function of the nozzle throughput for a nozzle–skimmer distance of 30 mm.

throughput Q_m / mbar l/s	**dissociator chamber** $p_\text{dis-ch}$ / mbar	**skimmer chamber** $p_\text{sk-ch}$ / mbar	**collimator chamber** $p_\text{col-ch}$ / mbar	**analysis chamber** $p_\text{an-ch}$ / mbar
0	2.0×10^{-7}	6.0×10^{-8}	5.0×10^{-8}	1.3×10^{-7}
1	2.1×10^{-4}	1.8×10^{-5}	7.0×10^{-7}	1.7×10^{-7}
2	5.2×10^{-4}	2.8×10^{-5}	1.4×10^{-6}	2.1×10^{-7}
3	8.6×10^{-4}	4.3×10^{-5}	2.2×10^{-6}	2.6×10^{-7}
4	1.3×10^{-3}	6.0×10^{-5}	3.0×10^{-6}	3.1×10^{-7}
5	1.6×10^{-3}	7.5×10^{-5}	2.2×10^{-6}	1.8×10^{-7}

Tab. E.1: Pressures in the various pumping stages of the atomic beam test stand as a function of dissociator throughput at a nozzle–skimmer distance of 30 mm.

F Nozzle Coating

Prior to surface coating the nozzles have been cleaned from any hydrocarbons or lubricants due to the machining procedure by successive washing in an ultrasonic bath at 50 °C with trichlorethylene, aceton, methanol and finally destilled water for 30 min each.

The Silicone coating applied is based on a two–component mixture (RHONE–POULENC, Rhodorsil® RTV 141 A & B). After merging the two components, the mixture has been evacuated at a pressure of about 50 mbar and vented for several times in order to remove air bubbles arising from the merging procedure. Before the mixture was poured into the nozzle cone, the nozzle surfaces has been treated with a primer (RHONE–POULENC, Primer A 4096). The netting procedure of the Silicone was accelerated by drying the coated nozzles in a clean oven at 50°C.

The Al–99.5 nozzles have been commercially anodized in sulfuric acid to form a homogeneous, roughly 10 μm thick Al_2O_3 layer (SINKOVEC corp.). Afterwards they have been immersed in 95°C hot destilled water for about 30 min.

The quartz coated nozzle has been provided by the INFN Ferrara. An SiO_2 layer has been sputtered onto the Al surface via RF magnetron sputtering [119].

Figures

Tables

References

[1] F. Rathmann*et al.*, Phys. Rev. C **58**, 658 (1998).

[2] B. v. Przewoski *et al.*, Phys. Rev. C **58**, 1897 (1998).

[3] H.O. Meyer *et al.*, Phys. Rev. Lett. **81**, 3096 (1998).

[4] D. Albers *et al.*, Phys. Lett. **78**, 1652 (1997).

[5] H. Rohdjess for the EDDA collaboration, Proc. Workshop on Pol. Gas Targets and Pol. Beams, Urbana 1997, AIP Conf. Proc. No. **421**, 99 (1998).

[6] Proc. Int. Workshop on Intermediate Energy Spin Physics, Jülich 1998, F.Rathmann, W.T.H.van Oers, C.Wilkin (Eds.), to be published.

[7] B. Adeva *et al.*, Phys. Lett. **B 302**, 533 (1993).

[8] D. Adams *et al.*, Phys. Lett. **B 329**, 399 (1994).

[9] D. Adams *et al.*, Phys. Lett. **B 396**, 338 (1997).

[10] D. Adams *et al.*, Phys. Rev. **D 56**, 5330 (1997).

[11] P.L. Anthony *et al.*, Phys. Rev. Lett. **71**, 959 (1993).

[12] K. Abe *et al.*, Phys. Rev. Lett. **74**, 346 (1995).

[13] K. Abe *et al.*, Phys. Rev. Lett. **79**, 26 (1997).

[14] H. Borel for the E155 collaboration, Proc. Int. Workshop on Deep Inelastic Scattering and QCD DIS 98, Brussels 1998, GH. Coremans, R. Rosen (Eds.), World Scientific, 607 (1998).

[15] The HERMES collaboration, *A Proposal to measure the spin–dependent Structure Functions of the Neutron and the Proton at HERA* (1990).

[16] The HERMES collaboration, Technical Design Report, DESY-PRC 93/06 (1993).

[17] M. Düren, Habilitation, University of Erlangen–Nürnberg (1995), DESY internal report HERMES-95-02 (1995).

[18] A. Brüll for the HERMES collaboration, Int. Symp. on Lepton–Photon Interactions LP '97, Hamburg 1997, A. De Roeck, A. Wagner (Eds.), World Scientific, 55 (1998).

[19] D.P. Barber *et al.*, Phys. Lett. **B 343**, 436 (1995).

[20] C. Baumgarten, Diploma Thesis, University of Hamburg (1996).

[21] B. Braun, PhD Thesis, University of Heidelberg (1995).

[22] B. Braun for the HERMES collaboration, Proc. Workshop on Pol. Gas Targets and Pol. Beams, Urbana 1997, AIP Conf. Proc. No. **421**, 156 (1998).

[23] F. Stock, Proc. Workshop on Pol. Beams and Pol. Gas Targets, Köln 1995, H. Paetz gen. Schieck, L. Sydow (Eds.), World Scientific, 260, (1996).

[24] A. Golendoukhin for the HERMES collaboration, Int. Symp. on High–Energy Phys. SPIN 96, Amsterdam 1996, C.W. de Jager *et al.*. (Eds.), World Scientific, 331 (1997).

[25] M. Poelker *et al.*, Proc. Workshop on Pol. Ion Sources and Pol. Gas Targets, Madison 1993, AIP Conf. Proc. No. **293**, 125 (1994).

[26] F. Schmidt, private communication (1998).

[27] M. Miller *et al.*, Proc. Workshop on Pol. Gas Targets and Pol. Beams, Urbana 1997, AIP Conf. Proc. No. **421**, 148 (1998).

[28] A. von Engel, *Electric Plasmas: Their Nature and Uses*, Taylor & Francis Ltd., London and New York (1983).

[29] G. Comsa, R. David, Surf. Sci. Rep. **5**, 145 (1985).

[30] L. Dick *et al.*, Proc. 8^{th} Int. Symp. High–Energy Spin Physics, Minneapolis 1988, AIP Conf. Proc. **187**, 1518 (1989).

[31] G. Scoles, *Atomic and Molecular Beam Methods*, Oxford University Press, New York – Oxford (1988).

[32] M. Wutz, H. Adam, W. Walcher, *Theorie und Praxis der Vakuumtechnik*, 2nd Edition, Vieweg & Sohn, Braunschweig/Wiesbaden (1982).

[33] M. von Ardenne, *Tabellen der Elektronenphysik, Ionenphysik und Übermikro–skopie*, Band II, VEB Deutscher Verlag der Wissenschaften, Berlin (1956).

[34] D. Fick, *Einführung in die Kernphysik mit polarisierten Teilchen*, BI–Hochschulskripten, Mannheim (1971), Reprint by MPI–Heidelberg (1991).

[35] G. Otter, R. Honecker, *Atome – Moleküle – Kerne, Band I Atomphysik*, Teubner, Stuttgart (1993).

[36] G. Breit, I.I. Rabi, Phys. Rev. **38**, 2082 (1931).

[37] W. Haeberli, Ann. Rev. Nucl. Sci. **17**, 373 (1967).

[38] A. Abragam, J.M. Winter, Phys. Rev. Lett. **1**, 374 (1958).

[39] F. Rathmann *et al.*, Phys. Rev. Lett. **71**, 1379 (1993).

[40] W. Korsch, Diploma Thesis, University of Marburg (1987).

[41] W. Korsch, PhD Thesis, University of Marburg (1990).

[42] F. Stock, PhD Thesis, University of Heidelberg (1994).

[43] U. Funk, Diploma Thesis, University of Heidelberg (1995).

[44] P. Schiemenz *et al.*, Nucl. Instr. Meth. **A 305**, 15 (1991).

[45] K. Halbach, Nucl. Instr. and Meth. **A 169**, 1 (1980).

[46] J. Stewart for the HERMES collaboration, Proc. Workshop on Pol. Gas Targets and Pol. Beams, Urbana 1997, AIP Conf. Proc. No. **421**, 69 (1998).

[47] K. Zapfe, private communication (1995)

[48] N. Koch, Diploma Thesis, University of Erlangen–Nürnberg (1995).

[49] F. Stock, Diploma Thesis, University of Heidelberg (1992).

[50] B. Lorentz, Diploma Thesis, University of Heidelberg (1993).

[51] J. Ross, *Molecular Beams*, John Wiley & Sons (1966).

[52] H. Haberland, U. Buck, M. Tolle, Rev. Sci. Instr. **59 (9)**, 1712 (1985).

[53] M. Schick, Diploma Thesis, University of Heidelberg (1990).

[54] E. Steffens, Proc. Workshop on Pol. Gas Targets and Pol. Beams, Urbana 1997, AIP Conf. Proc. No. **421**, 399 (1998).

[55] D. Pohlenz, Diploma Thesis, University of Heidelberg (1989).

[56] J.R. Roth, *Industrial Plasma Engineering, Vol. 1: Principles*, Institute of Physics Publishing, Bristol and Philadelphia (1995).

[57] S.C. Brown, *Basic Data of Plasma Physics*, AIP Press, American Institute of Physics (1993).

[58] R. Winkler, J. Wilhelm, A. Hess, Ann. Phys. **42**, 537 (1985).

[59] M. Moisan *et al.*, J. Vac. Sci. Technol. **B 9 (1)**, 8 (1991).

[60] C.M. Ferreira, J. Loureiro, J. Phys. D: Appl. Phys. **16**, 2471 (1983).

[61] C.C. Goodyear, A. von Engel, Proc. Phys. Soc., Vol. **79**, 732 (1962).

[62] K. Takayanagi, H. Suzuki, *Cross sections for atomic processes, Vol. I*, Research Information Center, Institute of Plasma Physics (1978).

[63] H. Haken, H.C. Wolf, *Molekülphysik und Quantenchemie*, Springer–Verlag, Berlin (1992).

[64] S.J.B. Corrigan, J. Chem. Phys.**43**, 4381 (1965).

[65] K. Wiesemann, *Einführung in die Gaselektronik*, Teubner Studienbücher, Stuttgart (1976).

[66] F.F. Chen, *Introduction to Plasma Physics and Controlled Fusion*, Plenum Press, New York (1984).

[67] D. Korzec *et al.*, J. Vac. Sci. Technol. **A 13 (4)**, 2074 (1995).

[68] S. Davidaud *et al.*, J. Phys. D: Appl. Phys. **22**, 770 (1989).

[69] A. Rousseau *et al.*, J. Phys. D: Appl. Phys. **27**,1412 (1994).

[70] A. Durandet *et al.*, J. Phys. D: Appl. Phys. **22**, 1288 (1989).

[71] O. Fukumasa, R. Itatani, S. Saeki, J. Phys. D: Appl. Phys. **18**, 2433 (1985).

[72] D.J. Rose, S.C. Brown, Phys. Rev. **98 (2)**, 310 (1955).

[73] B.J. Wood, H. Wise, J. Chem. Phys. **66**, 1049 (1962).

[74] K.M. Sancier, H. Wise, J. Chem. Phys. **51**, 1434 (1969).

[75] W.V. Smith, J. Chem. Phys. **11**, 110 (1943).

[76] Y.C. Kim, M. Boudart, Langmuir **7**, 2999 (1991).

[77] D.W. Trainor, D.O. Ham, F. Kaufman, J. Chem. Phys., Vol. **58**, No. **10**, 4599 (1973).

[78] V.H. Shui, J.P. Appleton, J. Chem. Phys. **55**, 3126 (1971).

[79] J. Loureiro, C.M. Ferreira, J. Phys. D: Appl. Phys. **22**, 1680 (1989).

[80] J. Engemann, private communication (1996).

[81] M. Moisan *et al.*, *Microwave Discharges: Fundamentals and Applications*, Plenum Press, New York, 1 (1993).

[82] W. Kubischta, private communication (1996).

[83] P. Schmelzbach, private communication (1997).

[84] D.T. Tuma, Rev. Sci. Instr. **41**, 1519 (1970).

[85] M. Moisan, Z. Zakrzewski, J. Phys. D: Appl. Phys. **24**, 1025 (1991).

[86] G. Goubau, *Electromagnetic Waveguides and Cavities*, Pergammon Press, Oxford, London, New York and Paris (1961).

[87] A.W. Trivelpiece, R.W. Gould, J. Appl. Phys **30**, 1784 (1959).

[88] M. Moisan, C. Beaudry, P. Leprince, Phys. Lett. **50 A (2)**, 125 (1974).

[89] M. Moisan, C. Beaudry, P. Leprince, IEEE Trans. Plasma Sci. **PS–3**, 55 (1975).

[90] M. Moisan, Z. Zakrzewski, R. Pantel, J. Phys. D: Appl. Phys. **12**, 219 (1979).

[91] M. Moisan *et al.*, Revue Phys. Appl. **17**, 707 (1982).

[92] Z. Zakrzewski, M. Moison, G. Sauve, *Microwave Discharges: Fundamentals and Applications*, Plenum Press, New York, 117 (1993).

[93] V.M.M. Claude *et al.*, J. Appl. Phys. **51 (11)**, 5693 (1980).

[94] M. Moisan et al, J. Phys. E: Sci. Instr. **20**, 1356 (1987).

[95] N. Koch, E. Steffens, Rev. Sci. Instr. **70 (3)**, 1631 (1999).

[96] R.N. Ghose, *Microwave Circuit Theory and Analysis*, McGraw–Hill (1963).

[97] M. Moisan, Z. Zakrzewski, Rev. Sci. Instr. **58 (10)**, 1895 (1987).

[98] J. Margot–Chaker *et al.*, J. Appl. Phys. **66**, 4134 (1989).

[99] A. Ding, J. Karlau, J. Weise, Rev. Sci. Instr., **48 (8)**, 1002 (1977).

[100] H. Nowakowska, Z. Zakrzewski, M. Moisan, J. Phys. D: Appl. Phys. **22**, 789 (1990).

[101] S.C. Brown, A.D. MacDonald, Phys. Rev. **76 (11)**, 1629 (1949).

[102] L. Bertrand *et al.*, Rev. Sci. Instr. **50 (6)**, 708 (1979).

[103] K.E. Shuler, K.J. Laidler, J. Chem. Phys. **17 (12)**, 1212 (1949).

[104] H. Wise, C.M. Ablow, K.M. Sancier; J. Chem. Phys. **44**, 3569 (1964).

[105] T. Wise, private communication (1996).

[106] Z. Rakem, P. Leprince, J. Marec, J. Phys. D: Appl. Phys. **25**, 953 (1992).

[107] V. Varentsov, private communication (1997).

[108] LEYBOLD AG, product information (1996).

[109] R.B. Scott, *Cryogenic Engineering*, D. Van Nostrand Company, Princeton (1959).

[110] H. Wegener, *Physik für Hochschulanfänger*, Teubner Studienbücher, Stuttgart (1989).

[111] F. Reif, *Statistische Physik und Theorie der Wärme*, De Gruyter, Berlin, New York (1987).

[112] A. Nass, PhD thesis, University of Erlangen–Nürnberg, in preparation.

[113] W.L. Fite, R.T. Brackmann, Phys. Rev. **112**, 1141 (1958).

[114] C.N. Burraus, A.J. Lieber, V.T. Zaviantseff, Rev. Sci. Instr. **38**, 291 (1967).

[115] W. Kubischta, G. Boero, Internal CERN/Help note **47** (1994).

[116] G. Boero, W. Kubischta, P. Leprince, Proc. Workshop on Pol. Beams and Pol. Gas Targets, Köln 1995, H. Paetz gen. Schieck, L. Sydow (Eds.), World Scientific, 270, (1996).

[117] G. Boero, W. Kubischta, P. Leprince, Nucl. Instr. Meth. **A 398**, 157 (1997).

[118] P.F. Dalpiaz, private communication (1997).

[119] P.F. Dalpiaz *et al.*, Nucl. Instr. Meth. **A402**, 171 (1998).

[120] J.L. Lemaire, Proc. Workshop on Polarized Ion Sources and Polarized Gas Targets, Madison, Wisconsin 1993, AIP Conf. Proc. No. **293**, 106 (1994).

[121] J.T.M. Walraven, I.F. Silvera, Rev. Sci. Instr. **53 (8)**, 1167 (1982).

[122] H. Wise, B.J. Wood, Adv. At. Mol. Phys. **3**, 291 (1967).

[123] D. Singy *et al.*, Nucl. Instr. Meth. **B 47**, 167 (1990).

[124] H. Kolster, PhD thesis, University of München (1998).

[125] N. Koch, A. Nass, E. Steffens, Proc. Int. Symp. on High–Energy Phys. SPIN 98, to be published.

[126] V.L. Varentsov, private communication (1998).

[127] T. Wise, A.D. Roberts, W. Haeberli, Nucl. Instr. Meth. **A336**, 410 (1993).

[128] R. Hertenberger *et al.*, Rev. Sci. Instr. **69 (2)**, 750 (1998).

[129] T. Wise, private communication (1996).

[130] V.L. Varentsov, *Calculations on nozzle beam properties*, unpublished (1997).

[131] S. Frabetti, B. Braun, N. Koch, HERMES Int. Note No. 98–033 (1998).

[132] C. Appelt, Diploma Thesis, University of Erlangen–Nürnberg (1994).

[133] W. Nagengast, PhD Thesis, University of Erlangen–Nürnberg (1999).

[134] F. Schmidt, PhD Thesis in preparation, University of Erlangen–Nürnberg.

[135] C. Bartels, Habilitationsschrift, University of Erlangen–Nürnberg, in preparation.

[136] I.D. Boyd, W. Kubischta, Proc. Workshop on Pol. Ion Sources and Pol. Gas Targets, Madison 1993, AIP Conf. Proc. No. **293**, 44 (1994).

[137] V.L. Varentsow, A.A. Ignatiew, E. Steffens, N. Koch, Proc. Workshop on Pol. Gas Targets and Pol. Beams, Urbana 1997, AIP Conf. Proc. No. **421**, 381 (1998).

[138] HALDENWANGER Technische Keramik GmbH & Co. KG, product information (1996).

[139] SCHOTT Glaswerke, product information (1996).

[140] A. Mandl, A. Salop, J. Appl. Phys., **44 (10)**, 4776 (1973).

Danksagung

Als Entwicklungssprojekt zur Verbesserung der am HERMES–Experiment eingesetzten Targetquelle, wurde die vorliegende Arbeit im wesentlichen am Deutschen Elektronensynchrotron (DESY) in Hamburg durchgeführt. Die dabei von Seiten des DESY, des Max–Planck–Instituts (MPI) für Kernphysik in Heidelberg, des Forschungszentrums (FZ) Jülich, sowie – last not least – der HERMES–Kollaboration gewährte Unterstützung hat im wesentlichen zum erfolgreichen Gelingen beigetragen.
Für die gute Zusammenarbeit möchte ich dabei folgenden Personen sehr herzlich danken:

◇ Meinem Doktorvater Herrn Prof. Dr. E. Steffens (Univ. Erlangen–Nürnberg) für die intensive und konstruktive Betreuung, sowie für die fortdauernde Unterstützung während des gesamten Projekts.

◇ Herrn Prof. Dr. K. Rith (Univ. Erlangen–Nürnberg) und Herrn Prof. Dr. D. Fick (Univ. Marburg) für die finanzielle Unterstützung und viele wertvolle Ratschläge.

◇ Herrn Prof. Dr. O. Schult und Herrn Dr. H. Seyfarth (FZ Jülich) für die finanzielle Unterstützung.

◇ Dem DESY Management für die technische und finanzielle Unterstützung.
Insbesondere danke ich Herrn Dr. Y. Holler für seine stete Hilfsbereitschaft und wertvolle Ratschläge während meiner gesamten Zeit am DESY.
Den Herren K. Hakelberg und M. Krüger danke ich recht herzlich für die zahlreichen Hilfestellungen in elektrotechnischen Dingen, sowie W. Beckhusen und V. Prahl für ihre Unterstützung bei mechanischen Problemen.
Bei der mechanischen Hauptwerkstatt unter der Leitung von Herrn R. Struck möchte ich mich für die präzise und zuverlässige Ausführung zahlreicher Aufträge bedanken, insbesondere sei Herrn D. Lieberz für seine gründliche Arbeit beim Bau der Plasmaquelle gedankt.
Dr. K. Zapfe danke ich für die finanzielle Unterstützung sowie für zahlreiche interessante Diskussionen in targettechnologischen Fragestellungen.

◇ Dr. Antje Brüll (MPI Heidelberg) für die gewährte Unterstützung durch die mechanische Hauptwerkstatt des MPI unter der Leitung von Herrn V. Mallinger, dem ich für die zahlreichen Ratschläge und Anregungen bzgl. mechanischer Fragestellungen danke.
Hierbei ist ausdrücklich die hervorragende Arbeit von Herrn E. Hänisch zu erwähnen, der das Entwicklungsprojekt während der gesamten Zeitdauer begleitete und der durch seine präzise und schnelle Durchführung der Aufträge viele der in dieser Arbeit präsentierten Studien erst möglich machte.

◇ Der mechanischen Werkstatt der Univ. Erlangen–Nürnberg unter der Leitung von Herrn G. Muhr und G. Heimpel, deren stete Hilfsbereitschaft und Unterstützung

ich schon während meiner Diplomarbeit zu schätzen lernte.
Insbesondere sei Herrn S. Sponer für seinen Einsatz beim Bau der Kältebrücke für die Düsenkühlung und Herrn F. Kolb für seine Geduld bei der Anfertigung der Düsen gedankt.

- Den Tandemoperateuren der Univ. Erlangen–Nürnberg unter der Leitung von Herrn P. Nickl, insbesondere den Herren H. Schott und H. Wildner für die konzentrierten Hilfsaktionen am DESY.

- Dem Glasbläser der Ingenieurswissenschaftlichen Fakultäten der Univ. Erlangen–Nürnberg, Herrn K. Händel, für den schnellen Nachschub an Entladungsrohren sowohl für die Targetentwicklung als auch die HERMES–Targetquelle, sowie für die zahlreichen Ratschläge in Sachen Glas.

- Unserer Erlanger Sekretärin Frau H. Löhner und den HERMES Sekretärinnen Frau S. Krohn und R. Matthes für die stets schnelle, effiziente und unbürokratische Hilfe.

- Der HERMES–Kollaboration und speziell der Targetgruppe für das kooperative und konstruktive Arbeitsklima. Für die zahlreichen interessanten und lehrreichen Diskussionen in physikalischen und technischen Belangen möchte ich mich besonders bei C. Baumgarten, Dr. B. Braun, Prof. Dr. G. Court, Dr. M. Düren, S. Frabetti, A. Golendhoukhin, Prof. Dr. G. Graw, M. Henoch, Dr. R. Hertenberger, Dr. H. Kolster, Dr. W. Korsch, A. Nass, C. Simani, Dr. J. Stewart, T. Wise und Dr. K. Zapfe bedanken.
  Für die Hilfe beim Aufbau, der Wartung und der Programmierierung des Datenaufnahmesystems sei speziell Christian Baumgarten, Dr. Bernd Braun, Dr. Walter Brückner und dem Sommerstudenten Stefan Schromm gedankt.
  Aleksan Golendhoukhin danke ich für die gute Zusammenarbeit bei der Installation und dem Betrieb der polarisierten Targetquelle.
  Speziell sei auch Dr. Jim Stewart für seine unzähligen Ratschläge in physikalischen, technischen und politischen Belangen während meiner gesamten Zeit in der Targetgruppe gedankt.
  Für die konstruktive Mitarbeit am Targetentwicklungsprojekt in der Endphase meiner Promotion danke ich Alexander Nass, dem ich noch viel Erfolg bei der Fortführung des Projekts wünsche.

- Herrn Dr. W. Kubischta (CERN) für die vielen interessanten Diskusssionen und wertvollen Ratschläge.

- Dr. V. Varentsow (St. Petersburg) und Dr. C. Bartels (Univ. Erlangen–Nürnberg) für tiefere Einblicke in die Strömungsmechanik.

- Den Mitgliedern der Targetgruppe des ANKE–Experiments am COSY–Ring dess FZ Jülich, insbesondere Dr. V. Nelyubin, Dr. F. Rathmann, Dr. H. Seyfarth und Dr. A. Vasssiliev.

- ◇ Natürlich meinen Erlanger Noch– und Ex–Kollegen Dr. Thomas Benisch, Stefan Bernreuther, Peter Budz, Dr. Michael Düren, Dr. Manfred Ferstl, Klaus Fiedler, Dr. Carsten Grosshauser, Andreas Gute, Dr. Matthias Kirsch, Daniel Körner, Stefan Lorenz, Wolfgang Nagengast, Dr. Frank Neunreither, Frank Schmidt, Michael Schmitt–Wiesmann, Dr. Jörn Stenger und Jürgen Wilbert für das gute Arbeitsklima und viele interssante Diskussionen.
  Unsam Bombercha Wolfgang Nagengast ganz speziell für die zahlreichen Tips in Sachen Latex, Paw und Biokost.

- ◇ Last not least meinen Eltern für die Ermöglichung des Physikstudiums und die stets gewährte Unterstützung und meiner Frau Daniela für Ihre Liebe und die im Zuge dieser Arbeit ertragenen Entbehrungen.